GLASS RAIN
MODELLING THE FORMATION, DYNAMICS AND RADIATIVE-TRANSPORT OF CLOUD PARTICLES IN HOT JUPITER EXOPLANET ATMOSPHERES

Graham Kim Huat Lee

A Thesis Submitted for the Degree of PhD
at the
University of St Andrews

PhD

Please use this identifier to cite or link to this item:
http://hdl.handle.net/10023/11740

Glass Rain

Modelling the formation, dynamics and radiative-transport of cloud particles in hot Jupiter exoplanet atmospheres

by

Graham Kim Huat Lee

Submitted for the degree of Doctor of Philosophy in Astrophysics

27th March 2017

University
of
St Andrews

Declaration

I, Graham Kim Huat Lee, hereby certify that this thesis, which is approximately 32,000 words in length, has been written by me, that it is the record of work carried out by me and that it has not been submitted in any previous application for a higher degree.

Date Signature of candidate

I was admitted as a research student in September 2013 and as a candidate for the degree of PhD in September 2013; the higher study for which this is a record was carried out in the University of St Andrews between 2013 and 2017.

Date Signature of candidate

I hereby certify that the candidate has fulfilled the conditions of the Resolution and Regulations appropriate for the degree of PhD in the University of St Andrews and that the candidate is qualified to submit this thesis in application for that degree.

Date Signature of supervisor

Copyright Agreement

In submitting this thesis to the University of St Andrews we understand that we are giving permission for it to be made available for use in accordance with the regulations of the University Library for the time being in force, subject to any copyright vested in the work not being affected thereby. We also understand that the title and the abstract will be published, and that a copy of the work may be made and supplied to any bona fide library or research worker, that my thesis will be electronically accessible for personal or research use unless exempt by award of an embargo as requested below, and that the library has the right to migrate my thesis into new electronic forms as required to ensure continued access to the thesis. We have obtained any third-party copyright permissions that may be required in order to allow such access and migration, or have requested the appropriate embargo below.

The following is an agreed request by candidate and supervisor regarding the electronic publication of this thesis: Access to Printed copy and electronic publication of thesis through the University of St Andrews.

Date Signature of candidate

Date Signature of supervisor

Abstract

The atmospheres of exoplanets are being characterised in increasing detail by observational facilities and will be examined with even grater clarity with upcoming space based missions such as the James Webb Space Telescope (JWST) and the Wide Field InfraRed Survey Telescope (WFIRST). A major component of exoplanet atmospheres is the presence of cloud particles which produce characteristic observational signatures in transit spectra and influence the geometric albedo of exoplanets. Despite a decade of observational evidence, the formation, dynamics and radiative-transport of exoplanet atmospheric cloud particles remains an open question in the exoplanet community. In this thesis, we investigate the kinetic chemistry of cloud formation in hot Jupiter exoplanets, their effect on the atmospheric dynamics and observable properties. We use a static 1D cloud formation code to investigate the cloud formation properties of the hot Jupiter HD 189733b. We couple a time-dependent kinetic cloud formation to a 3D radiative-hydrodynamic simulation of the atmosphere of HD 189733b and investigate the dynamical properties of cloud particles in the atmosphere. We develop a 3D multiple-scattering Monte Carlo radiative-transfer code to post-process the results of the cloudy HD 189733b RHD simulation and compare the results to observational results. We find that the cloud structures of the hot Jupiter HD 189733b are likely to be highly inhomogeneous, with differences in cloud particle sizes, number density and composition with longitude, latitude and depth. Cloud structures are most divergent between the dayside and nightside faces of the planet due to the instability of silicate materials on the hotter dayside. We find that the HD 189733b simulation in post-processing is consistent with geometric albedo observations of the planet. Due to the scattering properties of the cloud particles we predict that HD 189733b will be brighter in the upcoming space missions CHaracterising ExOPlanet Satellite (CHEOPS) bandpass compared to the Transiting Exoplanet Space Survey (TESS) bandpass.

Acknowledgements

This work could not have been completed without the support and advice of multiple individuals who have respectively given emotional, financial, professional and social support with great grace and patience. I highlight some especially important people below.

To my family and the Kelly family, who have provided monetary and emotional support since the beginning. To the support, catering and administrative staff at the Physics & Astronomy building, without which, I estimate the building would collapse in two days. To the general UK exoplanet community for the opportunity to converse and present research to throughout the years, with special thanks to the Exeter and Met Office folks who have been especially supportive of my research. To all former PhD students and Post-docs of the LEAP team at St Andrews: Craig, Paul, Irena and Isabel who provided invaluable advice and discussion on many topics from presentation skills to general jolliness. To Gabriella Hodosán for being a student in arms at the LEAP team, may your spells never be counter magicked again. To the extraordinary gifted and talented bunch of people I have shared office space with over the years (you know who you are). To my principle collaborators Ian Dobbs-Dixon, Kenny Wood and Peter Woitke, who's shoulders, teachings and code many chapters of this thesis stand on. To my supervisor Christiane Helling, who for some reason took me on as an unproven summer student many years ago and started this whole process.

Lastly, I've come to find that practicing theoretical science and modelling is alot like music theory, different sections coming together to form a harmonic whole. Sometimes, different regions need to be tweaked or a new instrument learned altogether, but what matters is the flow of the whole song and sometimes the simplest melody can be the most enjoyable. That said, without music (and an uplifting beat) this whole process would probably have been orders of magnitude less productive and enjoyable. So, the last dedication is to musical producers everywhere.

Contents

1

Introduction

Breathing air is a critical property of the biology of land animals, without a constant stream of oxygen and expellent of carbon dioxide, red blood cells cannot carry oxygen to other cells for normal bodily functions. We rely on our ambient atmospheric conditions for the continued sustaining of life on planet Earth. A question often asked in the realm of science fiction is would Earth confined animals be able to breath freely on other planets? Or if not, could alien life forms develop a different biological mechanism to their natural habitats natural atmospheric composition, perhaps toxic to Earth based animals? If we wish to answer these questions we must first ask a more general question, what exactly are exoplanet atmospheres made of, what gases do they contain? And at what temperatures and pressures? Only in the past few years has this fundamental question begun to be answered by the astrophysical and planetary science communities.

The relatively recent scientific field of exoplanets has been responsible for significant technological progress, from development of complex statistical techniques (e.g. Monte Carlo Markov Chains; MCMC), to high precision photometry and spectroscopy. The field has pushed technological advancements in numerous areas: Radial velocity measurements have necessitated the development of highly stable, low temperature spectrographs in order to measure shifts in spectra from doppler effects on the order of meters per second (e.g. HARPS; Mayor et al. 2003, HARPS-N; Cosentino et al. 2012). Transiting exoplanet studies require highly stable and sensitive photometry for detection, pioneered by early ground based transit survey missions such a Wide Angle Search for Planets (WASP; Pollacco et al. 2006) and COnvection ROtation et Transits planétaires (COROT; Auvergne et al. 2009). Both the upcoming space based missions CHaracterising ExOPlanet Satellite (CHEOPS; Broeg et al. 2013) and Transiting Exoplanet Space Survey (TESS; Ricker et al. 2014) space mission required the construction of a highly stable broadband illumination source for instrument testing [1]. Directly imaged exoplanets involves highly stable observational instrumentation, with several direct imaging facilities online or planned (e.g. Gemini Planet Imager (GPI; Macintosh et al. 2014), Spectro-Polarimetric High-Contrast Exoplanet REsearch (SPHERE; Beuzit et al. 2008) including chronographs on board the upcoming James Webb Space Telescope (JWST) and the Wide Field InfraRed Survey Telescope (WFIRST). Since direct imaging directly detects scattered or emitted photons from a planetary atmosphere, it is promising to be the next large leap in the understanding of exoplanet systems and atmospheres.

The rapid progress in the field of exoplanet astronomy parallels a general era of massive human technological and scientific advances. Perhaps due to the imagination of science fiction writers, exoplanets inspire the general public and remind us of the optimism of space exploration. Additionally, similar to science fiction, exoplanets reflect our own reality here on Earth. Is our world really so special and unique? Or are there a multitude of Earth-like planets ready to explored?

1.1 Exploring Exoplanet Atmospheres

A primary method of detecting exoplanets is the so called 'transit method', whereby a planet passes in front of its host star within the viewing plane of the Earth. This method yields a wealth of information about the exoplanetary system (Seager, 2010). By measuring the percentage dip in the flux from the host star as the planet passed in front of the host star (primary transit), the radius of the planet can be found, since the dip in flux is proportional to

---

[1] http://nccr-planets.ch/the-most-stable-source-of-light/

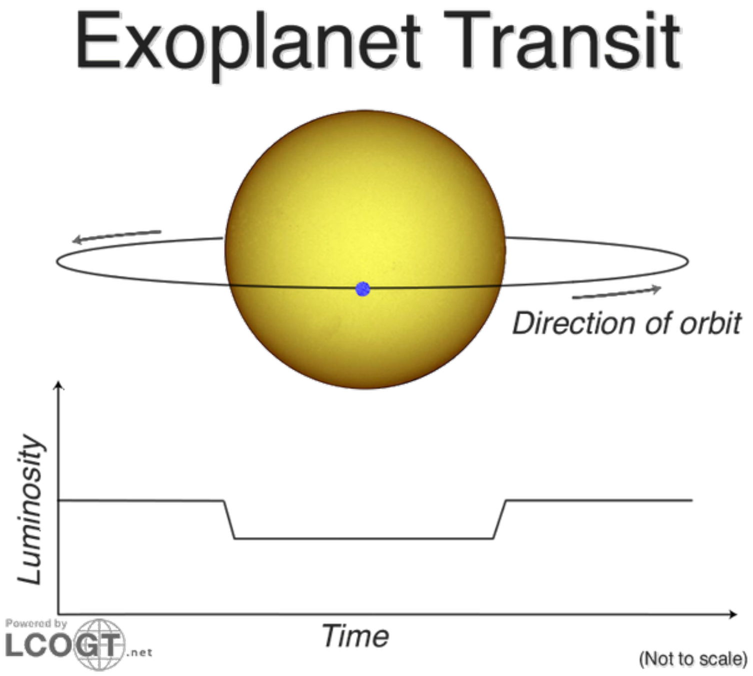

Figure 1.1: Schematic diagram of a transiting exoplanet system (Courtesy: LCOGT consortium). As the planet transits in front of its host star, the planet intercepts a portion of the star's flux towards Earth, resulting in a detectable dip in the total system brightness or luminosity for the duration of the transit.

the planetary radius by the relation

$$\frac{\Delta F_\star}{F_\star} = \left(\frac{R_p}{R_\star}\right)^2, \tag{1.1}$$

where $\Delta F_\star$ is the difference in flux outwith and during the transit, $F_\star$ the out of transit flux of the star, R_p the radius of the planet and $R_\star$ the radius of the star. Figure 1.1 shows an illustration of a transiting system.

If this measurement is carried out wavelength dependently, the exoplanet atmospheric properties can be detected. Since molecules and atoms have wavelength dependent opacities, the planet will appear larger or smaller with wavelength dependent on the atoms and molecules present in the atmosphere. Thus, molecular and atomic absorption features are imprinted in the transmission spectra of the exoplanet, allowing astronomers to deduce the compositional makeup of the atmosphere. From the duration of the transit (ingress to egress), and knowing the radius of the star, the orbital period of the planet can be calculated, as well as the inclination of the planet to the line of sight to Earth. At secondary eclipse, when the planet passed behind the host star, the reflected and emitted light by the planet is removed from the total star and planet system. Thus, by measuring the secondary eclipse of a planet, the scattered and emitted light spectrum of the exoplanet atmosphere can be reconstructed. Figure

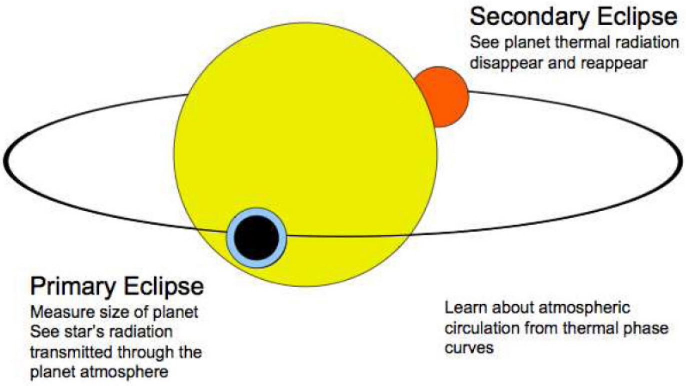

Figure 1.2: Schematic diagram of a transiting exoplanet system (Seager, 2010). During primary transit, the atmosphere can be detected by performing wavelength dependent measurements. The radius of the exoplanet will change with wavelength, and an absorption spectrum can be built up. During secondary eclipse, the scattered and thermally emitted light of the planet is blocked by the host star, so by subtracting the spectrum before and during secondary eclipse the spectrum of the planet can be built up.

1.2 shows an illustration of the transmission spectrum and secondary eclipse measurement process.

The first transiting exoplanet, HD 209458b, was discovered by Charbonneau et al. (2000), beginning a worldwide search for other transiting exoplanets. Some of the first theoretical works on exoplanet atmospheres and clouds were also conducted in the early 2000's. Marley et al. (1999) modelled the albedo and reflection spectrum of theoretical exoplanet temperature-pressure structures and cloud coverage. Seager & Sasselov (2000) modelled the transmission spectrum of theoretical exoplanet atmospheres, which lay the theoretical framework of the direct detection of a transiting planet's atmosphere. Seager et al. (2000) also modelled scattered light phase curves and polarisation fractions using a Monte Carlo radiative-transfer scheme.

The first detection of an exoplanetary atmosphere came shortly after with the Hubble Space Telescope (HST) (Charbonneau et al., 2002), which detected atomic sodium (Na), one of the most abundant atmospheric metallic elements, via transmission spectroscopy in the atmosphere of HD 209458b. Other atomic and molecular features were also detected in HD 209458b and other exoplanets, such as K (Sing et al., 2011), H_2O (Swain et al., 2009), CO (Snellen et al., 2010) and CH_4 (Swain et al., 2008).

To date, the best characterised exoplanet atmospheres are 'hot Jupiters', Jupiter sized exoplanets orbiting close to their host star. A significant observational feature of these exoplanet atmospheres is the inference of cloud particle cover. Evidence of cloud cover comes in three main effects on the transit spectra of hot Jupiters. First, a 'Rayleigh-like' scattering slope at optical wavelengths (e.g. HD 189733b; Lecavelier Des Etangs et al. 2008; Pont et al. 2013), interpreted as cloud or high altitude haze particles scattering photons out the observed line-of-sight. The observed slopes of hot Jupiter transit spectra are usually fit with an optical cross section with a wavelength dependence $\sigma \propto \lambda^{-4}$, intrinsically assuming Rayleigh scattering materials in the atmosphere. However, this does not mean that these slopes are strictly caused by small particles that satisfy the Rayleigh scattering size parameter limit ($\mathrm{x} = 2\pi \mathrm{a} \ll \lambda$), are physically present in the atmosphere. This fitting procedure, however, gives a first theoretical estimate of the types of particles required to fit the optical spectra. Second, muted or reduced H_2O feature (e.g. HD 209458b; Deming et al. 2013), interpreted as cloud particles covering or blanketing H_2O absorption features. Thirdly, reduced/anomalous or muted Na or K absorption features from solar metallicity (e.g. WASP-31b; Sing et al. 2015), interpreted as the cloud particles opacity blanketing the Na and K absorption features. Condensation of Na and K containing cloud material is also a possibility, reducing the gas phase abundances of Na and K and therefore their absorption features. Sing et al. (2016) present a set of 10 hot Jupiter atmospheres, including HD 189733b, HD 209458b and WASP-31b, in transit spectroscopy using HST and Spitzer, each exhibiting one or more of the above features. Their measurements suggest that some form of cloud cover is common to hot Jupiters across a large equilibrium temperature scale (T_{eq} = 1000—2000 K).

More evidence of cloud particles on hot Jupiter atmospheres are the numerous albedo measurements and optical phase curve measurements made during the secondary eclipse of transiting exoplanets. Most published albedo measurements come from the Kepler mission (Borucki et al., 2010), which observes in an optical photometry band from 0.3—1.1 μm. A westward offset from the sub-stellar point (the closest point of the exoplanet to its host star) in the optical phase curves of Kepler-7b was observed by Demory et al. (2013) which was interpreted as cloud particles that scatter optical wavelength photons on the western hemisphere. But a reduced or absent cloud particle abundance on the eastern hemisphere. More Kepler planets (e.g. Kepler-12b, Kepler-8b, Kepler-41b; Angerhausen et al. 2015; Esteves et al. 2015; Shporer & Hu 2015) were found to exhibit similar phase curve behaviour, revealing that offset optical phase curves may be a common feature of hot Jupiter atmospheres. Some Kepler field planets (e.g. HAT-P-7b, Kepler-5b, Kepler-7b, Kepler-17b, Kepler-41b, Keper-76b; Heng & Demory 2013; Angerhausen et al. 2015; Esteves et al. 2015) also have non-negligible geometric albedos ($A_g > 0.1$) in the Kepler bandpass (0.43—0.89 μm), suggesting the presence of an optical to near-IR scattering aerosol. B Band (0.29—0.45μm) and V Band (0.45—0.57μm) geometric albedo measurements of HD 189733b by Evans et al. (2013) using HST STIS show a blueward slope in the optical, inferring the presence of wavelength-dependent, backscattering cloud particles.

Earth-sized planets in habitable zones are already being discovered, most recently, TRAPPIST 1 (Gillon et al., 2017) was found to contain seven Earth sized planets orbiting an M dwarf, three of which are in a conservatively defined habitable zone. The closest star to the Sun, Proxima Centauri contains an Earth mass sized planet at a temperate semi major axis from the host M dwarf (Anglada-Escudé et al., 2016), found by radial velocity measurements. However, many questions remain about these Earth sized planets, such as the effect of fierce stellar flares on the survivability of the planetary atmosphere.

1.2 Historical Background

The scientific investigation into the properties of cloud particles has a rich and varied history, too large to fully summarise here. However, of most relevance to the methodology and cloud particle chemistry used in this thesis is the work of John Aitken. A key founder of modern cloud and aerosol science, John Aitken, FRS, FRSE (18 September 1839 — 14 November 1919) was a Scottish scientist who spent most of his life in Falkirk. He contributed much to the first experimentation on the formation of water clouds and the important role seed particles play in their development. One key experiment he performed was to pass steam through a cotton wool filter, before letting the steam enter a larger vessel to expand and condense. He found that the steam lost its ‘cloudiness’ when it passed through the filter and would be clear. The filtered steam also did not condense in the center of the chamber due to a lack of condensation surfaces. From this, he deduced that the small impurities and particles removed by the cotton wool filter were vital to an efficient condensation process. In one invention, air was sucked into a handheld device containing supersaturated water vapour and the user was able count the number of droplets formed on a glass screen. From this, he could estimate the number density of aerosols present in the atmosphere. Aitken nuclei, the smallest cloud seed particles of $\sim$ 1 nm in radius found in Earth’s atmosphere, are named after him.

1.3 Brown Dwarf and Planetary Science Atmosphere Heritage

The exoplanet scientific community draws significantly on the theoretical and modelling experience of the well matured fields of Brown Dwarf and planetary science atmospheric research, which share many similarities, but also many differences, to exoplanet atmosphere modelling. The early and late 2000's saw development of many cloud formation models, each bringing the philosophies and assumptions from either the stellar or planetary science community. Two main cloud formation methodologies have emerged from the large volume of works on Brown Dwarf and Gas Giant atmospheres currently used for exoplanet atmospheres, an equilibrium cloud approach and a kinetic approach. Both contain different assumptions and philosophies, but have been generally consistent on the large scale details of clouds (height extension, sizes etc.), but differ significantly on smaller scales (chemistry, size distribution etc.). We summarise each of these approaches below. Specific details on the approaches of each model can be found in Helling et al. (2008b).

1.3.1 Equilibrium Modelling

The major class of exoplanet cloud formation modelling has used equilibrium states and methodologies as the basis of their cloud formation model. A common theme to all equilibrium models is a key assumption that cloud material is instantaneously in supersaturated equilibrium ($S(T) = 1$; Eq. 2.1) and elements removed from the gas phase. The cloud base is defined as the region where a species $S(T) = 1$ on a temperature-pressure profile, with schemes to inform particle density and size in supersaturated $S(T) > 1$ regions above this point. These approaches are also 'bottom-up', where the integration is carried out from the base of the atmosphere to the top for each species independently. Thus, clouds are 'pure' and homogenous in composition, with usually one representative species for each family of solid materials (silicates, iron, titanium etc.) chosen.

Ackerman & Marley (2001) present an equilibrium cloud model where the upward mixing of condensible gas is balanced by the sedimentation velocity of the cloud particles. The height of the cloud deck can be controlled by the sedimentation efficiency parameter $f_{\rm sed}$, which is directly multiplied by the sedimentation velocity. The model is described by the balancing of the equation

$$-K_{\rm zz}\frac{\partial q_t}{\partial z} - f_{\rm sed}w_{\star}q_c = 0, \tag{1.2}$$

where K_{zz} [cm^2 s^{-1}s] is the eddy diffusion coefficient, $q_t = q_c + q_v$ the molar fraction of the solid condensate and gas phase vapour, z [cm] the atmospheric height, f_{sed} the sedimentation efficiency parameter, $w_\star$ [cm s^{-1}] the settling velocity and q_c the condensate molar fraction. By assuming a particle distribution (usually log-normal) the number density and particle sizes can be derived for each profile from the f_{sed} parameter. The sedimentation parameter f_{sed} is a tunable parameter with a physical interpretation. For low values of f_{sed} (e.g. < 1), particles are retained at greater atmospheric heights in the atmosphere, with smaller particles present at the cloud layer (due the required balancing with the settling velocity and eddy diffusion). For higher values of f_{sed} (e.g. > 1) the sedimentation of particles is enhanced, resulting in a more compact cloud layer, with larger particles.

The Tsuji (2002, 2005) and related family of models apply a temperature cut off T_{cr} to control the height of the cloud above the $\text{S(T)} = 1$ region. This critical temperature is set to lower that the saturation temperature of the material of interest (i.e. $\text{T}_{\text{cr}} < \text{T}_{\text{sat}}$). In effect, the free parameter T_{cr} sets the thickness of the cloud layer, which can be adjusted to fit the observational data. Additionally, cloud particles are assumed to be a constant 0.01 μm in size.

The Allard et al. (2001, 2003, 2007) family of models perform a balancing between the sedimentation, condensation and coalescence timescales in each layer are compared to the mixing timescale. The equilibrium grain size is calculated by comparing the mixing and settling timescales and the condensation and coalescence timescales are computed for the grain size. The mixing timescale is then compared to these chemical timescales. If the growth timescale is faster than the mixing timescale, the grain size is recomputed to once which balances the growth and mixing timescales. Should the mixing timescale be larger than the growth timescale, the grain size is computed by balancing the mixing and condensation timescales. Depending on weather the mixing timescale is faster or slower than the compared timescale at each layer, the cloud structure is built up.

1.3.2 Kinetic Modelling

A microphysical approach for Brown Dwarfs/Exoplanets was presented by Helling et al. (2001); Woitke & Helling (2003) and subsequent papers Woitke & Helling (2004); Helling & Woitke (2006); Helling et al. (2008b), inspired by AGB stellar outflow dust formation modelling (e.g. Gail & Sedlmayr, 2014). This model was coupled to the stellar atmospheric model PHOENIX, and a suite of sub-stellar models, DRIFT-PHOENIX, across a wide parameter range (T_{eff}, [M/H], log g) was published by Witte et al. (2009). This method is 'top-down', in which the formation and growth of seed particles is followed at the top of the atmosphere to the bottom of the atmosphere. In their models, an appropriate species (the seed species) is chosen to homogeneously nucleate from the gas phase (Chapter 2), which provides the first surfaces for other materials to condense on top. Surface chemical reactions are then used to grow or evaporate the cloud particle material, dependent on the local thermochemical conditions and material specific supersaturation ratios. A static solution is then obtained by balancing the upward gas phase replenishment mixing rates with the chemical consumption rates. The local cloud particle number densities and grain sizes are therefore calculated directly from the microphysical chemistry, and all species are calculated in parallel. A key output of this model is that grains are therefore 'dirty', composed of many different materials, either growing or evaporating at any one instance. Integration is performed from the top of the atmosphere, downward, in contrast to most equilibrium models.

1.4 Contemporary 3D Methods and Models

In the past half decade, modelling and theoretical movement has been migrating away from 1D modelling (although still very much widely used), towards a full 3D description of exoplanet climates. Observational and theory papers are increasingly utilising and urging the use of 3D Global Circulation Models (GCMs) and Radiative-Hydrodynamic (RHD) models on objects, as observational evidence increasingly captures the spatial and temporal properties of exoplanet atmospheres, motivating the use of these models for investigating atmospheric properties and their observational signatures.

For example, Beatty et al. (2016) observed Kepler-17b in secondary eclipse using HST, and urged the community to perform 3D GCM cloud modelling of the object to test if cold trapping of TiO/ViO gas phase molecules could explain the unobserved temperature inversion, that is expected for hot Jupiters at high, 2000+ K, effective temperatures. The recent review by Heng & Showman (2015) identified a 3D consistent cloud formation model as a significant barrier to future progress in 3D exoplanet atmospheric modelling.

To date, most groups have focused on modelling the hot Jupiters, HD 189733b (e.g. Showman et al., 2009; Dobbs-Dixon & Agol, 2013), HD 209458b (e.g. Showman et al., 2009; Dobbs-Dixon et al., 2010; Rauscher & Menou, 2010; Heng et al., 2011; Mayne et al., 2014) and the warm sub-Neptune GJ 1214b (e.g. Kataria et al., 2014; Charnay et al., 2015a). These planets were chosen as they are some of the most characterised exoplanetary atmospheres to date. Codes differ in their implementation and hydrodynamic assumptions (see summary in Mayne et al. 2014) and radiative-transfer schemes (Amundsen et al., 2014) as well as the complexity with which gas and cloud chemistry is implemented. However, the overall global thermal structures and jet patterns remain similar for HD 209458b simulations (Heng & Showman, 2015).

Hot Jupiter simulations of HD 189733b (e.g. Showman et al., 2009; Dobbs-Dixon & Agol, 2013) have consistently reproduced offsets of maximum temperature to the East of the sub-stellar point, in line with Knutson et al. (2009) Spitzer thermal maps of atmospheres.

Kataria et al. (2016) modelled the hydrodynamics, thermal structure of nine hot Jupiters from the Sing et al. (2016) observing program. They post-process their simulations and examine the differences in the gas phase chemical equilibrium abundances between each planet. Other simulations have investigated the effect of eccentricity (Lewis et al., 2010, 2014), orbital distance (Showman et al., 2015), rotation (Rauscher & Kempton, 2014; Showman et al., 2015) and irradiation (Perna et al., 2012; Komacek & Showman, 2016) on the hydrodynamics of the atmosphere.

Thus far, investigations of atmospheric cloud properties of hot Jupiters using GCM/RHD simulations have not included a model for describing the formation of clouds. Parmentier et al. (2013) simulated the mixing of constant μm sized (a $= 0.1 \ldots 10$ μm) cloud tracer particles for HD 209458b. They showed that sub-micron sized grains are likely to not settle out of the upper atmosphere. Charnay et al. (2015b) simulated the warm sub-Neptune GJ 1214b. They applied a constant particle size approach for KCl[s] and ZnS[s] using the phase equilibrium condensate chemistry from Morley et al. (2012). Oreshenko et al. (2016) used a phase equilibrium scheme for $MgSiO_3$[s], Mg_2SiO_4[s], Fe[s], TiO[s] and Al_2O_3[s]. They post-process their GCM to model the optical and infrared wavelength phase curves of Kepler-7b (Demory et al., 2013). Parmentier et al. (2016) simulated a suite of hot Jupiter atmospheric models at equilibrium temperatures ranging from $T_{eq} = 1300 \ldots 2200$ K. They applied a phase equilibrium approach to model single, homogeneous species Fe[s], Al_2O_3[s], $MgSiO_3$[s], Cr[s], MnS[s] and Na_2S[s] clouds for prescribed, constant grain sizes. They then post-process their suite of models to investigate optical phase curve offsets in the Kepler bandpass. A common feature of the above cloud modelling approaches is the prescription of a constant grain size and homogeneous mineral composition of cloud particles.

1.5 Aim of Thesis

Despite nearly a decade of observational evidence of cloud particles in exoplanet atmospheres, a consistent, microphysical cloud formation model coupled to 3D radiative-hydrodynamics of exoplanet atmospheres has yet to be developed. The modelling of clouds is a multi-dimensional. multi-topic problem. This thesis outlines a first step towards a holistic, 3D approach to modelling cloud particles in exoplanetary atmospheres, split into three main themes. First, investigating the chemical processes that govern cloud formation in a 3D environment. Second, investigating the feedback of clouds on the dynamics, radiation and chemistry of an exoplanet atmosphere. Third, investigating the 3D propagation of radiation in an inhomogeneous cloudy environment and its effect on observable properties.

In Chapters 2 the kinetic theory of cloud formation in exoplanet atmospheres is summarised. Chapter 3 presents the results and discussion of the 1D version of the model, applied to the hot Jupiter HD 189733b, and attempts to extrapolate to 3D cloud structures. Chapter 4 presents a HD 189733b 3D RHD model, consistently coupled with a time-dependent 3D cloud formation module. Chapter 5 presents a 3D Monte Carlo radiative transfer for post-processing our 3D RHD results and comparing to observations. Chapter 6 contains potential future projects using the tools outlined in the previous chapters. Lastly, a summary and conclusion is found in Chapter 7.

2

Cloud Formation in Exoplanet Atmospheres

2.1 Introduction

The formation of cloud particles is fundamentally a chemical process whereby an initial supersaturated gas phase mixture is transitioned into a solid material. At a macroscopic level, the thermochemical stability or instability of a material i is characterised by the temperature dependent supersaturation ratio $S(T)$ given by

$$S(T) = \frac{p_{i,par}}{p_{i,vap}} \tag{2.1}$$

where $p_{i,par} = n_i kT$ is the partial pressure of species i, with k the Boltzmann constant and T the local gas temperature, and $p_{i,vap}$(T) the vapour pressure of species i, dependent on the local gas temperature. Should S > 1, it is energetically favourable at the local thermochemical environment for the material to condense or grow into a liquid or solid form. While if S < 1, it is energetically unfavourable to condense, and likely to evaporate from liquid and solid forms into gas phase particles. A balanced, equilibrium situation occurs when $S = 1$, where neither growth nor evaporation are energetically favoured.

On Earth, water clouds are formed when small seed particles called Aitken nuclei, usually made of sand, ash or ocean sea salt spray are lofted upwards by atmospheric winds to upper atmospheric regions where supersaturated water vapour resides. The surface of these seed particles provides an efficient catalyst to the formation of liquid or ice water droplets. For Earth clouds only a slightly supersaturation greater than unity (S $\sim$ 1.01) is required to efficiently form clouds in the presence of seed particle surfaces (Korolev & Mazin, 2003). While, without the seed particle surface, an order of magnitude larger (S $\sim$ 400) supersaturation ratio would be required to condense water clouds. The timescale to form clouds is also on the order of seconds-minutes in the presence of seed particles, as without these surfaces, cloud formation is likely to take on the order of hours to form.

Unlike Earth water clouds, exoplanet atmospheric clouds are theorised to be formed of mineral materials such as iron and silicates. Our kinetic theory of cloud formation in exoplanet atmospheres traces its routes to theories developed for describing cloud formation in Brown Dwarf atmospheres from the 1990's and 2000's. In this chapter, we summarise the chemical processes of nucleation and growth/evaporation in the context of hot Jupiter exoplanet cloud formation. We provide an overview of the kinetic cloud framework used in later chapters, and details of the size-distributions of cloud particles. Lastly, we summarise the calculation of cloud particle opacities using effective medium theory and Mie theory.

2.2 Nucleation

Hot Jupiter exoplanets lack solid or liquid surface geophysical processes to provide seed particles as the first step in the cloud formation process. Therefore, the first surfaces must form from the original gas phase materials present in the atmosphere. The process of nucleation is defined as the conversion of gas phase material to solid particles via a chemical process. An example of this process and an experiment undertaken by many high school students and chemistry hobbyists is the growing of crystals using material dissolved above supersaturation levels. For homogenous nucleation (i.e. considering only a single molecule monomer species) this process depends on the saturation properties of the material (i.e. temperature and chemical abundance). Starting from a single monomer (or unit) molecule of size $\sim$ 0.1 nm, more monomers are added in succession through a chemical pathway of interactions through cluster space. Figure 2.1 from Lee et al. (2015b) shows examples from computational chemistry literature of potential cluster geometries of $(TiO_2)_N$, N = 1—10 monomers.

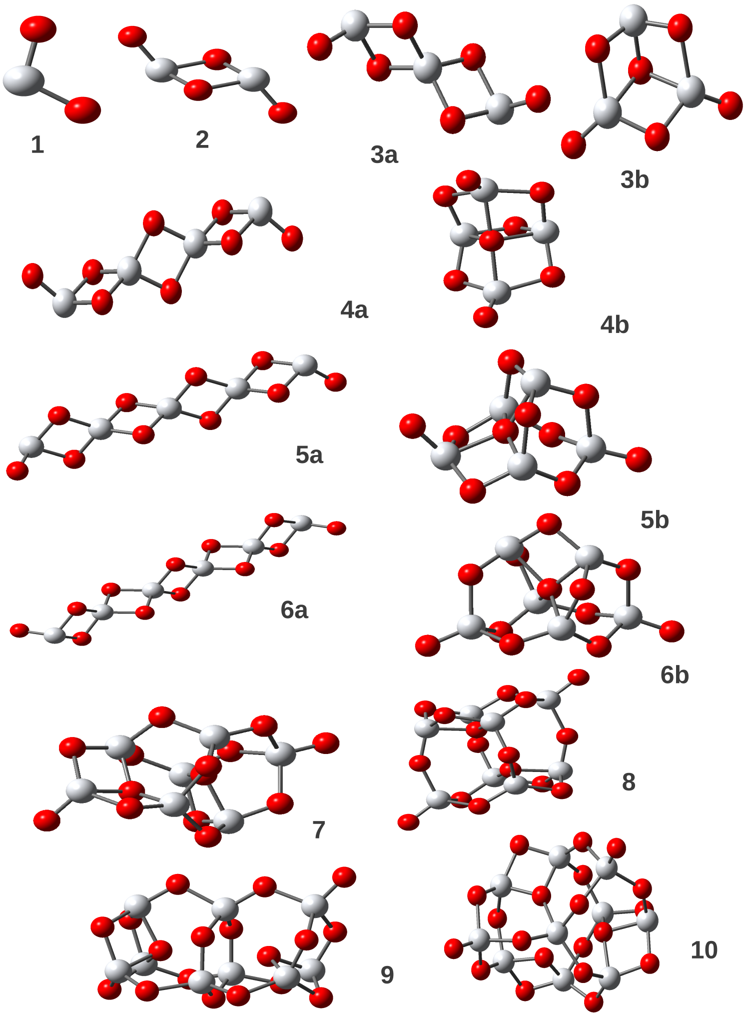

Figure 2.1: Figure from Lee et al. (2015b): Geometry of the $(TiO_2)_N$ structures calculated. Molecules with label 'a' are the molecules calculated by Jeong et al. (2000) and those labeled 'b' or unlabelled are the current most stable cluster geometries (Calatayud et al., 2008; Syzgantseva et al., 2011). Silver/grey balls represent Ti atoms while red represent O atoms.

Eventually, the chemical pathway reaches a critical cluster size, N_*, which represents the monomer addition that is least efficient in the chemical pathway and the bottleneck to the nucleation process. The aim of classical nucleation theory is to calculate the flux or rate of particles that are able to grow through this critical cluster size and on to the larger seed particle sizes of $\sim$ 1000 monomer sizes. We summarise below the main methodology of classical nucleation theory, we refer the reader to Helling & Fomins (2013), Gail & Sedlmayr (2014) and Lee et al. (2015b) for more general details and reviews.

We consider the stationary nucleation rate, J_* [cm^{-3} s^{-1}], of a homogenous, homomolecular gas phase material given by

$$J_*^c(t) = \frac{\overset{\circ}{f}(N_*)}{\tau_{gr}(r_i, N_*, t)} Z(N_*) S(T) \cdot \exp\{(N_* - 1)\ln S(T)\} \tag{2.2}$$

with N$_*$ the critical cluster size. The equilibrium cluster size distribution, $\overset{\circ}{f}(N)$ [cm^{-3}], can be considered as a Boltzmann-like distribution in local thermal equilibrium,

$$\overset{\circ}{f}(N) = \overset{\circ}{f}(1) \exp\left(-\frac{\Delta G(N)}{RT}\right), \tag{2.3}$$

where $\overset{\circ}{f}(1)$ [cm^{-3}] is the equilibrium number density of the monomer (smallest cluster unit like TiO_2 or SiO), $\Delta G(N)$ [kJ mol^{-1}] is the Gibbs free energy change due to the formation of cluster of size N from the saturated vapour at temperature T and R the molar gas constant. The rate of growth for each individual cluster of size N is

$$\tau_{\rm gr}^{-1}(r_{\rm i}, N, t) = A(N)\alpha(r_{\rm i}, N) v_{\rm rel}(n_{\rm f}(r_{\rm i}), N) n_{\rm f}(r_{\rm i}, t), \tag{2.4}$$

where $A(N) = 4\pi a_0^2 N^{2/3}$ [cm^2] is the reaction surface area of a N-sized cluster, N is the number of monomers in a cluster, a_0 the hypothetical monomer radius, α is the efficiency of the reaction (assumed to be 1); $v_{\rm rel}$ [cm^{2}s^{-1}] is the relative velocity between a monomer and the cluster, and $n_{\rm f}$ [cm^{-3}] is the particle density of the molecule for the growth (forward) reaction ($\equiv \overset{\circ}{f}(1)$). The relative velocity is approximated by the thermal velocity

$$v_{\rm rel} = \sqrt{\frac{kT}{2\pi\bar{\mu}}} \approx \sqrt{\frac{kT}{2\pi m_{\rm x}}} \tag{2.5}$$

with $\bar{\mu} = 1/(1/m_x - 1/m_V)$, where m_x is the mass of the monomer molecule (e.g. TiO_2) and m_V the mass of a grain with volume V. For macroscopic grains, $m_V \ll m_x$, hence $\bar{\mu} \approx m_x$. ΔG(N) can be expressed by a relationship to the standard molar Gibbs free energies in reference state '$\circleddash$' (measured at a standard gas pressure and gas temperature) of formation for cluster size N

$$\Delta G(N) = \Delta_{\mathrm{f}}^{\ominus} G(N) + RT \ln\left(\frac{\overset{\circ}{p}_{sat}(T)}{p^{\ominus}}\right) - N\Delta_{\mathrm{f}}^{\ominus} G_1(s), \tag{2.6}$$

where the $^{\ominus}$ symbol represents a quantity defined at a standard reference value. Combining Eqs. 2.3 and 2.6 results in

$$\Delta G(N) = \Delta_{\mathrm{f}}^{\ominus} G(N) - \Delta_{\mathrm{f}}^{\ominus} G(1) - (N-1)\Delta_{\mathrm{f}}^{\ominus} G_1(s) \tag{2.7}$$

where the right hand side contains standard reference state values only $\Delta_{\mathrm{f}}^{\ominus} G(\mathrm{N})$ - standard Gibbs free energy of formation of cluster size N, $\Delta_{\mathrm{f}}^{\ominus} G(1)$ - standard Gibbs free energy of the monomer, $\Delta_{\mathrm{f}}^{\ominus} G_1(\mathrm{s})$ - standard Gibbs free energy of formation of the solid phase) which can be found by experiment or computational chemistry.

Classical nucleation theory assumes that the detailed knowledge about $\Delta G(\mathrm{N})$ can be encapsulated by the value of the surface tension, σ_{∞}, of the macroscopic solid such that

$$\frac{\Delta G(N)}{RT} = -N\ln(S) + \theta_{\infty} N^{2/3} \quad \text{with} \quad \theta_{\infty} = \frac{4\pi a_0^2 \sigma_{\infty}}{k_b T}. \tag{2.8}$$

The dependence of the surface energy on cluster size is therefore neglected. The Zeldovich factor (contribution from Brownian motion to nucleation rate) in Eq. 2.2 is

$$Z(N_*) = \left(\frac{\theta_{\infty}}{9\pi(N_*-1)^{4/3}} \frac{(1+2(\frac{N_f}{N_*-1})^{1/3})}{(1+(\frac{N_{\mathrm{f}}}{N_*-1})^{1/3})^3}\right)^{1/2}. \tag{2.9}$$

The nucleation rate can now be expressed as

$$J_*^c(t) = \frac{\overset{\circ}{f}(1,t)}{\tau_{gr}(1,N_*,t)} Z(N_*) \exp\left((N_*-1)\ln S(T) - \frac{\Delta G(N_*)}{RT}\right). \tag{2.10}$$

2.2.1 Modified classical nucleation theory

Modified nucleation theory was proposed by Draine & Salpeter (1977) and Gail et al. (1984). By taking into account the curvature on the surface energy for small clusters (Gail et al., 1984).

Equation 2.8 changes to

$$\frac{\Delta G(N)}{RT} = \theta_\infty \frac{N-1}{(N-1)^{1/3} + N_f^{1/3}} \tag{2.11}$$

where N_f is a fitting factor representing the particle size at which the surface energy is reduced to half of the bulk value. This fitting factor allows to calculate a critical cluster N_* as

$$N_* - 1 = \frac{N_{*,\infty}}{8}\left(1 + \sqrt{1 + 2\left(\frac{N_f}{N_{*,\infty}}\right)^{1/3}} - 1\left(\frac{N_f}{N_{*,\infty}}\right)^{1/3}\right)^3 \tag{2.12}$$

with

$$N_{*,\infty} = \left(\frac{\frac{2}{3}\theta_\infty}{\ln S(T)}\right)^3 . \tag{2.13}$$

The nucleation process is perhaps the most critical step to the cloud formation, as without the presence of seed particles nucleated from the gas phase, cloud formation becomes chemically inefficient, for example, for water clouds without seed particles the required supersaturation ratio to produce clouds occurs at $S > 1000$, while with seed particles present $S \sim 1.01$ for cloud formation to occur.

A related but important concept in nucleation theory is heterogenous nucleation, where multiple species combine to form the seed particles. Goumans & Bromley (2012) propose a heterogenous nucleation pathway of Mg, Si and O containing species to form $Mg_2Si_2O_6$ clusters. A full description of heterogenous nucleation is beyond the scope of this thesis and an overview can be found in Gail & Sedlmayr (2014).

An alternative source of atmospheric seed particles is the suggestion that meteoritic accretion could provide surfaces for the clouds formation process. An example of this is Earth's noctilucent clouds, which can form from the debris of meteorite breakup in the upper atmosphere. Thus far, this cloud formation route has not been studied in the context of exoplanet atmospheres.

2.3 Growth and Evaporation

Once a seed particle surface is present, either by the nucleation process or from other source, other gas phase material may condense on the surface, growing the cloud particle larger. Conversely, should a solid phase material present on the surface of the grain become thermally unstable (S < 1) at some point in the particle's lifetime, the material will begin to evaporate into the gas phase, reducing the grain volume and mass. The growth of a material on the surface of a grain occurs by the processing of chemical reactions of gas phase species on the surface of the grain. For example, the formation of $MgSiO_3[s]$

$$Mg + SiO + 2H_2O \rightarrow MgSiO_3[s] + H_2. \tag{2.14}$$

Conceptually, this process may be thought of as two or more gas phase species diffusing around the surface of the grain until they meet. The surface of the grain then provides a favourable reaction site for the reaction to occur. This process results in 'islands' of stable material together on the surface of the grain (Woitke & Helling, 2004). It is important to note, that many solid species (such as $MgSiO_3[s]$) do not occur naturally in the gas phase and can only be formed by such chemical processes; while other material (e.g. SiO, H_2O) can be abundant in the gas phase and condense directly, represented by

$$Y \rightarrow Y[s]. \tag{2.15}$$

The rate of the surface chemical reaction depends directly on the abundance of the key species taking part in the reaction. This is defined as the gas phase species that is least abundant in the gas phase compared to its reactant. In the example reaction above (Eq. 2.14, this would be the minimum abundance between Mg and SiO in the gas phase. In the evaporation process a material is thermochemically unstable (S < 1), and solid material evaporates into the gas phase. This process can be thought of as the reverse of the growth reactions, with the solid material breaking up into two or more gas phase constituent parts. This returns elements to the gas phase, previously locked up in the cloud particles. A list of Oxygen rich surface chemical reactions can be found in Helling et al. (2008b). Carbon rich cloud formation chemical reactions can also be considered, such as those in Helling et al. (2016a).

2.4 Kinetic Modelling Framework

By carefully considering each surface chemical reaction, the kinetic framework of cloud formation is built up. The net growth/evaporation velocity $\chi^{\rm net}(\vec{r})$ [cm s^{-1}] of a grain due to chemical surface reactions (Gail & Sedlmayr, 1986; Helling & Woitke, 2006) is given by

$$\chi^{\mathrm{net}}(\vec{r}) = \sqrt[3]{36\pi}\sum_{s}\sum_{r=1}^{R}\frac{\Delta V_r^s n_r^{\mathrm{key}} v_r^{\mathrm{rel}} \alpha_r}{\nu_r^{\mathrm{key}}}\left(1-\frac{1}{S_r}\frac{1}{b_{\mathrm{surf}}^s}\right), \tag{2.16}$$

where r is the index for the chemical surface reaction, ΔV_r^s the volume increment of the solid s by reaction r, n_r^{key} the particle density of the key reactant in the gas phase, v_r^{rel} the relative thermal velocity ($v_r^{\mathrm{rel}} = \sqrt{kT/2\pi m_r}$) of the gas species taking part in reaction r, α_r the sticking coefficient of reaction r and ν_r^{key} the stoichiometric factor of the key reactant in reaction r. S_r is the reaction supersaturation ratio (Helling & Woitke, 2006) and $1/b_{\mathrm{surf}}^s = \mathrm{V_s}/\mathrm{V_{tot}}$ the volume of solid s, V_s, to the total grain volume containing all species $\mathrm{V_{tot}} = \sum_s \mathrm{V}_s$.

2.4.1 Conservation of Elements

The local gas-phase composition is an input for the cloud formation process as it determines (along with temperature) the cloud formation nucleation and growth/evaporation rates. The elements involved in the cloud formation process are altered by depletion or replenishment depending on the dominating cloud formation processes (nucleation, growth, evaporation). The depletion/enrichment of gas phase elements $\varepsilon_i(\vec{r})$ (abundance ratio of element i to Hydrogen; $\varepsilon_i(\vec{r}) = n_i/n_{\langle H\rangle}$) by cloud particle growth/evaporation (Helling & Woitke, 2006) is given by

$$\begin{aligned}\frac{\partial\left(n_{\langle H\rangle}\varepsilon_i\right)}{\partial t} + \nabla\cdot\left(n_{\langle H\rangle}\varepsilon_i\mathbf{u}_{\mathrm{gas}}\right) = &-\nu_{x,0}N_l J(V_l)\\ &- \sqrt[3]{36\pi}\rho L_2\sum_{r=1}^{R}\frac{\nu_{x,s} n_r^{\mathrm{key}} v_r^{\mathrm{rel}}\alpha_r}{\nu_r^{\mathrm{key}}}\left(1-\frac{1}{S_r}\frac{1}{b_{\mathrm{surf}}^s}\right),\end{aligned} \tag{2.17}$$

where i is the index of the element that contributes to the cloud formation process and $n_{\langle H\rangle}$ the local total number density of hydrogen. The first r.h.s. terms describes the consumption of elements from the nucleation process. The second r.h.s. term denotes the source (evaporation) and sink (growth) of elements as a result of cloud particle chemical surface reactions. The second l.h.s. term describes the advection of $n_{\langle H\rangle}$ $\varepsilon_i(\vec{r})$ through space at the local gas velocity $\mathbf{u}_{\mathrm{gas}}(\vec{r})$.

2.5 Size Distribution: Bin Method

Fundamental to the kinetic method of cloud formation is the concept of a size-distribution of cloud particles. In an atmosphere, the local local cloud particles may be a multitude of particle sizes, ranging from seed particle sizes (∼ 1 nm) to micron or larger sizes. The local number of each particle at a particular size is described by the size-distribution, $f(a)$ [cm^{-3} cm^{-1}].

The local number density of cloud particles, $n_{\rm d}$ is given by the integral over all particle sizes from the seed particle size.

$$n_{\rm d} = \int_{a_{\rm seed}}^{\infty} f(a) da. \tag{2.18}$$

Generally, the integral part is split into appropriately sized bins or 'size bins' with a maximum cloud particle radius, resulting in

$$n_{\rm d} = \sum_{b=1}^{N_b} n_d(b). \tag{2.19}$$

where b is a bin index, N$_b$ the number of bins and n_d(b) [cm^{-3}] the number density of cloud particles present in bin b. Using the nucleation and growth equations above, the flux of particles into and out of each bin is calculated and integrated in time (e.g. Gail & Sedlmayr, 2014). Usually a large number of bins is required (10-100) to accurately capture the size-distribution of cloud particles. This makes the bin method computationally inefficient for large scale hydrodynamical modelling of cloud particles. However, the bin method can fully capture the size properties of the cloud particles when interaction between cloud particle sizes is important.

2.6 Size Distribution: Method of Moments

Instead of tracking the population of individual size bins, weighted integrated properties of the size distribution can be calculated, called the Moment Method or Method of Moments. This greatly simplifies the complexity of the modelling process without sacrificing chemical detail, and avoids some of the more tricky parts of modelling with the bin method. However, since the moments are integrated properties, the shape of the size distribution is lost. The shape can be reconstructed assuming a shape after the simulation has been performed (Sect. 2.6.2).

To describe the cloud formation process Woitke & Helling (2003, 2004); Helling & Woitke (2006); Helling et al. (2008b) derive a set of dust moment equations. The dust volume moments $L_j(\vec{r})$ [cm^j g^{-1}] ($j = 0, 1, 2, 3$) are the local integrated particle size distribution, weighted by a power of the grain volume $V^{j/3}$, defined as

$$\rho_{\rm gas} L_j(\vec{r}, t) = \int_{V_l}^{\infty} f(V, \vec{r}, t) V^{j/3} {\rm d}V, \tag{2.20}$$

where $f(V, \vec{r})$ [cm^{-6}] is the distribution of particles in volume space and V_l [cm^3] the volume of a seed particle. The moments can also be expressed weighted by the particle radius a rather than the volume ($K_j(\vec{r}, t)[cm^j]$), given by (e.g. Gail & Sedlmayr, 2014)

$$K_j(\vec{r}, t) = \int_{a_l}^{\infty} f(a, \vec{r}, t) a^j {\rm d}a, \tag{2.21}$$

which is useful for more easily reconstructing the size distribution and other cloud properties. The conservation equation of dust volume moments is given by (Woitke & Helling, 2003)

$$\frac{\partial \left(\rho_{\rm gas} L_j\right)}{\partial t} + \nabla \cdot \left(\rho_{\rm gas} L_j \mathbf{u}_{\rm d}\right) = V_l^{j/3} J_* + \frac{j}{3} \chi^{\rm net} \rho_{\rm gas} L_{j-1}, \tag{2.22}$$

which has the same conservation transport equation structure as hydrodynamic transport conservation equations (e.g. Navier-Stokes). No prior assumptions about the particular grain size distribution or grain sizes are required to compute the number density of cloud properties.

The composition of material forming on the grain mantle changes as a result of local chemical and thermodynamic conditions and the thermal stability of each material in those conditions. The volume of a specific solid mineral s depends on the growth/evaporation rate of that material. The volume of each material s can be described by a separate moment conservation equation for the third dust moment, $L_{3,s}(\vec{r})$ [cm^3 g^{-1}], (Helling et al., 2008b)

$$\frac{\partial \left(\rho_{\rm gas} L_{3,s}\right)}{\partial t} + \nabla \cdot \left(\rho_{\rm gas} L_{3,s} \mathbf{u}_{\rm d}\right) = V_{l,s} J_* + \chi_s^{\rm net} \rho_{\rm gas} L_2, \tag{2.23}$$

where the growth velocity of the solid s, $\chi_s^{\rm net}(\vec{r})$ [cm s^{-1}], is given by

$$\chi_s^{\rm net}(\vec{r}) = \sqrt[3]{36\pi}\sum_{r=1}^{R}\frac{\Delta V_r^s n_r^{\rm key} v_r^{\rm rel}\alpha_r}{\nu_r^{\rm key}}\left(1 - \frac{1}{S_r}\frac{1}{b^s_{\rm surf}}\right). \tag{2.24}$$

The local volume fraction $\mathrm{V}_s/\mathrm{V}_{\rm tot}$ of each species s is calculated from the $L_{3,s}(\vec{r})$ dust moment using the identity (Woitke & Helling, 2004; Helling et al., 2008b)

$$\sum_s L_{3,s} = L_3, \sum_s V_{\rm s} = V_{\rm tot}. \tag{2.25}$$

By evolving a set of the dust volume moments in time across a 3D grid, the chemical and advective processes of cloud formation are captured by the scheme. In general, the moment scheme is more computationally efficient than tracking the evolution of several bins. However, information, and therefore accuracy, is lost on the minutia of the size distribution shape. Despite this, the moment method is a powerful tool, especially for 3D GCM/RHD modelling which requires computational efficiency but also reasonable accuracy. Additionally, the same chemical scheme is used for both the bin and moment methods. Interesting chemical details and material properties are therefore well represented by the moment method.

2.6.1 Integrated Distribution Properties

As integrated quantities, mean properties of the size distribution can be recovered from the dust moment solutions. By taking different ratios of the volume integrated quantities, L_j [cm^j g^{-1}], many local mean properties of the size distribution can be calculated, representing different physical properties.

The total cloud particle number density, n_d [cm^{-3}],

$$n_d = \rho L_0. \tag{2.26}$$

The mean cloud particle size, $\langle a \rangle$ [cm],

$$\langle a \rangle = \left(\frac{3}{4\pi}\right)^{1/3}\frac{L_1}{L_0}. \tag{2.27}$$

The mean cloud particle area, $\langle A \rangle$ [cm^2],

$$\langle A \rangle = (36\pi)^{1/3} \frac{L_2}{L_0}. \tag{2.28}$$

The mean cloud particle volume, $\langle V \rangle$ [cm^3],

$$\langle V \rangle = \frac{L_3}{L_0}. \tag{2.29}$$

Another important derivable quantity is the effective cloud particle radius, $a_{\rm eff}$ [cm] (Hansen & Travis, 1974), which is the area weighted mean radius given by

$$a_{\rm eff} = \left(\frac{3}{4\pi}\right)^{1/3} \frac{L_3}{L_2}, \tag{2.30}$$

which is useful for characterising the mean opacity and scattering properties of the size distribution, since the opacity of the distribution scales $\sim$a^2 (Sect. 2.8.2).

2.6.2 Reconstructing the Size Distribution

Given specific shape information a size distribution can be reconstructed from the moment solutions by *assuming* a suitable arithmetic distribution shape to fit to the moment data. The relations between moments represent a mathematical property of the size-distribution, for example, the expectation value, $E[X]$, is approximately equal to the mean cloud particle size $\langle a \rangle$, and the variance, $Var[X]$, approximately equal to the mean cloud particle area $\langle A \rangle$. Should they be needed, dimensionless parameters using higher moments can be used, for example, the skewness $Skew[X] = L_3/L_2^{3/2}$ and kurtosis $Kurt[X] = L_4/L_2^2$. However, these higher moments are generally not required to be provided for reconstruction, except to investigate very specific shape distributions. Figure 2.2 presents a graphical representation of each of the reconstructed grain size distribution (GSD) using data from Chapter 4.

Log-normal distribution

A widely used GSD used in both Earth and exoplanet cloud particle studies is the log-normal distribution, which is a Gaussian or Normal distribution in log-space. This is given by (e.g Stark et al., 2015)

$$f(a) = \frac{N_0}{a\sigma\sqrt{2\pi}} \exp\left[-\frac{(\ln(a) - \mu)^2}{2\sigma^2}\right], \tag{2.31}$$

Where N_0 is the total cloud particle density, a the sampled grain size, μ the natural logarithm of the distribution mean and σ the natural logarithm of the distribution variance. The parameters μ and σ are estimated from the kinetic cloud formation results by (Stark et al., 2015)

$$\mu = \ln\left[\frac{\langle a\rangle^2}{\sqrt{\langle A\rangle - \langle a\rangle^2}}\right], \tag{2.32}$$

and

$$\sigma = \frac{1}{2}\ln\left(\frac{\langle A\rangle}{\langle a\rangle^2} + 1\right), \tag{2.33}$$

where $\langle A\rangle$ is the mean cloud particle area and $\langle a\rangle$ the mean cloud particle radius. This distribution is mostly used to describe Earth rain droplet clouds where collisions, as well as condensation grow the particles as they fall through the atmosphere. This results in a wider distribution, with the same number of particles either side of a mode value in log-space. This is perhaps the most 'balanced' distribution, with a mix of large and small grains in equal proportions around a mode value.

Gaussian distribution

The Gaussian distribution is given by

$$f(a) = \frac{N_0}{a\sigma\sqrt{2\pi}} \exp\left[-\frac{(a - \mu)^2}{2\sigma^2}\right] \tag{2.34}$$

The parameters μ and σ are estimated from the cloud formation results as

$$\mu = \frac{\langle a\rangle^2}{\sqrt{\langle A\rangle - \langle a\rangle^2}}, \tag{2.35}$$

and

$$\sigma = \left(\frac{\langle A\rangle}{\langle a\rangle^2} + 1\right)^2. \tag{2.36}$$

This distribution, as a linear distribution over many order of magnitude, skews the distribution towards smaller cloud particle sizes. A characteristic of this distribution is that the mode cloud particle size is equal to the mean cloud particle size.

Inverse Gamma distribution

The inverse Gamma distribution is mostly used as an alternative to the log-normal distribution for Earth clouds due its similar profile at larger grain sizes. It is characterised by a power-law ingress with an exponential egress at the mode value.

$$f(a) = \frac{N_0}{\Gamma(\alpha)}\beta^{\alpha}a^{-\alpha-1}\exp\left[-\frac{\beta}{a}\right] \tag{2.37}$$

with parameters α and β found from the definitions of the mean and variance of the distribution, and from the cloud formation results, from

$$E[X] = \langle a\rangle = \frac{\beta}{\alpha-1}, \tag{2.38}$$

for the mean and

$$Var[X] = \langle A\rangle = \frac{\beta^2}{(\alpha-1)^2(\alpha-2)}, \tag{2.39}$$

for the variance. The distribution is skewed towards larger grain sizes, representing a physical process that can efficiently grow grains to larger sizes.

Gamma distribution

The gamma distribution is the non-inverted version of Eq. 2.37.

$$f(a) = \frac{N_0}{\Gamma(\alpha)}\beta^{\alpha}a^{\alpha-1}\exp[-\beta a] \tag{2.40}$$

with parameters α and β derived from the mean and variance given by

$$E[X] = \langle a \rangle = \frac{\alpha}{\beta}, \tag{2.41}$$

and

$$Var[X] = \langle A \rangle = \frac{\alpha}{\beta^2}. \tag{2.42}$$

The distribution is characterised by an exponential rise to a mean point, and a power law falloff. Suggestive of a growth process that tapers off with increased particle size.

Rayleigh distribution

The Rayleigh size distribution is a special case of a gamma distribution given by

$$f(a) = \frac{N_0 a}{\sigma^2} \exp\left[-\frac{a^2}{2\sigma^2}\right], \tag{2.43}$$

where σ can be derived from many distribution properties

$$\langle a \rangle = \sigma\sqrt{\frac{\pi}{2}}, \tag{2.44}$$

which is mainly characterised by a steep decline from the mode value. It represents a physical process that prevents particles from growing efficiently to larger sizes, skewing the distribution towards smaller particle sizes. This distribution is commonly used to model the size distribution resultant from industrial grinding of rock material, where larger particles are ground down into smaller ones, resulting in a sharp decline in the numbers of large grains present in the distribution.

Potential exponential/modified Gamma

To investigate the opacity of cloud particles in brown dwarf atmospheres, Helling et al. (2008b) proposed a potential exponential distribution in the form

$$f(a) = a^B \exp\left[A - Ca\right], \tag{2.45}$$

which can be recast into a modified gamma distribution form to

$$f(a) = \frac{\langle a \rangle N_0}{\Gamma(\alpha)} C^{\alpha} a^{\alpha-2} \exp\left[-Ca\right]. \tag{2.46}$$

where the parameters α, A, B and C can be derived from the relations

$$\alpha = B + 2, \tag{2.47}$$

$$A = \ln K_1 + (B+2)\ln C - \ln\Gamma(B+2), \tag{2.48}$$

$$B = \frac{2K_1K_3 - 3K_2^2}{K_2^2 - K_1K_3}, \tag{2.49}$$

$$C = (B+2)\frac{K_1}{K_2}. \tag{2.50}$$

where K$_j$ is the size distribution moments in radius space (Eq. 2.21)

Hansen Distribution

The Hansen distribution (Hansen, 1971; Hansen & Travis, 1974) is a modified gamma distribution, primarily used to describe Earth based clouds, which makes use of the effective particle size and effective particle variance. The dimensionless effective cloud particle variance, $\nu_{\rm eff}$ (Hansen & Travis, 1974), is the normalised variance about the effective radius, $a_{\rm eff}$, formally defined by

$$\nu_{\rm eff} = \frac{\int_0^{\infty}(a - a_{\rm eff})^2 \pi a^2 f(a) {\rm d}a}{a_{\rm eff}^2 \int_0^{\infty} \pi a^2 f(a) {\rm d}a}, \tag{2.51}$$

expanding the terms and using the definition of the cloud moments in radius space (i.e. K_j, Eq. 2.21), in terms of the local particle moment values, reduces to

$$\nu_{\text{eff}} = \frac{K_4 - 2a_{\text{eff}}K_3 + a_{\text{eff}}^2 K_2}{a_{\text{eff}}^2 K_2}. \tag{2.52}$$

If the 4th moment K_4 is unknown, it may be reasonable from the definition of the fourth moment to assume that $K_4 \approx a_{\text{eff}}\, K_3$, retaining the dimensionality of the fourth moment. This implicitly assumes that the kurtosis $\propto a^4$, or 'knee' of the distribution is well peaked around the effective radius. Using this approximation the effective cloud particle variance then becomes

$$\nu_{\text{eff}} = \frac{a_{\text{eff}}K_3 - 2a_{\text{eff}}K_3 + a_{\text{eff}}^2 K_2}{a_{\text{eff}}^2 K_2}. \tag{2.53}$$

In many cases ν_{eff} is assumed to be $= 0$, which is equivalent to a mono-disperse size distribution.

The Hansen distribution is given by

$$f(a) = \frac{N_0}{\Gamma[(1-2\beta)/\beta]}(\alpha\beta)^{(2\beta-1)/\beta} a^{(1-3\beta)/\beta} \exp[-a/(\alpha\beta)], \tag{2.54}$$

where α is the effective particle size a_{eff} (Eq. 2.30) and β is the effective variance ν_{eff} (Eq. 2.51). This distribution has also recently been used in Brown Dwarf investigations (Hiranaka et al., 2016).

The Helling et al. (2008b) and Hansen (1971) modified gamma distributions are similar approaches, in that they attempt to fit a distribution from the moment solutions by using the variance about a mean value. For the Helling et al. (2008b) distribution this is the mean particle size $\langle a \rangle$, while for the Hansen (1971) distribution it is the effective particle size a_{eff}. This results in the Hansen distribution requiring an additional higher moment (K_4) to fit compared to the potential exponential.

2.7 Cloud Particle Settling

A critical ingredient for any clouds model is estimating how fast particles vertically settle or rain out from the atmosphere. This is denoted by the vertical velocity, or drift velocity of the cloud particles in the atmosphere. The relative velocity of gas and dust is given by the drift velocity $\mathbf{v}_{\text{dr}}(\vec{r})$ [cm s^{-1}] defined as (Woitke & Helling, 2003)

$$\mathbf{v}_{\rm dr}(\vec{r}) = \mathbf{u}_{\rm d}(\vec{r}) - \mathbf{u}_{\rm gas}(\vec{r}), \tag{2.55}$$

where $\mathbf{u}_{\rm gas}(\vec{r})$ [cm s^{-1}] is the gas hydrodynamic velocity.

The dimensionless Knudsen number, Kn, is given as the ratio between the mean free path of the gas molecules and the radius of the cloud particle, given by

$$Kn = \frac{l}{a}, \tag{2.56}$$

where l is the mean free path of the gas and a the a the radius of the cloud particle. For Kn $\gg$ 1, the mean free path of surrounding gas particle is larger than the cloud particle radius. In this regime, gas freely streams across the grain surface. For Kn $\ll$ 1, the mean free path is small compared to the cloud particle radius. In this regime, gas interacting with the cloud particles diffuse around the grain surface. These two limits describe different interactions of the gas with solid phase, which results in differing settling behaviour.

Following the analysis in Woitke & Helling (2003), the mean equilibrium drift velocity $\langle \overset{\circ}{\mathbf{v}}_{\rm dr}\rangle(\vec{r})$ [cm s^{-1}] in the large Knudsen number regime (Kn $\gg$ 1) is given by

$$\langle \overset{\circ}{\mathbf{v}}_{\rm dr}\rangle(\vec{r}) = -\frac{\sqrt{\pi}}{2}\frac{g\rho_{\rm d}\langle {\rm a}\rangle}{\rho_{\rm gas}c_{\rm T}}\mathbf{e}_{\rm r}, \tag{2.57}$$

where $\rho_{\rm d}$ [g cm^{-3}] is the bulk (material) dust density, $c_{\rm T}$ [cm s^{-1}] the speed of sound, $g\mathbf{e}_{\rm r}$ [cm s^{-2}] the gravitational acceleration in the radial direction and $\langle {\rm a}\rangle(\vec{r})$ [cm] the local mean grain size.

Ackerman & Marley (2001) and Parmentier et al. (2013) apply the Stokes-Cunningham settling velocity, the velocity of the dust component only, used for low Reynolds number flows. This is given by

$$v_d = \frac{2\beta a^2 g(\rho_{gas} - \rho_d)}{9\eta}, \tag{2.58}$$

where η is the kinematic viscosity of the gas mixture and β is the Knudsen number dependent Cunningham slip factor

$$\beta = 1 + K_N(1.256 + 0.4{\rm e}^{-1.1/{\rm K_N}}). \tag{2.59}$$

A difference between this formalism and the Woitke & Helling (2003) is that positive values of

v_d are permitted if the density of the gas is greater than the cloud particle bulkd density (ρ_{gas} $> \rho_d$).

2.8 Cloud Opacity and Scattering Properties

Critical to the observational and modelling properties of exoplanet atmospheres is the significant opacity that cloud particles can give to the atmosphere. Clouds are a major source of opacity, which in turn affects the observable properties of the planet from the scattering of incident starlight to the absorption of light which affect the temperature structure of the planet through greenhouse and anti-greenhouse radiative effects.

2.8.1 Optical Constants and Effective Medium Theory

Solid materials of differing composition will interact differently with impinging photons, dependent on the wavelength of light. For example, glass (silicon) is transparent at optical wavelengths, but absorbing at UV, while iron (Fe) is a dark material that absorbs light across much of the electromagnetic spectrum. The precise interaction of photons with a material is contained in the material optical constants (n, k), which details the absorption and scattering properties of a material. When calculating the opacity of cloud particles it is important to consider the material specific properties of the cloud which contribute to the wavelength dependency of the opacity. Wavelengths of high absorption efficiency correspond to frequencies of the ‘bending’ and ‘stretching’ modes of the material composition We provide a brief overview of the cloud species used in this thesis and some of their specific optical properties.

Al_2O_3: is non-absorbing at optical wavelengths, absorption bands are found in the deep infrared (400 and 600 μm). TiO_2: is also non-absorbing at optical wavelengths and has absorption features at 20—40 μm. Fe: As a conducting material, is highly absorbing across the entire wavelength range considered here, with absorption efficiency increasing with wavelength. SiO: Is absorbing in the UV, non-absorbing at optical wavelengths and has absorption bands at $\sim$ 10 μm. SiO_2: Is similar to SiO, but with an additional absorption band at $\sim$ 20 μm. $MgSiO_3$: Is similar to SiO_2 with absorption bands at 10 μm and 20 μm. Mg_2SiO_4: Is very similar to $MgSiO_3$ but with a slightly reduced absorption efficiency. Figure 2.3 shows each material (n, k) constants graphically.

Other studies have also investigated other mineral materials for exoplanet atmospheres,

Table 2.1: References for the (n, k) optical constants of the 12 different solids.

Solid species	Source
TiO_2[s]	Ribarsky in Palik (1985)
Al_2O_3[s]	Zeidler et al. (2013)
$CaTiO_3$[s]	Posch et al. (2003)
Fe_2O_3[s]	Unpublished
FeS[s]	Henning et al. (1995)
FeO[s]	Henning et al. (1995)
Fe[s]	Posch et al. (2003)
SiO[s]	Philipp in Palik (1985)
SiO_2[s]	Posch et al. (2003)
MgO[s]	Palik (1985)
$MgSiO_3$[s]	Dorschner et al. (1995)
Mg_2SiO_4[s]	Jäger et al. (2003)

such as KCl, Na_2S, MnS, each with their own specific material dependent properties. Table 2.1 provides a list of other cloud formation species and references for their optical constants.

Most solid materials published experimental optical constants do not cover the wavelength range (λ = 0.3—400.0 μm) required for RHD/GCM radiative-transfer schemes. An extrapolation of the available data for each material to shorter and longer wavelengths is therefore required to be undertaken. For wavelengths shorter than published data, it is assumed that (n, k) remain constant. At longer wavelengths, for the non-conducting material considered in this study, we assume that n remains constant while k is reduced linearly from the last data point to the longer wavelengths. This can make the material effective optical constants for the infrared wavelength bins, λ = 20.0-400.0 μm uncertain depending on the volume fraction and available data of each species. Figure 2.3 shows the (n, k) values of the outlined above materials graphically. Solid and dotted lines show the values of the interpolation scheme undertaken for lower/higher wavelengths, while the points show the raw experimental data.

Effective Medium Theory

Each mineral material present in the cloud particle will contribute their specific optical (n, k) constants, weighted by their local volume fraction V_s/V_{tot} (Eq. 2.25) of the material in each grain. Since Mie theory requires a single (n, k) as input to the code, effective optical constants for the material mixtures are calculated using effective medium theory. The numerical Bruggeman method (Bruggeman, 1935) is most often used, given by

$$\sum_s \left(\frac{\mathrm{V_s}}{\mathrm{V_{tot}}}\right) \frac{\epsilon_s - \epsilon_{\mathrm{av}}}{\epsilon_s + 2\epsilon_{\mathrm{av}}} = 0, \tag{2.60}$$

where $\mathrm{V_s}/\mathrm{V_{tot}}$ is the volume fraction of solid species s, ϵ_s the dielectric function of solid species s and ϵ_{av} the effective, average dielectric function over the total cloud particle volume. A Newton-Raphson minimisation scheme is then applied to solve for ϵ_{av}. In cases of rare non-convergence at the furthest infrared wavelengths ($\lambda = 20.0$—400.0 μm) where the (n, k) experimental values for materials are most uncertain, the analytic Landau-Lifshitz-Looyenga [LLL] method of Looyenga (1965) can be used, given by

$$\sqrt[3]{\epsilon_{\mathrm{av}}^2} = \sum_{\mathrm{s}} \left(\frac{\mathrm{V_s}}{\mathrm{V_{tot}}}\right) \sqrt[3]{\epsilon_s^2}. \tag{2.61}$$

Crystalline or Amorphous?

The grains found in the interstellar medium [ISM] are amorphous in nature due to the bombardment of neutrons and/or cosmic rays over long time periods, which breaks up the ordered crystalline structures. Since the dust grains from the ISM collapse into protoplanetary disks in star forming regions, amorphous grains have also been extensively invoked in protoplanetary disk studies.

Grains grown from chemical reactions from condensing materials are usually thought to be crystalline in nature due to the similarity of the chemical process to the growth of crystal material on Earth. Helling (2009) showed that nucleation experiments in Brown Dwarf cloud formation conditions are expected to be crystalline in nature. The initial ISM dust load is also thought to be crystalline from similar chemical processes in AGB star outflows. Additionally, since cloud particles are continually transported from lower to higher temperatures, either from dayside-nightside or height dependent temperature differences, an annealing process on the cloud surface is a likely possibility. This would give the crystal structure the surface energy and time to form from an initial amorphous state.

2.8.2 Cloud Opacity: Mie Theory

Cloud particles are a major source of opacity in the atmospheres of exoplanets. Scattering and extinction cross sections can be calculated using Mie theory for spherical particles (Mie, 1908). We follow the approach of Bohren & Huffman (1983), where the scattering and extinction cross sections are defined as

$$C_{\mathrm{sca}}(\lambda, a) = \frac{2\pi a^2}{x^2} \sum_{n=1}^{\infty} (2n+1)(|a_{\mathrm{n}}|^2 + |b_{\mathrm{n}}|^2), \tag{2.62}$$

$$C_{\mathrm{ext}}(\lambda, a) = \frac{2\pi a^2}{x^2} \sum_{n=1}^{\infty} (2n+1) Re(a_{\mathrm{n}} + b_{\mathrm{n}}), \tag{2.63}$$

respectively; where $\mathrm{x} = 2\pi a/\lambda$ is the wavelength dependent size parameter. The scattering coefficients $\mathrm{a_n}$ and $\mathrm{b_n}$ are calculated from the material optical k constant (Bohren & Huffman, 1983). The wavelength-dependent absorption and scattering efficiency of a cloud particle is then

$$Q_{\mathrm{sca}}(\lambda, a) = \frac{C_{\mathrm{sca}}(\lambda, a)}{\pi a^2}, \tag{2.64}$$

$$Q_{\mathrm{abs}}(\lambda, a) = \frac{C_{\mathrm{ext}}(\lambda, a)}{\pi a^2} - Q_{\mathrm{sca}}, \tag{2.65}$$

respectively. The total absorption and scattering efficiency κ [$\mathrm{cm^2\ g^{-1}}$] can then be derived by multiplying the corresponding efficiencies with the area and occurrence rate of each cloud particle.

$$\kappa_{\mathrm{sca}}(\lambda, a) = Q_{\mathrm{sca}}(\lambda, a)\pi a^2 n_{\mathrm{d}}/\rho_{\mathrm{gas}}, \tag{2.66}$$

$$\kappa_{\mathrm{abs}}(\lambda, a) = Q_{\mathrm{abs}}(\lambda, a)\pi a^2 n_{\mathrm{d}}/\rho_{\mathrm{gas}}. \tag{2.67}$$

From Mie theory the single scattering albedo ω_0 and the scattering asymmetry parameter g of the cloud particles can be calculated (Chapter 5).

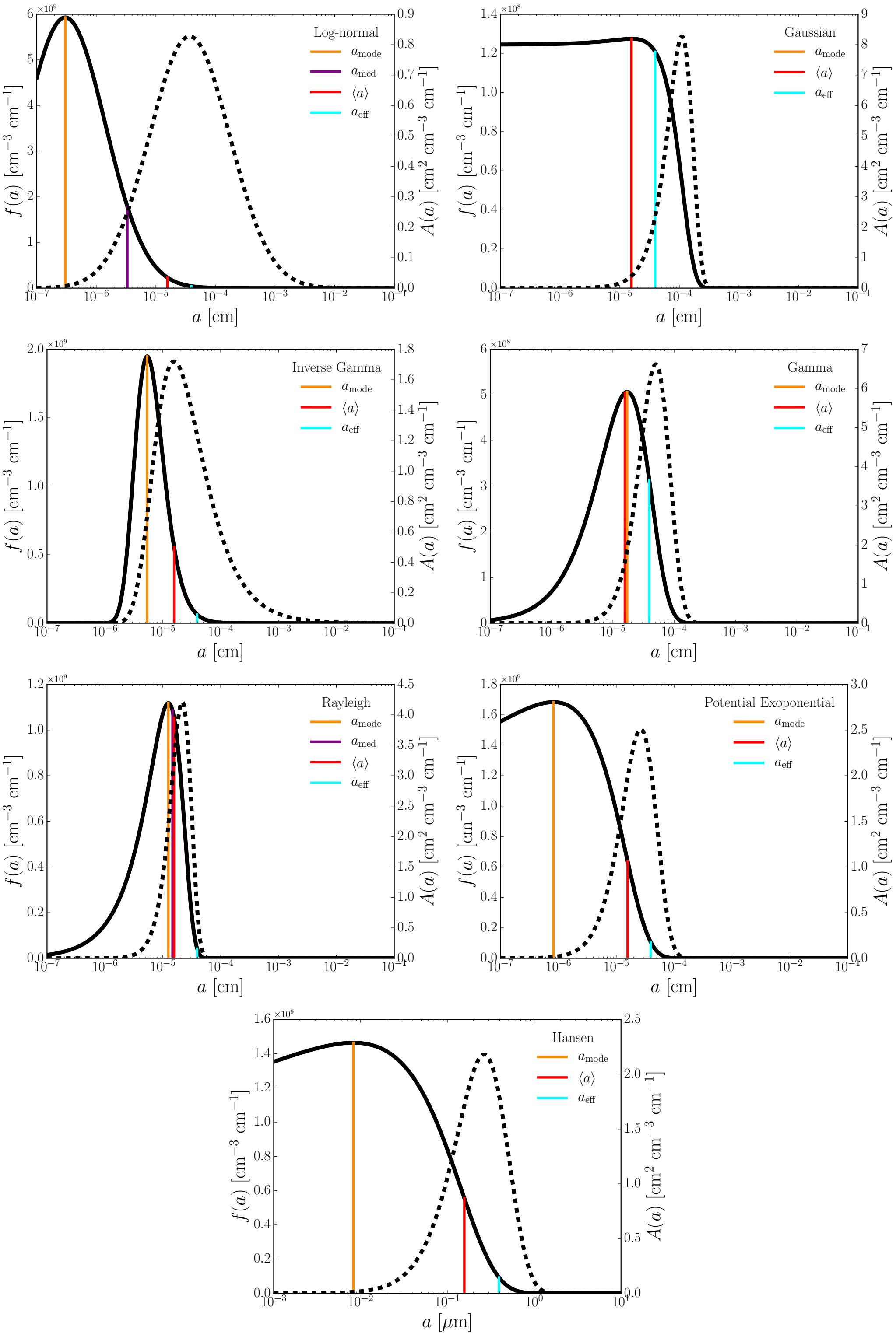

Figure 2.2: Reconstructed distributions from a nightside profile of the RHD simulations in Chapter 4. Top row: Log-normal and Gaussian distributions. Second row: Inverse Gamma and Gamma distributions. Third row: Rayleigh and Potential Exponential distributions. Bottom row: Hansen distribution. Solid lines represent the number density distribution f(a), while dashed lines represent the area distribution A(a). Various mean grain sizes derived from the simulation are also shown in the plots.

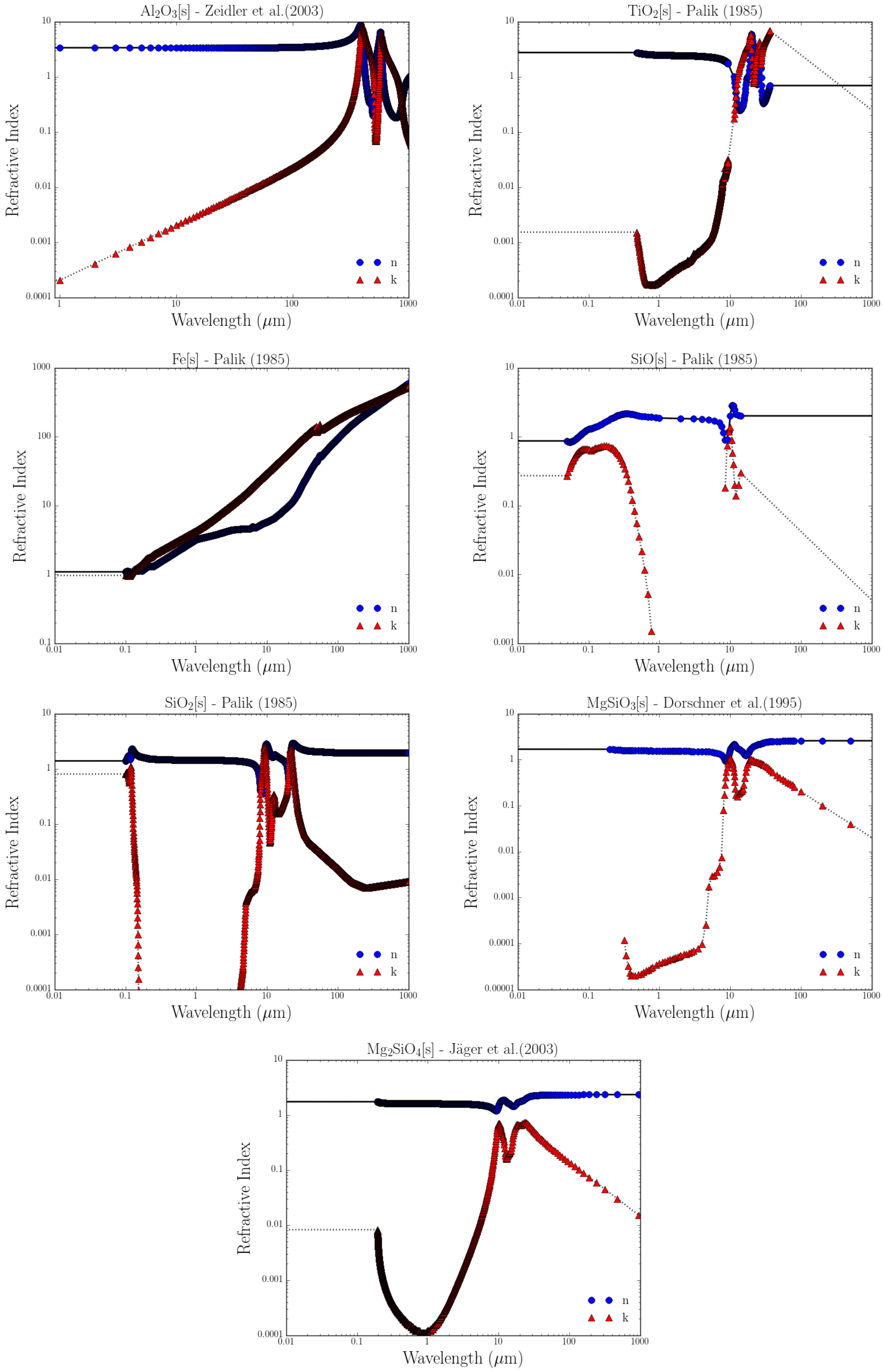

Figure 2.3: n (blue) and k (red) values from Table 2.1 for mineral materials used in this thesis. Top row: Al_2O_3[s] and TiO_2[s]. Second row: Fe[s] and SiO[s]. Third row: SiO_2 and $MgSiO_3$[s]. Bottom row: Mg_2SiO_4[s]. Triangles denote the values from the published tables, while solid lines represent the interpolation scheme used for missing data.

3

Static Cloud Formation Modelling

3.1 Introduction

In this chapter, we apply the 1D static cloud formation model DRIFT (Woitke & Helling, 2003, 2004; Helling & Woitke, 2006; Helling et al., 2008b) to output of the hot Jupiter HD 189733b RHD simulation presented in Dobbs-Dixon & Agol (2013). We investigate the chemical processes of cloud formation that occur in the simulation and assess the suitability of the atmosphere of HD 189733b to hosting mineral clouds in its atmosphere.

3.2 Timescales and Mixing

Vertical mixing is important to resupply the upper atmosphere with elements which have been depleted by cloud particle formation and their subsequent gravitational settling into deeper atmospheric layers (Woitke & Helling, 2003). Without mixing, the cloud particles in the atmosphere would rain out and remove heavy elements from the upper atmosphere. This leaves a metal poor gas phase where no future cloud particles could form (Woitke & Helling 2004;

Appendix A).

Previous Brown Dwarf approach

The main energy transport mechanism in the core of a Brown Dwarf is convection. The atmosphere is convectively unstable in the inner, hotter parts. This atmospheric convection causes substantial overshooting into even higher, and radiation dominated parts (e.g. Ludwig et al. (2002)). Woitke & Helling (2003, 2004) define the mixing timescale in low mass stellar atmospheres as the time for convective motions $v_{\rm conv}$ to travel a fraction of the pressure scale height, $\mathrm{H_p}(\vec{r})$

$$\tau_{\rm mix,conv}(\vec{r}) = \mathrm{const} \cdot \frac{H_{\rm p}(\vec{r})}{\mathrm{v_{conv}}(\vec{r})}, \tag{3.1}$$

and *const* an efficiency constant. Helling et al. (2008b); Witte et al. (2009, 2011) represent values for $\mathrm{v_{conv}}(\vec{r})$, in their 1D DRIFT-PHOENIX model atmospheres, above the convective zone (defined by the Schwarzschild criterion) from inertially driven *overshooting* of ascending gas bubbles.

Previous Hot Jupiter approach

On hot Jupiters, in contrast to Earth, Jupiter and Brown Dwarf atmospheres, the intensity of stellar irradiation can suppress convective motions down to very large pressures (Barman et al., 2001). Therefore turbulent diffusion is likely the dominant vertical transport mechanism. The use of the 3D RHD model results allows us to apply the local vertical velocity component, $\mathrm{v_z}(\vec{r})$, in our cloud formation model. No additional assumptions are required. Hence, $\mathrm{v_z}(\vec{r})$ is known for each atmospheric trajectory chosen, as visualised in Fig. 3.4.

Some chemical models of hot Jupiters (e.g. Moses et al. (2011)) use an approximation of the vertical diffusion coefficient $\mathrm{K_{zz}}(\vec{r})$ [$\mathrm{cm^2\ s^{-1}}$] of the gaseous state.

$$K_{\rm zz}(\vec{r}) = H_{\rm p}(\vec{r}) \cdot \mathrm{v_z}(\vec{r}). \tag{3.2}$$

The diffusion timescale is then

$$\tau_{\rm mix,diff}(\vec{r}) = \mathrm{const} \cdot \frac{H_{\rm p}^2(\vec{r})}{K_{\rm zz}(\vec{r})}. \tag{3.3}$$

Moses et al. (2011) apply the root-mean-square (rms) vertical velocities derived from global horizontal averages at each atmospheric layer to their chemical models. This results in a horizontally homogenous $K_{zz}(\vec{r})$ mixing parameter. Parmentier et al. (2013) derive a global mean value for $K_{zz}(\vec{r})$ as a function of local pressure using a passive tracer in their global circulation model [GCM] of HD 189733b resulting in $K_{zz}(\vec{r}) = 10^7\ p^{-0.65}$ (p [bar]). Using a global mean smooths away all horizontally dependent vertical velocity variations. Any parameterisation of the vertical mixing will depend on the details of the underlying hydrodynamical structure. Parmentier et al. (2013) use a 3D primitive equation model where vertical hydrostatic equilibrium is assumed. The radiation hydrodynamic simulations performed by Dobbs-Dixon & Agol (2013), applied in this chapter solve the full Navier-Stokes equations and will produce larger vertical velocities compared to the primitive equations (e.g. see Mayne et al. (2014)). In summary, vertical velocity may be substantially damped in models using the primitive equations. Both Eq. (3.2) and Parmentier et al. (2013) definitions for $K_{zz}(\vec{r})$ assume that the dominant mixing occurs in the vertical direction, possible mixing from horizontal flows are neglected. The time-scale comparison in Sect. 3.2 supports this assumption for cloud formation processes. It is worthwhile noting that the idea of diffusive mixing originates from shallow water approximations as applied in solar system research where a 2D velocity field produces shear which creates a turbulent velocity component. Hartogh et al. (2005) outline how local wind shear and the hydrostatic gas pressure are used to represent a vertical mixing.

Some arguments reinforce why vertical mixing is important:

- Regions with low vertical velocity can be replenished of elements by the horizontal winds from high vertical velocity regions in a 3D situation.
- Large vertical circulation patterns may be present, where vertical transport can be significant and element replenishment to the upper atmosphere may be more efficient.
- Vertical transport is a key mixing process on Earth which has been successfully applied to hot Jupiter chemical models (Moses et al., 2011; Venot et al., 2012; Agúndez et al., 2014).

We use Eq. (3.3) (const = 1) as the 1D mixing timescale input for our kinetic dust formation model, with Eq. (3.2) as the definition of the diffusion coefficient. We adopt the local vertical velocities that result from the Dobbs-Dixon & Agol (2013) 3D RHD atmosphere simulations

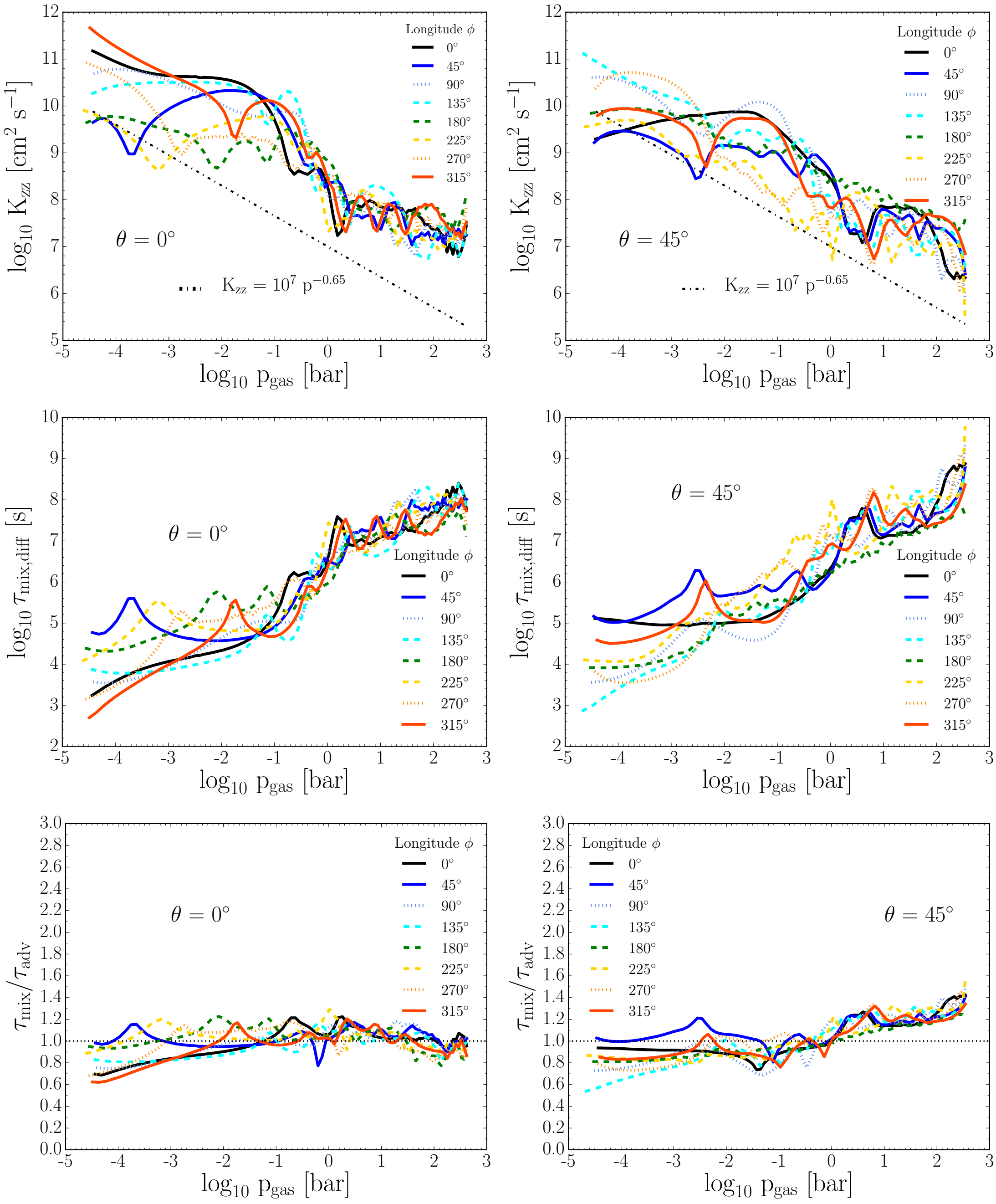

Figure 3.1: Top Row: Vertical diffusion coefficient $K_{zz}(\vec{r}) = H_p \cdot v_z(\vec{r})$ [cm^2 s^{-1}] applying the smoothed vertical velocities of the radiative-hydrodynamic HD 189733b model at latitudes $\theta = 0°$ and $\theta = 45°$, as a function of pressure at $\Delta\phi = +45°$ longitude intervals. The $K_{zz}(\vec{r}) = 10^7 p^{-0.65}$ (p [bar]) expression from Parmentier et al. (2013) is shown as dash-dotted lines. **Middle Row:** The vertical mixing timescales $\tau_{\rm mix,diff}$ [s] derived from the HD 189733b radiative-hydrodynamic model results at latitudes $\theta = 0°$, $\theta = 45°$, as a function of pressure at $\Delta\phi = +45°$ longitude intervals. **Bottom Row:** Ratio of the mixing and advective timescales at $\theta = 0°$, 45° respectively. The ratio of the timescales stays approximately equal at all pressures. Solid, dotted and dashed lines indicate dayside, day-night terminator and nightside profiles respectively.

for HD 189733b as the values for $v_z(\vec{r})$ (Fig. 3.4). A 3-point boxcar smoothing was applied to these velocities in order to smooth out negative vertical velocity bumps. The longitude dependent K_{zz} (ϕ, r) for latitudes $\theta = 0°, 45°$ is shown in Fig. 3.1 (first row) and the resulting vertical mixing timescales (second row). We include the K_{zz} relation from Parmentier et al. (2013) in Fig. 3.1 (dash-dotted line) for comparison. Their linear fit is approximately one order of magnitude lower which is similar to the difference found in HD 189733b and HD 209458b chemical models (Agúndez et al., 2014) who compared the two $K_{zz}(\vec{r})$ expressions for Showman et al. (2009) GCM simulations. The current approach aims to capture the unique vertical mixing and thermodynamic conditions at each trajectory, while also accounting for practical modelling of atmospheric mixing.

Advective timescales

An important timescale to consider is the characteristic advective timescale which is a representative timescale for heat to redistribute over the circumference of the globe. The advective timescale is given by

$$\tau_{\rm adv}(\vec{r}) = \frac{\pi r}{v_{\rm horiz}(\vec{r})}, \tag{3.4}$$

where $r(z)$ is the radius of the planet and $v_{\rm horiz}(\vec{r})$ the local gas velocity in the horizontal direction (ϕ). This timescale gives an idea of how fast thermodynamic conditions can change in the longitudinal direction at a particular height z in the atmosphere. Figure. 3.1 compares the advective timescale to the vertical diffusion timescale (Eq. (3.3)) and find that both time scales are of the same order of magnitude. This suggests that the convective/turbulent diffusion of upward gaseous material as described in Sect. 3.2 occurs approximately at the same timescales as gas advected across the globe. This suggests that, to a first approximation, the 1D ($T_{\rm gas}$, $p_{\rm gas}$) trajectories used as input for the cloud formation model do not fluctuate rapidly enough to substantially influence the cloud properties.

Cloud formation timescales

We compare the cloud particle settling, growth and nucleation timescales that result from our cloud model (Sect. 3.4) to the mixing and advection timescales that are derived from the

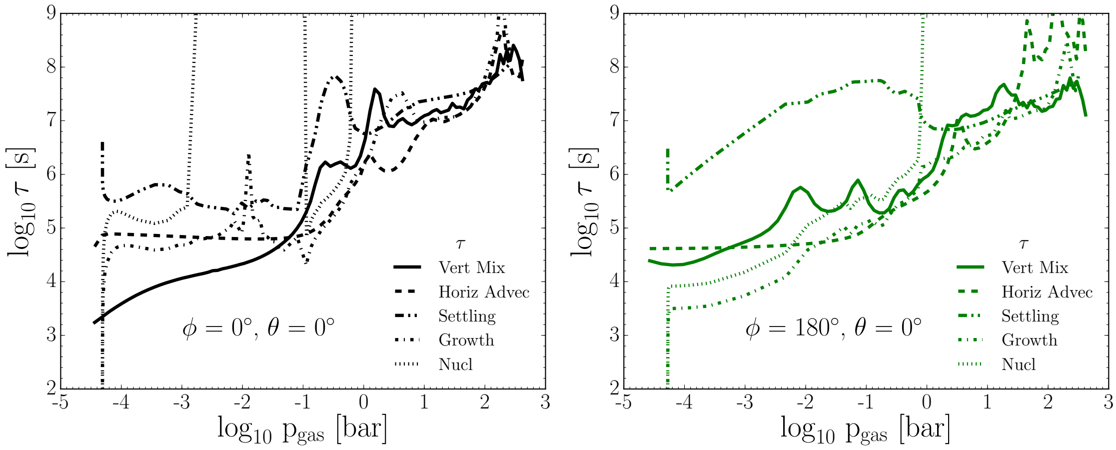

Figure 3.2: The vertical mixing, horizontal advection, cloud settling, cloud growth and cloud nucleation timescales at the sub-stellar point (Left) and $\phi = 180°$, $\theta = 0°$ (Right).

hydrodynamic fluid field. The nucleation timescale $\tau_{\rm nuc}$ is defined as

$$\tau_{\rm nuc} = \frac{n_{\rm d}}{J_\star}, \tag{3.5}$$

the growth timescale $\tau_{\rm gr}$ by

$$\tau_{\rm gr} = \frac{\sqrt[3]{36\pi}\langle a\rangle}{3|\chi^{\rm net}|}, \tag{3.6}$$

and the cloud particle settling timescale $\tau_{\rm setl}$ by

$$\tau_{\rm setl} = \frac{H_{\rm p}}{|\langle {\rm v}_{\rm dr}\rangle|}, \tag{3.7}$$

where $\langle {\rm v}_{\rm dr}\rangle$ is the large Knudsen number frictional regime (Kn >> 1) mean drift velocity (Woitke & Helling, 2003, Eq. 63). Figure 3.2 shows the timescales at the sub-stellar and anti-stellar points. Our results agree with earlier timescale analysis in Woitke & Helling (2003) who point out an hierarchical dominance of the cloud formation processes through the atmosphere. In the upper atmosphere nucleation is the most efficient process:

$$\tau_{\rm nuc} \lesssim \tau_{\rm gr} << \tau_{\rm mix} \sim \tau_{\rm adv} << \tau_{\rm setl}.$$

Deeper in the atmosphere nucleation eventually becomes inefficient and all timescales become comparable

$$\tau_{\rm gr} \lesssim \tau_{\rm mix} \sim \tau_{\rm adv} \lesssim \tau_{\rm setl}.$$

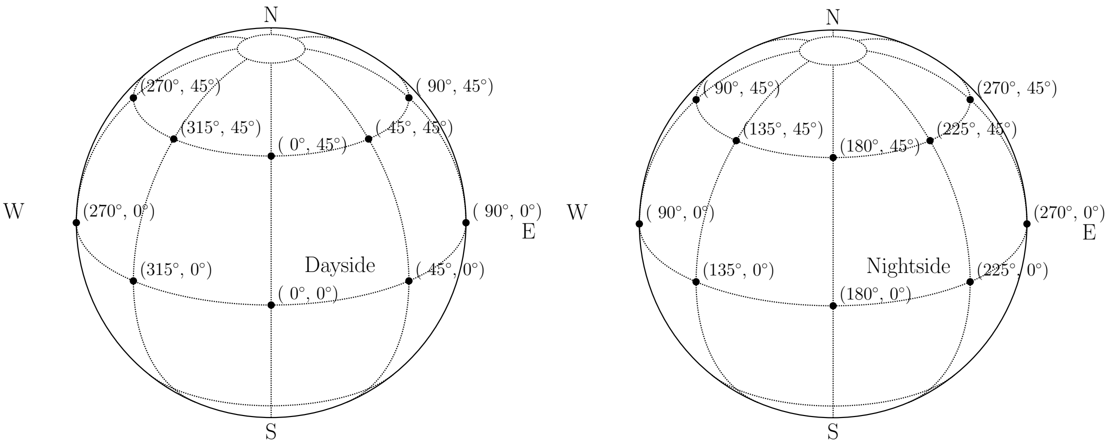

Figure 3.3: Illustration of the sample trajectories (black points) taken from the 3D radiative-hydrodynamic model atmosphere of HD 189733b (Dobbs-Dixon & Agol, 2013); longitudes $\phi = 0°$ $\ldots 315°$ in steps of $\Delta\phi = +45°$, latitudes $\theta = 0°, +45°$. The sub-stellar point is at $\phi = 0°$, $\theta = 0°$. We assume that the sample trajectories are latitudinal (north-south) symmetric.

The chemical processes that determine the cloud particle formation occur on shorter timescales than the large scale hydrodynamical timescales. This emphasises that the cloud particle formation is a local process.

3.3 2-model approach

We apply our kinetic dust cloud formation model to results from 3D radiation-hydrodynamic [3D RHD] simulations of HD 189733b's atmosphere (Dobbs-Dixon & Agol, 2013) and present a first study of spatially varying cloud formation on a hot Jupiter. We briefly summarise the main features of the kinetic cloud formation model (see: Woitke & Helling (2003, 2004); Helling et al. (2008b); Helling & Fomins (2013)). This cloud model has been successfully combined with 1D atmosphere models (DRIFT-PHOENIX; Dehn et al. (2007); Helling et al. (2008a); Witte et al. (2009, 2011)) to produce synthetic spectra of M Dwarfs, Brown Dwarfs and *non-irradiated* hot Jupiter exoplanets. We then summarise the multi-dimensional radiative-hydrodynamical model from Dobbs-Dixon & Agol (2013) used as input for the kinetic cloud formation model. Finally, we outline our approach in calculating the absorption and scattering properties of multi-material, multi-disperse, mixed cloud particles.

3.3.1 Cloud formation modelling

Cloud formation proceeds via a sequence of processes that are described kinetically in our cloud formation model:

Table 3.1: Input quantities for the cloud formation model. Local T_{gas}, p_{gas}, ρ_{gas}, v_z and z are taken from the 3D radiation-hydrodynamic model.

Input	Definition	Units
T_{gas} $(\vec{r})$	local gas temperature	K
p_{gas} $(\vec{r})$	local gas pressure	dyn cm^{-2}
ρ_{gas} $(\vec{r})$	local gas density	g cm^{-3}
v_z $(\vec{r})$	local vertical gas velocity	cm s^{-1}
z	vertical atmospheric height	cm
$\epsilon_x^0/\epsilon_{H(\vec{r})}$	element abundance	-
g $(\vec{r})$	surface gravity	cm s^{-2}

1. Formation of seed particles by homomolecular homogeneous nucleation (Jeong et al., 2003; Lee et al., 2015b).

2. Growth of various solid materials by gas-grain chemical surface reactions on the existing seeds or grains (Gail & Sedlmayr, 1986; Helling & Woitke, 2006; Helling et al., 2008b).

3. Evaporation of grains when the materials that they are composed of become thermally unstable (Helling & Woitke, 2006; Helling et al., 2008b).

4. Gravitational settling allowing a continuation of grain growth through transport of grains out of under-saturated regions (Woitke & Helling, 2003, 2004).

5. Element depletion in regions of cloud formation which can stop new grains from forming (Helling & Woitke, 2006).

6. Convective/turbulent mixing from deeper to higher atmospheric regions to provide element replenishment (Woitke & Helling, 2003, 2004).

3.3.2 3D radiative-hydrodynamical model

The 3D radiative-hydrodynamical [3D RHD] model solves the fully compressible Navier-Stokes equations coupled to a wavelength dependent two-stream radiative transfer scheme. The model assumes a tidally-locked planet with $\phi = 0°$, $\theta = 0°$ denoting the sub-stellar point (the closest point to the host star). There are three components to the wavelength dependent opacities: molecular opacities consistent with solar composition gas, a gray component representing a strongly absorbing cloud deck, and a strong Rayleigh scattering component. Equations are solved on a spherical grid with pressures ranging from $\sim 10^{-4.5}$ to $\sim 10^3$ bar. Input parameters were chosen to represent the bulk observed properties of HD 189733b, but (with the exception of the opacity) were not tuned to match spectroscopic observations. The

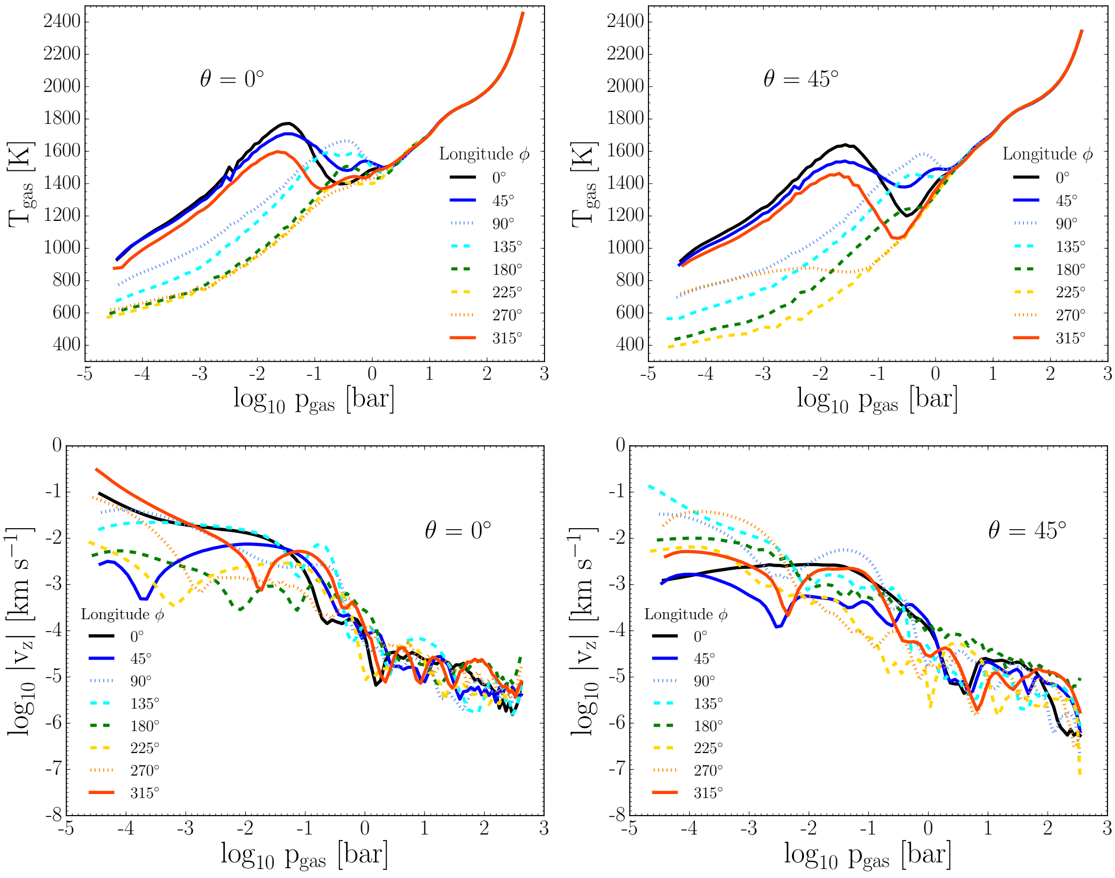

Figure 3.4: 1D trajectory results from the 3D RHD HD 189733b atmosphere simulation used as input for the cloud formation model. **Top Row:** (T_{gas}, p_{gas}) profiles in steps of longitude $\Delta\phi = +45°$ at equatorial, $\theta = 0°$ and latitude, $\theta = 45°$ profiles. **Bottom Row:** Smoothed vertical gas velocities $\vec{v}_z$ [km s^{-1}] in steps of longitude $\Delta\phi = +45°$ at equatorial, $\theta = 0°$ and latitude, $\theta = 45°$ profiles. Both latitudes show a temperature inversion on the dayside. The sub-stellar point is at $\phi = 0°$, $\theta = 0°$. Solid, dotted and dashed lines indicate dayside, day-night terminator and nightside profiles respectively.

dominant dynamical feature is the formation of a super-rotating, circumplanetary jet (Tsai et al., 2014) that efficiently advects energy from day to night near the equatorial regions. Rossby waves are global planetary waves which are a result of the latitudinal displacement of constant potential vorticity surfaces. This results in a westward directional jet at higher latitudes. The equatorial eastward jet forms from the coupling of these Rossby wave with eddies which pumps positive angular momentum toward the equator (Showman & Polvani, 2011). Significant vertical mixing, discussed later, is seen throughout the atmosphere. Calculated transit spectra, emission spectra, and light curves agree quite well with current observations from 0.3μm to 8.0μm. Further details can be found in Dobbs-Dixon & Agol (2013).

3.3.3 Model set-up and input quantities

We sampled vertical trajectories of the 3D RHD model at longitudes of $\phi = 0^\circ \ldots 315^\circ$ in steps of $\Delta\phi = +45^\circ$ and latitudes of $\theta = 0^\circ$, $+45^\circ$ (Fig. 3.3). The horizontal wind velocity moves in the positive ϕ direction. Figure 3.4 shows the ($T_{\rm gas}$, $p_{\rm gas}$) and vertical velocity profiles used to derive the cloud structure at the equator $\theta = 0^\circ$ and latitude $\theta = 45^\circ$. Local temperature inversions are present in the dayside ($T_{\rm gas}$, $p_{\rm gas}$) profiles which are exposed to the irradiation of the host star without the need for an additional opacity source. The local temperature maximum migrates eastward with increasing atmospheric depth. This is due to hydrodynamical flows funnelling gas towards the equator causing viscous, compressive and shock heating. The ($T_{\rm gas}$, $p_{\rm gas}$) profile at latitude $\theta = 45^\circ$ has steeper temperature inversions on the dayside. Sample trajectories converge to equal temperatures at $p_{\rm gas} > 1$ bar for all longitudes and latitudes. We apply a 3-point boxcar smoothing to the vertical velocity profiles in order to reduce the effects of unresolved turbulence. Further required input quantities are a constant surface gravity of $\log g = 3.32$ and initial solar element abundances $\epsilon^0_{\rm x}/\epsilon_{\rm H}$ (element ‘x’ to Hydrogen ratio) with C/O = 0.427 (Anders & Grevesse, 1989) for all atmospheric layers. However, we note the element abundance of the gas phase will increase or decrease due to cloud formation or evaporation (Fig. 3.8). We assume local thermal equilibrium (LTE) for all gas-gas and dust-gas chemical reactions. The required input quantities for the kinetic cloud formation model are summarised in Table 3.1.

3.4 Modelling Cloud Formation in HD 189733b

We apply the dust formation theory developed by Woitke & Helling (2003, 2004); Helling & Woitke (2006) and Helling et al. (2008b) in its 1D stationary form to 1D output trajectories of a 3D HD 189733b radiation-hydrodynamical [3D RHD] model, as described in Dobbs-Dixon & Agol (2013). In the following, we present local and global cloud structures for HD 189733b and discuss detailed results on cloud properties such as grain sizes, material composition, element abundances, dust-to-gas ratio and C/O ratio. We investigate general trends of the cloud structure as it varies throughout the atmosphere and make first attempts to study the cloud properties across the planetary globe.

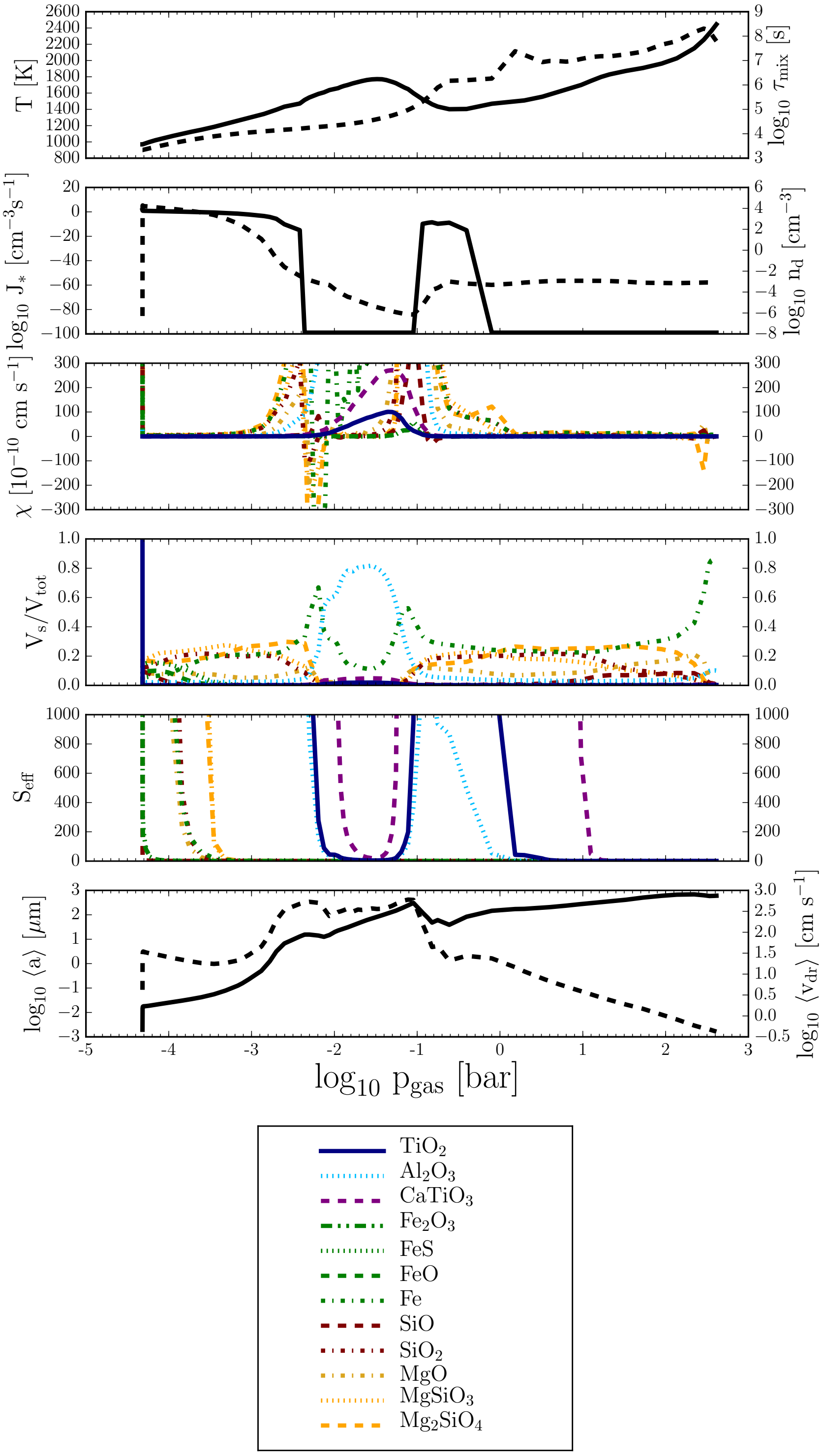

Figure 3.5: HD 189733b's calculated cloud structure at the sub-stellar point ($\theta = 0°$, $\phi = 0°$). **Upper**: *1st panel*: Local gas temperature T_{gas} [K] (solid, left) and mixing timescale τ_{mix} [s] (dashed, right). *2nd panel*: Nucleation rate J_* [cm^{-3}s^{-1}] (solid, left) and dust number density n_d [cm^{-3}] (dashed, right). *3rd panel*: Growth velocity of material s χ [cm s^{-1}]. *4th panel*: Volume fraction V_s/V_{tot} of solid s. *5th panel*: Effective supersaturation ratio S_{eff} of individual solids. *6th panel*: Cloud particle mean radius ⟨a⟩ [μm] (solid, left) and mean drift velocity ⟨v_{dr}⟩ [cm s^{-1}] (dashed, right). **Lower**: Key showing line-style and colour of our considered dust species.

3.4.1 The cloud structure of HD 189733b at the sub-stellar point

The substellar point ($\phi = 0°$, $\theta = 0°$) is the most directly irradiated point in atmospheres of hot Jupiters such as HD 189733b which is measured by observing before, during and after secondary transit (occulatation). We use this well defined location to provide a detailed description of the vertical cloud structure. We compare this atmospheric trajectory to other longitudes in Sec. 3.4.2 and to other latitudes in Sec. 3.4.3. Figure 3.5 shows that the cloud structure starts with the formation of seed particles (J_* [cm^{-3} s^{-1}] - nucleation rate) occurring at the upper pressure boundary of $\sim10^{-4}$ bar. After the first surface growth processes occur on the seed particles, the cloud particles then gravitationally settle into the atmospheric regions below (toward higher density/pressure). Primary nucleation is efficient down to $\sim10^{-2.5}$ bar where it drops off significantly, indicating that the local temperature is too high for further nucleation and that the seed forming species has been substantially depleted. The gas-grain surface chemical reactions that form the grain mantle (Eq. (2.16)) increase in rate as the cloud particles fall inward due the force gravity acting on their bulk. This is due to the cloud particles encountering increasing local gas density, and therefore more condensible material is available to react with cloud particles. This surface growth becomes more efficient from $\sim10^{-3}\ldots\sim10^{-2}$ bar until the local temperature is so hot that the materials become thermally unstable and evaporate. The evaporation region results in a half magnitude decrease of the cloud particle sizes (negative χ) in the center region of the cloud. The relative volume fractions of the solid 's', V_s/V_{tot}, represents the material composition of the cloud particles. The cloud particle composition is dominated by silicates and oxides such as $MgSiO_3$[s]($\sim$27%), Mg_2SiO_4[s]($\sim$20%), SiO_2[s]($\sim$21%) at the upper regions $\lesssim10^{-2.5}$ bar. Fe[s] contributes $\lesssim$20% to the volume of the cloud particle in this region. The other 8 growth species (TiO_2[s]($\sim$0.03%), Al_2O_3[s]($\sim$2%), $CaTiO_3$[s]($\sim$0.15%), Fe_2O_3[s]($\sim$0.001%), FeS[s]($\sim$1.6%), FeO[s]($\sim$0.35%), SiO[s]($\sim$0.05%), MgO[s]($\sim$7%)) constitute the remaining grain volume. An evaporation region at $\sim10^{-2.5}$ bar before the temperature maximum at $\sim10^{-1.5}$ bar alters the grain composition dramatically. Al_2O_3[s] and Fe[s] dominate the grain composition in this region as the less stable silicates and oxides have evaporated from the grain surface. At the temperature maximum the grain is composed of Al_2O_3[s]($\sim$80%) and Fe[s]($\sim$15%). This suggests the presence of a cloud section more transparent than surrounding layers. Deeper in the atmosphere, a temperature inversion occurs (Fig. 3.4) starting from $\sim10^{-1.5}$ bar. The temperature drops by $\sim$400 K from

$\sim10^{-1.5}\ldots\sim10^{-0.5}$ bar. This temperature decrease allows a secondary nucleation region from $\sim10^{-1}\ldots1$ bar. The number density of grains jumps by ∼2 orders of magnitude at the secondary nucleation region, as a result of formation of many new cloud particles. This causes a dip in the mean grain size at $\sim10^{-1}$ bar. Such secondary nucleation has not been seen in our cloud model results in Brown Dwarf nor non-irradiated giant gas planet atmospheres. Silicates and oxides are now thermally stable and once again form the grain mantle. The grain composition is approximately a 70-20-10 % mix of silicates and oxides, iron and other material respectively in this region, similar to the composition before the temperature maximum. At the cloud base, Fe[s] dominates the composition (∼35%) with MgO[s] and Mg_2SiO_4[s] making up ∼16% and ∼23% respectively. Table. 3.2 shows the percentage volume fraction V_s/V_{tot} of the 12 dust species at the sub-stellar point and the $\phi = 180°$, $\theta = 0°$ trajectory at 10^{-4}, 10^{-3}, 10^{-2}, 10^{-1}, 1 and 10 bar.

Our results show that the entire vertical atmospheric range considered here ($\sim10^{-4.5}\ldots10^{3}$ bar) is filled with dust. The exact properties of this dust such as size, composition and number density change depending on the local thermodynamical state. The 3D RHD model does not expand to such low pressures and densities that the cloud formation processes becomes inefficient (Chapter. 3). This suggests that clouds can be present at a higher and lower pressure than the present 3D RHD model boundary conditions allow.

3.4.2 Cloud structure changes with longitude (East-West)

One of the main features of the radiation-hydrodynamic simulation is the equatorial jet structure which transports heat over the entire 360° longitude. The presence of this jet changes the thermodynamic structure of the atmosphere which affects the resulting global cloud structure. We sampled the 3D RHD results in longitude steps of $\Delta\phi = +45°$ at the equatorial region $\theta = 0°$ to investigate if cloud properties change significantly from dayside to nightside. Figure 3.4 shows that the nightside (T_{gas}, p_{gas}) profiles can be ∼200 K cooler than the dayside in the upper atmospheric regions ($\sim10^{-4.5}\ldots10^{-1}$ bar). Figure 3.6 shows the nucleation rate J_* [$cm^{-3}\ s^{-1}$] for dayside (solid lines), day-night terminator (dotted lines) and nightside (dashed lines) sample trajectories. The dayside nucleation rates fall off quicker with atmospheric depth compared to the terminator and nightside profiles, particularly relevant for interpreting transit spectra. At longitude $\phi = 315°$ a secondary nucleation region emerges, similar to the sub-stellar point structure (Fig. 3.5). The terminator and nightside nucleation regions extend further into the

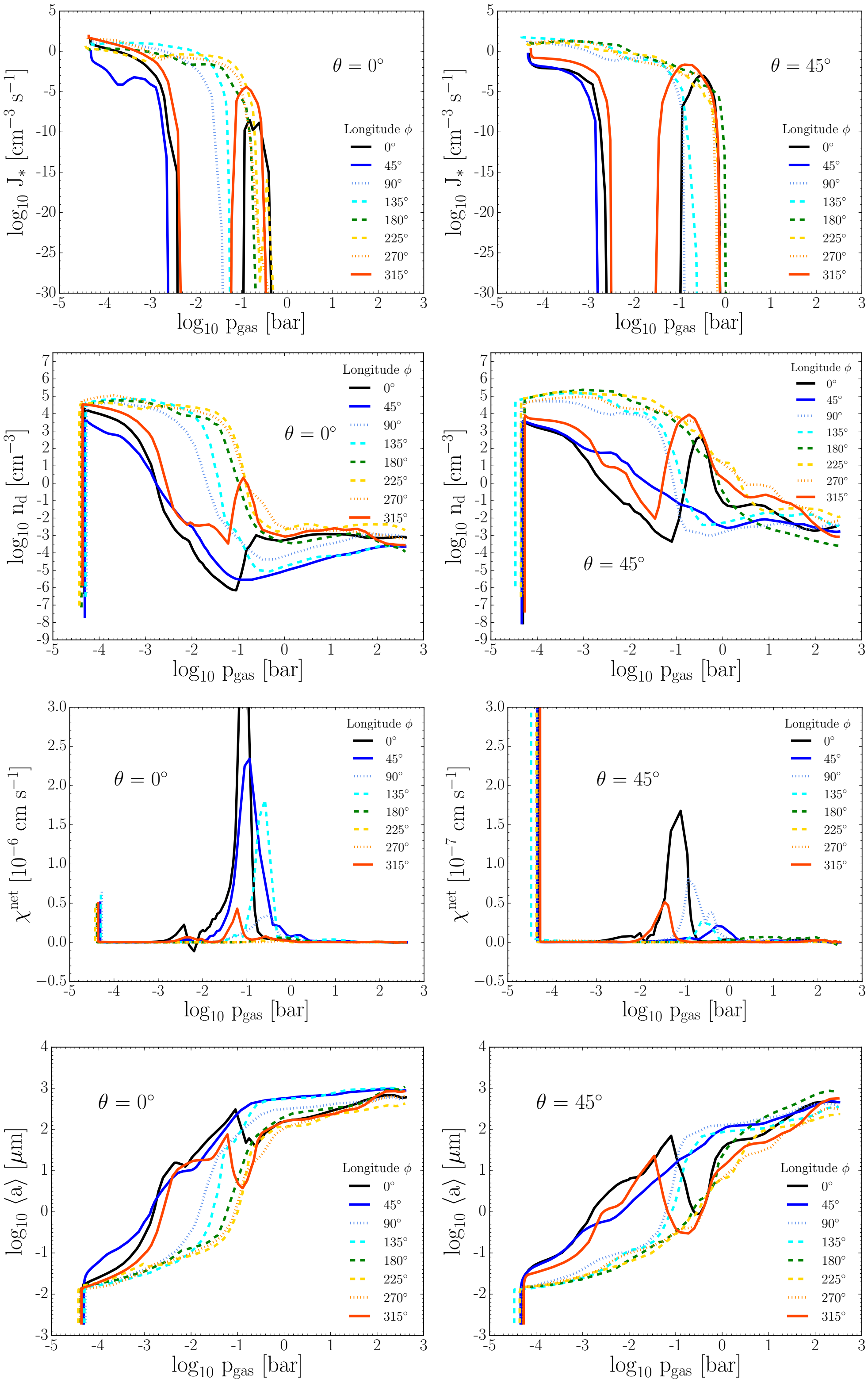

Figure 3.6: Dust properties as a function of gas pressure for $\Delta\phi = +45°$ longitude intervals for latitudes $\theta = 0°$ (Left column) and 45° (Right column): **Top Row:** Nucleation rate J$_*$ [cm^{-3} s^{-1}]. **Second Row:** Dust number density n$_d$ [cm^{-3}]. **Third Row:** Net dust growth velocity χ^{net} [cm s^{-1}]. **Bottom Row:** Mean grain size ⟨a⟩ [μm]. Solid, dotted and dashed lines indicate dayside, day-night terminator and nightside profiles respectively.

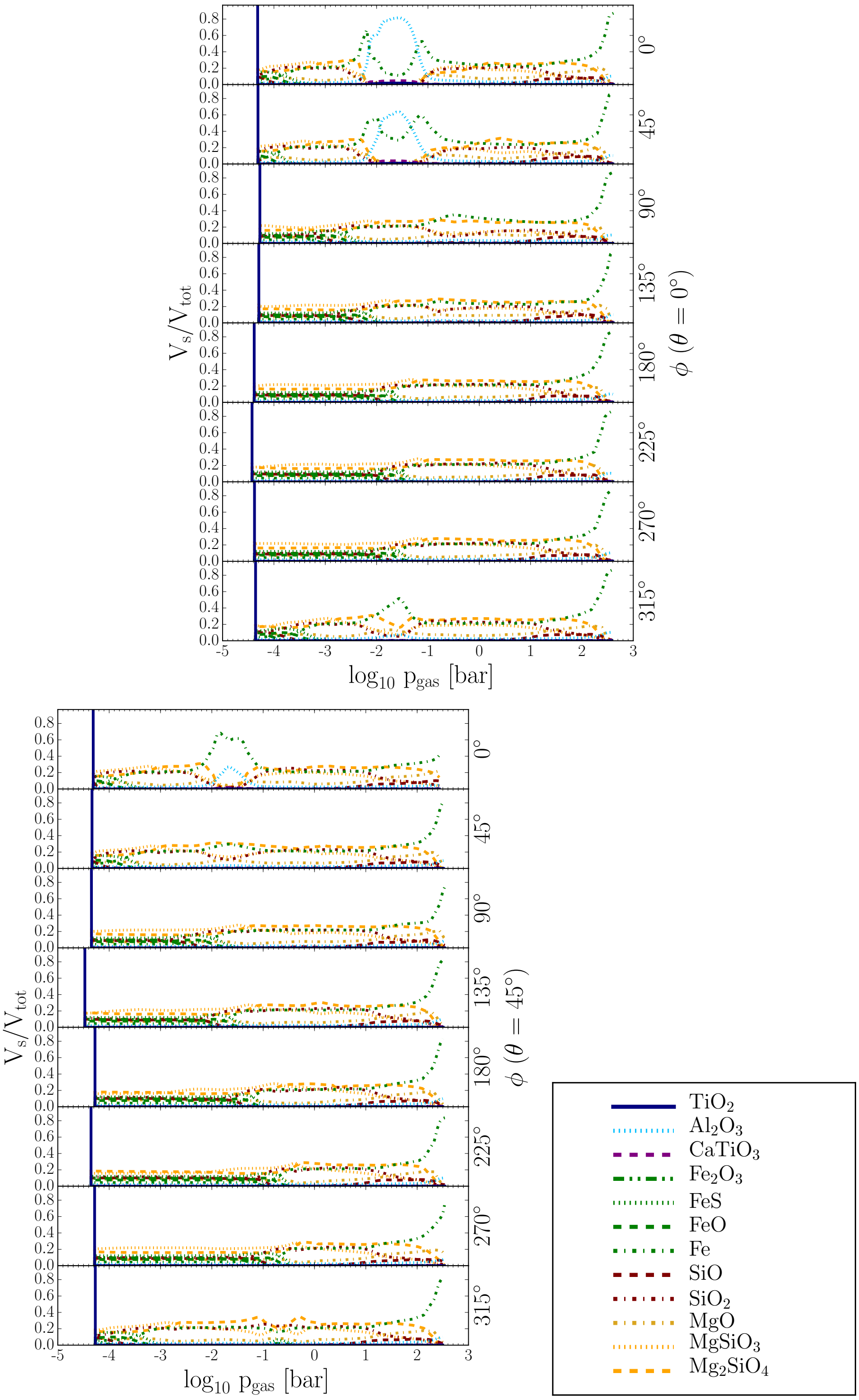

Figure 3.7: Top: Dust composition volume fraction V_s/V_{tot} as a function of pressure at $\theta = 0°$ (Left) and $\theta = 45°$ (Right) in $\Delta\phi = +45°$ longitude intervals. Grain composition is generally dominated by silicate-oxides including $MgSiO_3$[s] apart from localised regions such as $10^{-2}\ldots10^{-1}$ bar at $\phi = 0°, 45°$, $\theta = 0°$. Fe[s] dominates at $10^{-2}\ldots10^{-1}$ bar at $\phi = 0°$, $\theta = 45°$. Fe[s] grains remain at the cloud base as the most thermally stable element. **Bottom:** Key showing line-style and colour of our considered dust species.

Table 3.2: Volume fraction V_s/V_{tot}[%] for the 12 solid species included in kinetic the cloud model. The first row of each species corresponds to the sub-stellar trajectory ($\phi = 0°$, $\theta = 0°$) cloud structure. The second row corresponds to the nightside trajectory $\phi = 180°$, $\theta = 0°$ cloud structure. Note: The pressure at the cloud base is different for the two profiles.

Pressure [bar]	10^{-4}	10^{-3}	10^{-2}	10^{-1}	1	10	Cloud base
$\langle a \rangle$ [μm]	0.025	0.23	19.9	307	146	275	605
	0.018	0.035	0.15	12.3	174	338	1088
Solid species							
TiO_2[s]	0.03	0.03	1.22	0.26	0.05	0.02	0.22
	0.06	0.04	0.03	0.03	0.02	0.01	0.24
Al_2O_3[s]	2.11	2.43	60.98	13.99	3.68	2.84	10.03
	2.06	2.06	2.13	2.42	2.44	2.49	10.03
$CaTiO_3$[s]	0.13	0.16	3.56	0.87	0.24	0.22	0.64
	0.07	0.10	0.14	0.17	0.17	0.20	0.77
Fe_2O_3[s]	0.10	>0.01	>0.01	>0.01	>0.01	>0.01	>0.01
	9.69	9.68	0.07	>0.01	>0.01	>0.01	>0.01
FeS[s]	14.44	0.22	0.03	0.09	0.05	0.02	0.03
	12.12	12.12	14.45	0.10	0.05	0.02	0.03
FeO[s]	8.87	0.06	0.03	0.07	0.02	0.02	0.09
	7.63	7.63	7.93	0.03	0.02	0.02	0.09
Fe[s]	7.87	21.08	30.93	45.00	24.29	22.49	87.15
	4.52	4.52	8.50	21.14	21.29	21.75	86.80
SiO[s]	2.42	0.06	0.08	0.70	0.48	3.82	0.92
	8.84	9.03	1.12	0.11	0.44	5.20	0.99
SiO_2[s]	17.90	20.08	0.75	7.88	19.94	20.60	0.12
	9.92	10.13	19.35	21.26	22.18	20.33	0.13
MgO[s]	7.73	5.13	1.97	11.10	8.05	8.87	0.79
	7.21	7.28	7.61	5.40	6.51	9.35	0.89
$MgSiO_3$[s]	22.47	24.11	0.14	8.96	20.77	15.79	>0.01
	21.74	20.71	22.41	22.02	21.82	15.25	>0.01
Mg_2SiO_4[s]	15.93	26.64	0.30	11.09	21.41	25.31	0.02
	16.15	16.70	16.23	27.31	26.59	25.39	0.04

atmosphere to ~10^{-1} bar. As a consequence of the different nucleation rates between dayside and nightside, the number density of cloud particles n_d [cm^{-3}] is greater on the nightside down to pressures of ~10^{-1} bar. At this pressure, the secondary nucleation regions on the dayside, ϕ = 0°, 315° profiles spike up the number density comparable to values on the nightside. From Fig. 3.6 the net growth velocity χ^{net} [cm s^{-1}] shows that the most efficient growth regions for the grains is approximately $10^{-3}\ldots1$ bar for the dayside and $10^{-2}\ldots1$ bar for the nightside. Although the temperature of the local gas phase plays a role in increasing the growth rate, it is the increasing local density of material (as the particle falls thought the atmosphere) that is the dominating factor in determining growth rates (Eq. (2.16); Fig. 3.8). Consequently, the mean grain size $\langle a \rangle$ [μm] shows a stronger increase from ~$10^{-4}\ldots10^{-1}$ bar on the dayside than the nightside. The mean grain size dips at ~10^{-1} bar for longitudes $\phi = 0°$ and 315° due to the increase of grain number density as now the same number of gaseous growth species have to be distributed over a larger surface area. Figure 3.7 shows the volume fraction V_s/V_{tot} of the solid species 's'. The dust composition is generally dominated by silicates and oxides (~60 %) such as $MgSiO_3$[s], Mg_2SiO_4[s] and SiO_2[s] with (~20 %) Fe[s] and FeO[s] content. At the cloud base the grain is primarily composed of Fe[s] (~85%) and Al_2O_3[s] (~10%). The $\phi = 45°$, $\theta = 0°$ cloud structure contains an Al_2O_3[s] (~60 %) and Fe[s] (~30 %) dominant region from ~$10^{-2}\ldots10^{-1}$ bar similar to the sub-stellar point structure. Table 3.2 summarises the percentage volume fraction V_s/V_{tot} and the mean cloud particle size $\langle a \rangle$ of the 12 dust species at the sub-stellar point and the $\phi = 180°$, $\theta = 0°$ trajectory at 10^{-4}, 10^{-3}, 10^{-2}, 10^{-1}, 1 and 10 bar pressures.

3.4.3 Cloud structure changes with latitude (North-South)

At higher latitudes $\theta \gtrsim 40°$ the 3D RHD model produces a jet structure flowing in the opposite direction to the equatorial jet at dayside longitudes (Tsai et al., 2014). This significantly alters the (T_{gas}, p_{gas}) and vertical velocity profiles (Fig. 3.4). These latitudes also contain the coldest regions of the nightside where vortices form and dominate the atmosphere dynamics (Dobbs-Dixon & Agol, 2013, Fig. 1). To investigate the cloud structure at these latitudes we repeated our trajectory sampling for latitudes of $\theta = 45°$ in longitude steps of $\Delta\phi = +45°$. Figure 3.6 shows the nucleation rate J_* [cm^{-3} s^{-1}] for dayside (solid lines), day-night terminator (dotted lines) and nightside (dashed lines) sample trajectories. The profiles are similar to the equatorial $\theta = 0°$ regions with double nucleation peaks at $\phi = 0°$ and 315°. Again, there is an increase in number density n_d [cm^{-3}] (Fig. 3.6) from $10^{-1}\ldots1$ bar due to second nucleation regions at $\phi = 0°$ and 315°. The growth velocity χ^{net} is generally an order of magnitude lower on the dayside than the equatorial regions. This results in higher latitude clouds containing smaller grain sizes compared to their equatorial counterparts.

3.4.4 Element depletion, C/O ratio and dust-to-gas ratio

The cloud formation process strongly depletes the local gas phase of elements, primarily through extremely efficient solid surface growth processes. We consider the 8 elements that constitute the solid materials of the cloud particles, Mg, Si, Ti, O, Fe, Al, Ca and S assuming an initial solar element abundance (ϵ_x^0) for all layers. Figure 3.8 shows the elemental abundance ϵ_x (ratio to Hydrogen abundance) of each element as a function of pressure at each of the sample trajectories. Depletion occurs due to the formation of solids made of the these elements onto the cloud particle surface and by nucleation of new cloud particles. Increase in element abundances correspond to regions of solid material evaporation. Ti is depleted at the upper boundary due to immediate efficient nucleation. For dayside profiles $\phi = 0°$, 45°, 315°, $\theta = 0°$, 45°, from $10^{-4.5}\ldots10^{-3}$ bar, Mg, Ti, Si, Al and Fe are depleted by ~1 order of magnitude while O, S and Ca are depleted by ~ 10%. These profiles return to initial solar abundance values at $\sim10^{-2}$ bar where the solid material from the grain surface evaporates, returning elements to the gas phase. O, Fe, Si S and Mg abundance can slightly overshoot solar abundance values at their respective maximums. Elements are most heavily depleted in these profiles at $\sim10^{-1}$ bar where the most efficient surface growth occurs. Mg, Si, and Fe are depleted by ~3 orders of magnitude, Ti by 8 orders of magnitude and Al by 5 orders of magnitude. O, S and Ca are again depleted by ~ 10%. Fe, Al, S and Ti return to solar abundance or slightly sub-solar abundance at the cloud base, where all materials have evaporated. The cloud base is enriched in O, Ca, Mg and Si which are ~50% above solar abundance values. For nightside and day-night terminator profiles $\phi = 90°$, 135°, 180°, 225°, 270° $\theta = 0°$, 45°, from $10^{-4.5}\ldots10^{-2}$ bar, Mg, Ti, Si, Al and Fe are depleted by 4 to 8 orders of magnitude while O and S are depleted by ~1 order of magnitude and Ca by ~10%. The $\phi = 90°$ and 135°, $\theta = 0°$, 45° show a return to near initial abundance at $\sim10^{-0.5}$ bar from material evaporation. Other nightside/terminator profiles gradually return to initial abundance from ~1 bar to their respective cloud bases. Again, O, Ca, Mg and Si are slightly above solar abundance at the cloud base.

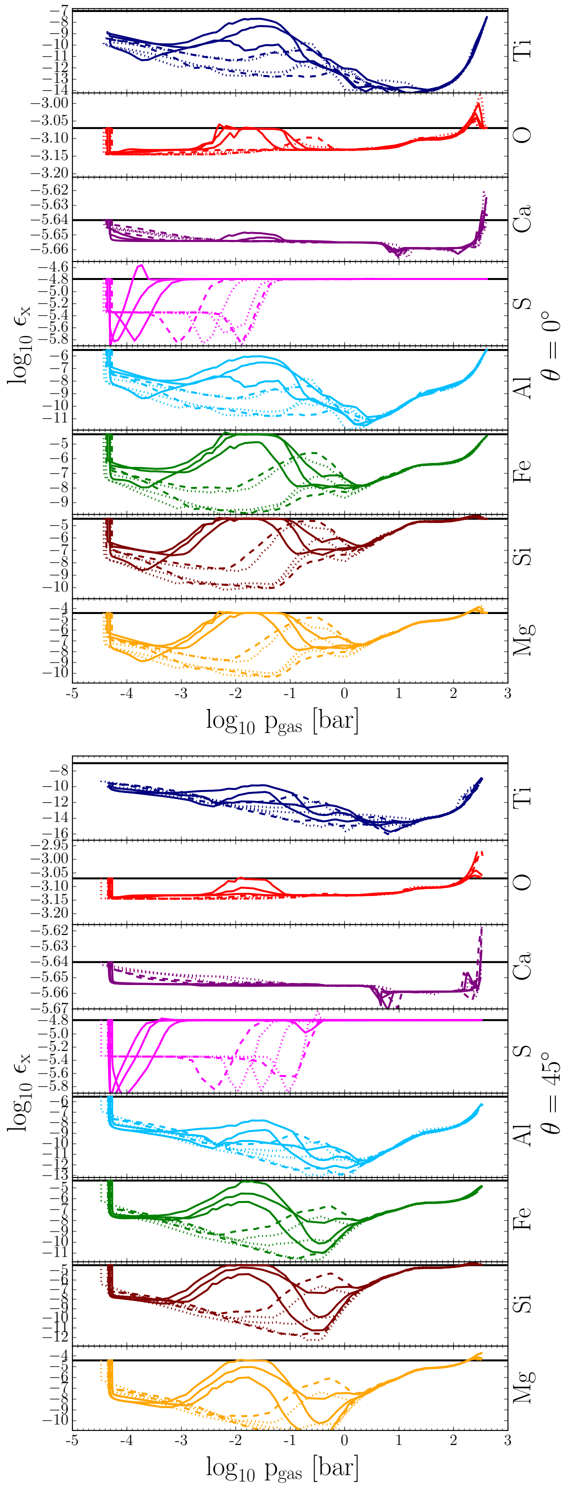

Figure 3.8: Gas phase element abundances ϵ_x as a function of pressure at $\theta = 0°$ (Left) and $\theta = 45°$ (Right) in $\Delta\phi = +45°$ longitude intervals. We consider 8 elements: Mg(orange), Si(maroon), Ti(blue), O(red), Fe(green), Al(cyan), Ca(purple), S(magenta) that constitute the growth species. Horizontal black lines indicate solar abundance ϵ_x^0. A decrease in element abundance indicates condensation of growth species onto cloud particle surface. An increase indicates evaporation of molecules constituted of that element from the cloud particle surface. Dayside profiles (solid) are $\phi = 0°, 45°, 315°$, $\theta = 0°, 45°$. Day-night terminator profiles (dashed) are $\phi = 90°, 270°$, $\theta = 0°, 45°$. Nightside profiles (dotted) are $\phi = 135°, 180°, 225°$, $\theta = 0°, 45°$.

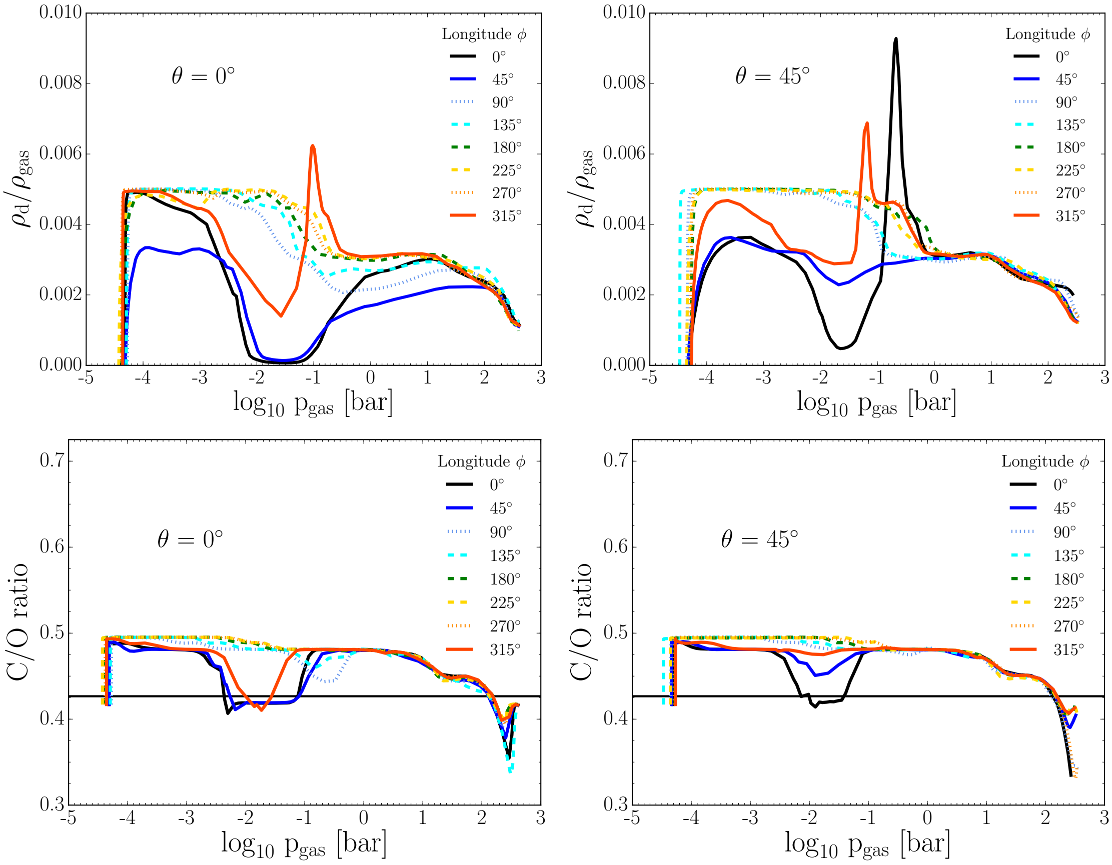

Figure 3.9: Gas properties as a function of gas pressure for $\Delta\phi = +45°$ longitude intervals from the cloud formation process. **Top Row:** Dust-to-gas ratio ρ_d/ρ_{gas} at latitudes $\theta = 0°$ and 45°. **Bottom Row:** C/O ratio at latitudes $\theta = 0°$ and 45°. Solid, dotted and dashed lines indicate dayside, day-night terminator and nightside profiles respectively. The horizontal black line indicates solar C/O ratio. Regions of decreasing ρ_d/ρ_{gas} and C/O indicate cloud particle evaporation.

We calculate the dust-to-gas ratio and the C/O ratio of our cloud structures. Figure. 3.9 shows the local dust-to-gas ratio of the sample trajectories at latitudes $\theta = 0°$ and $45°$ respectively. Dayside profiles show increases and decreases in dust-to-gas ratio corresponding to regions of nucleation/growth and evaporation. Nightside profiles show less cloud particle evaporation throughout the upper atmosphere, with only small changes in the dust-to-gas ratio which starts to drop off from $\sim 10^{-2}$ bar. Figure. 3.9 shows the local gaseous C/O ratio of our sample trajectories at latitudes $\theta = 0°$ and $45°$ respectively. These follow similar trends to the dust-to-gas ratio. The C/O ratio lowers where evaporation of cloud particles releases their oxygen bearing materials, replenishing the local gas phase, The abundance of C is kept constant at $\epsilon^0_{\rm C} = 10^{-3.45}$ (solar abundance) and is not affected by the formation of cloud particles in our model. Dayside equatorial profiles show C/O ratio dips by ∼5% below solar values at pressures of $10^{-2.5} \ldots 10^{-1}$ bar. The $\phi = 0°$, $\theta = 45°$ profile also shows a dip below solar values at similar pressure levels. Apart from these localised regions of oxygen replenishment, the C/O ratio remains above solar values for the majority of the atmospheric profiles; except from the cloud base, which is enriched with oxygen by 10%-20% for all profiles.

3.5 Limitations of 1D Mixing Approach

Some key limitations of the 1D mixing approach are outlined below. As a time independent, static approach, this method does not capture the effects of horizontal and vertical flows as well as time-dependent particle settling. Although, in this study, we attempt to capture the inhomogeneous nature of the atmosphere by using profiles from different parts of the atmosphere. The vertical mixing is a key input quantity to the model, the mixing tracers using a GCM of Parmentier et al. (2013) suggest that vertical mixing may be too strong in many 1D chemical models using similar mixing length approaches. The cloud opacity is also not fed back into the scheme and has no effect on the temperature structure, however, a parameterised cloud opacity was included in the RHD model of Dobbs-Dixon & Agol (2013), so the temperature structure may be more accurate than cloud free input.

3.6 Conclusions

From the results of our 2-model 1D approach, HD 189733b contains highly suitable thermochemical conditions for cloud formation and growth. Cloud formation can reduce gas phase element abundances by several orders of magnitude The cloud formation structures also depend greatly on the local thermodynamic and vertical mixing conditions. Particle nucleation and therefore size and settling are different for each profile, especially between the dayside and nightside of simulated planet. Cloud particles are more thermally stable on the nightside, we expect a richer cloud particle composition for nightside profiles and more stable materials (TiO_2, Fe, Al_2O_3) to dominate the composition more of the hotter dayside.

4

Cloud Dynamics and Radiative-Hydrodynamic Modelling

4.1 Introduction

Atmospheres are intrinsically time-dependent, 3D objects and generally inhomogeneous in nature, with differences in cloud cover, temperatures and chemical composition with latitude, longitude and depth. A thorough investigation of the properties of exoplanet atmospheres must therefore include a time-dependent, 3D description of the atmosphere including the effects of a cloud component. 3D RHD/GCM models are required to be computationally efficient, hence simplified or reduced chemical schemes, in their 3D forms, are usually invoked. We apply the time-dependent cloud formation, kinetic cloud formation model of Chapter 2 to a 3D RHD model of HD 189733b. We investigate the spatial and temporal cloud properties of the simulation and how inhomogeneous cloud coverage affects the thermochemical environment of the hot Jupiter exoplanet.

4.2 3D RHD Modelling of Exoplanet Atmospheres

The 3D modelling of dynamic clouds for hot Jupiter atmospheres requires a coupled, time-dependent hydrodynamic, radiative-transfer and cloud formation model scheme. For this, time dependently evolving the 3D Navier-Stokes equations and a two-stream radiative transfer scheme (e.g. Dobbs-Dixon & Agol, 2013) coupled with a time dependent, 3D, cloud description (e.g. Woitke & Helling, 2003) is required to be carried out by the model. Gravitational settling of the cloud particles and element conservation under the influence of cloud formation must also be taken into account. In this study, the method of dust moments in Sect. 2.6 is combined with the RHD model of Dobbs-Dixon & Agol (2013) including the feedback of opacity.

4.2.1 3D radiative-hydrodynamic model

The radiative-hydrodynamic (RHD) model applied in this study combines the fully compressible 3D Navier-Stokes equations to a two-stream, frequency dependent radiative transfer scheme. Equations (4.1), (4.2) and (4.3) represent the continuity, momentum and energy conservation of a local fluid element respectively,

$$\frac{\partial \rho_{\rm gas}}{\partial t} + \nabla \cdot \left(\rho_{\rm gas}\mathbf{u}_{\rm gas}\right) = 0, \tag{4.1}$$

where $\rho_{\rm gas}$ [g cm^{-3}] is the hydrodynamic gas density and $\mathbf{u}_{\rm gas}$ [cm s^{-1}] the hydrodynamic gas velocity.

$$\begin{aligned}\frac{\partial \mathbf{u}_{\rm gas}}{\partial t} + \left(\mathbf{u}_{\rm gas}\cdot\nabla\right)\mathbf{u}_{\rm gas} = -\frac{1}{\rho_{\rm gas}}\nabla P_{\rm gas} + \mathbf{g} \\ -2\mathbf{\Omega}\times\mathbf{u}_{\rm gas} - \mathbf{\Omega}\times\left(\mathbf{\Omega}\times\mathbf{r}\right) + \nu\nabla^2\mathbf{u}_{\rm gas} + \frac{\nu}{3}\nabla\left(\nabla\cdot\mathbf{u}_{\rm gas}\right),\end{aligned} \tag{4.2}$$

where $P_{\rm gas}$ [dyn cm^{-2}] is the local gas pressure, $\vec{g}$=g$\mathbf{e}_r$ [cm s^{-2}] the gravitational acceleration in the radial direction, $\mathbf{\Omega}$ [rad s^{-1}] the rotational frequency of the planet, $\mathbf{r}$(r, ϕ, θ) [cm] the spherical coordinate radial distance vector and $\nu = \eta/\rho_{\rm gas}$ [cm^2 s^{-1}] the constant kinematic viscosity.

$$\left[\frac{\partial e_{\mathrm{gas}}}{\partial t} + (\mathbf{u}_{\mathrm{gas}} \cdot \nabla) e_{\mathrm{gas}}\right] = -P_{\mathrm{gas}} \nabla \cdot \mathbf{u}_{\mathrm{gas}} - \frac{1}{r^2} \frac{d}{dr}\left(r^2 F_r\right) + S_\star + D_\nu, \tag{4.3}$$

where e_{gas} [erg cm^{-3}] is the internal energy density of the fluid element, F_r [erg cm^{-2} s^{-1}] the radiative flux in the radial direction, $S_\star$ [erg cm^{-3} s^{-1}] the incident stellar energy density per second and D_ν [erg cm^{-3} s^{-1}] the local energy density per second from gaseous viscous heating.

4.2.2 Radiative-Transfer

For the radiation field, the heating due to stellar irradiation $S_\star$ [erg cm^{-3} s^{-1}] is given by

$$S_\star = \left(\frac{R_\star}{a}\right)^2 \sum_{b=1}^{nb} \frac{d\tau_{b,\star}}{dr} e^{-\tau_{b,\star}/\mu_\star} \int_{\nu_{b,1}}^{\nu_{b,2}} \pi B_\nu(T_\star, \nu)\, d\nu, \tag{4.4}$$

where $R_\star$ [cm] and a [cm] are the stellar radius and semi-major axis, respectively, r [cm] the radial coordinate, $\mu_\star = \cos\theta$ the cosine of the angle between the normal and the incident stellar photons, accounting for the slant path from a vertically defined optical depth and $\tau_{b,\star}$ the optical depth of stellar photons for wavelength band b given by

$$\tau_{b,\star}(r) = -1.66 \int_{R_{\mathrm{p}}}^{r} \rho_{\mathrm{gas}} \kappa_{b,\star} \mathrm{d}l. \tag{4.5}$$

Where 1.66 is the diffusivity factor, an approximation that accounts for an exponential integral that arises when taking the first moment of the intensity to calculate the flux (Elsasser, 1942) and κ_b [cm^2 g^{-1}] the opacity for wavelength band b (Eq. 4.14). In the two-stream approximation, the net radial flux, $F_r\,(\tau_b)$ [erg cm^{-2} s^{-1}], for wavelength band b in the upward or downward direction is

$$F_r\,(\tau_b) = \sum_b \left(F_{\uparrow,b}\,(\tau_b) - F_{\downarrow,b}\,(\tau_b)\right). \tag{4.6}$$

The propagation of radiation intensity in the downward $F_{\downarrow,b}$ and upward $F_{\uparrow,b}$ direction at each cell (two-steam approximation) is given by

$$F_{\downarrow,b}\left(\tau_b\right) = \int_0^{\tau_b} S_b(T_{\rm gas}) e^{-\left(\tau_b - \tau_b'\right)} d\tau_b', \tag{4.7}$$

and

$$F_{\uparrow,b}\left(\tau_b\right) = S_b\left(T_{bot}\right) e^{-\left(\tau_{b,bot} - \tau_b\right)} + \int_{\tau_{b,bot}}^{\tau_b} S_b(T_{\rm gas}) e^{-\left(\tau_b' - \tau_b\right)} d\tau_b', \tag{4.8}$$

respectively, where S_b [erg cm^{-2} s^{-1}] is the source function given by the wavelength integrated Planck function at the local temperature (T = T$_{\rm gas}$),

$$S_b(T_{\rm gas}) = \int_{\nu_{b,1}}^{\nu_{b,2}} \pi B_\nu(T_{\rm gas}, \nu) d\nu. \tag{4.9}$$

$S_b(T_{bot})$ in Eq. (4.8) is the contribution of energy emitted from the interior of the planet, below which the planet is assumed to emit as a blackbody. This interior contribution to the upward flux is fixed to match the observed radius (Dobbs-Dixon & Agol, 2013). Stellar heating is fully accounted for in Eq. (4.4).

Gas and Dust Opacities

We calculate the cloud opacity at wavelengths corresponding to the 31 wavelength opacity bin edges used in Showman et al. (2009). The cloud opacity is then averaged across the wavelength range of the bins to calculate the cloud opacity for that band. For gas opacities, we use the temperature, density tabulated frequency dependent results from Sharp & Burrows (2007) Planck averaged over the wavelength bins of Showman et al. (2009).

Cloud particles are a large source of opacity, absorbing and scattering photons at optical and infrared wavelengths. We apply spherical particle Mie theory (Mie, 1908) (Sect. 2.8.2) in combination with effective medium theory (Sect. 2.8.1) to calculate the mixed material cloud opacity. Extinction efficiencies, Q$_{\rm ext}$(λ, a), for the local mean grain sizes $\langle$a$\rangle$ (Eq. 2.27) are calculated based on the Bohren & Huffman (1983) BHMie routines. We use two approximations for the size parameter (x = $2\pi\langle$a$\rangle$ / λ) limits of Mie theory. For large size parameters x $\geq$ 1000 we use the large particle, hard sphere scattering approximation where the absorption efficiency asymptotically tends towards zero, $Q_{\rm abs}$ = 0, and all extinction is assumed to be from scattering. In the large particle limit, extinction efficiency $Q_{\rm ext}$ is then

$$Q_{\rm ext} = 2. \tag{4.10}$$

For small size parameters x $< 10^{-6}$ we use the small metallic sphere particle limit approximation, as, for example, outlined by Gail & Sedlmayr (2014), where

$$Q_{\rm abs} = 4x\,{\rm Im}(\alpha) + \frac{2}{15}x^3\,{\rm Im}(\epsilon), \tag{4.11}$$

and

$$Q_{\rm sca} = \frac{8}{3}x^4\alpha\alpha^*, \tag{4.12}$$

where ϵ is the complex dielectric function and α = (ϵ - 1)(ϵ + 2). The second term in $Q_{\rm abs}$ contains the effect due to induction of eddy currents on the grain surface by the electromagnetic field of the photons. The $Q_{\rm sca}$ equation calculates the contribution to the total extinction from Rayleigh scattering. This approximation has been shown to produce similar results to Mie theory for very small size parameters (Gail & Sedlmayr, 2014). For all other size parameters the full Mie calculation is carried out. The mass extinction coefficient $\kappa_{\lambda,cloud}$ [cm^2 g^{-1}] at wavelength λ is then given by

$$\kappa_{\lambda,cloud} = Q_{\rm ext}(a)\pi a^2 n_{\rm d}/\rho_{\rm gas}, \tag{4.13}$$

where a = ⟨a⟩ is the mean grain size from Eq. (2.27). We calculate the cloud opacity at wavelengths corresponding to the 31 wavelength opacity bin edges used in Showman et al. (2009). The cloud opacity is then averaged across the wavelength range of the bins to calculate the cloud opacity for that band. For gas opacities, we use the temperature, density tabulated frequency dependent results from Sharp & Burrows (2007) Planck averaged over the wavelength bins of Showman et al. (2009). The total band opacity from the gas and cloud $\kappa_{b,total}$ [cm^2 g^{-1}] is then given by

$$\kappa_{b,total} = \kappa_{b,gas} + \kappa_{b,cloud}. \tag{4.14}$$

This local total opacity is treated as a purely absorptive extinction in the radiative transfer scheme (i.e. no scattering effects are taken into account). This will add an error in the cloudy simulations as both inward and outward scattered light will affect the energy budget of the simulation.

4.3 Cloud Modelling with 3D RHD Simulations

In this section we outline our cloud formation approach, numerical approach, initial conditions and convergence properties for our RHD and cloud formation model. The addition of our cloud formation model the RHD model adds additional costs to the simulation times. For example, the $\sim$60 simulated days presented here took $\sim$20 Earth days using 64 cores. In contrast, the simulation without clouds runs approximately 30 times faster.

4.3.1 Cloud formation and element abundance

We consider the homogeneous nucleation of TiO_2 seed particles based on $(TiO_2)_N$ cluster data from Jeong et al. (2003); Lee et al. (2015b). We consider five simultaneous surface materials, TiO_2[s], SiO[s], SiO_2[s], Mg_2SiO_4[s], $MgSiO_3$[s] with 22 of the corresponding surface chemical reactions found in Helling et al. (2008b). The local cloud properties are locally time-dependently computed for each computational domain while the flux of the moments through 3D space can be calculated using an advection scheme. This is a significant improvement over our previous 1D methods of Chapter 3 which rely on mixing timescale arguments to calculate clouds properties and do not consider transport in horizontal directions. We solve Eq. (2.17) for four element abundances: Ti, O, Si and Mg and assume a constant solar element abundance for all other elements. We assume horizontal and meridional frictional coupling of the dust and gas phase ($\mathbf{u}_{\rm d,h,m} = \mathbf{u}_{\rm gas,h,m}$). Vertical decoupling between the dust and gas phase is applied given by Eq. (2.55) ($\mathbf{u}_{\rm d,vert} = \mathbf{u}_{\rm gas,vert} + \mathbf{v}_{\rm dr}$).

We evolve the Navier-Stokes equations (Eq. 4.1, 4.2 and 4.3) over a spherical grid with a resolution of ($N_{\rm r}$, N_ϕ, N_θ) = (100, 160, 64), where r is the radial direction, ϕ the longitude and θ the latitude. The upper radial boundary is allowed to vary between $\sim 10^{-5}$ and 10^{-4} bar depending on dynamical properties and the lower boundary is fixed at $\sim$500 bar. Vertical velocity dampening (sponge zone) is implemented near the upper boundaries of the simulation, common to GCM models (e.g. Mayne et al., 2014). We account for flow over polar regions by the method found in Dobbs-Dixon et al. (2012).

One integration of the kinetic cloud formation chemistry can take ∼20-30 times the computational time of a single hydrodynamic timestep. Therefore, the cloud formation chemistry (r.h.s. Eq. 2.22) is integrated every 10 hydrodynamic timesteps to update the local cloud particle properties. The drift velocity $\mathrm{v}_{\mathrm{dr}}(\vec{r})$ and cloud opacity $\kappa_{b,cloud}$ are updated after the cloud formation chemistry. At every hydrodynamic timestep, cloud moments; $\mathrm{L}_j(\vec{r})$, material volume composition; $\mathrm{L}_{3,s}(\vec{r})$ and gaseous element abundances; $\varepsilon_i(\vec{r})$ are also advected around the globe.

Additionally, we take a number of physically based assumptions to reduce the number of cloud chemistry iterations required and to ensure physical solutions to the cloud properties. During an evaporation event, the maximum integration step size is reduced by half to capture the evaporation process more consistently. We limit evaporation of grains to the seed particle size (∼0.001 μm); should the integrator attempt to evaporate the moment solutions below seed particle sizes, the end solution is assumed to be at the local seed particle values. At this point, should the seed particles be thermally unstable ($\chi^{\mathrm{net}}_{\mathrm{TiO_2[s]}}(\vec{r}) < 0$ cm s^{-1}) then all seed particles are assumed to be evaporated (i.e. $L_j(\vec{r}) = 0$) and the Ti and O elements returned to the gas phase by Eq. (4.15). This condition is only met at the hottest, deepest parts of the atmosphere ($\mathrm{T}_{\mathrm{gas}} > 2300$ K) in our simulations. Thermal stability may prevail to higher gas temperatures if other high-temperature condensates are included.

We limit the calculation of the dust chemistry to regions where the number density of grains is $n_{\mathrm{d}}(\vec{r}) > 10^{-10}$ cm^{-3} unless the local nucleation rate is $J_*(\vec{r}) > 10^{-10}$ cm^{-3} s^{-1}. This condition ensures that only regions that are efficiently nucleating or already contain a significant number of cloud particles are integrated. This criterion ensures that deeper atmospheric regions ($\mathrm{p}_{\mathrm{gas}}$ $>$ 10 bar) which have a negligible nucleation but large growth rate, where a small number of cloud particles grow rapidly large (>1 cm), do not occur. Without this criterion, these regions become computationally challenging as the drift velocity (Eq. 2.57) becomes large (∼ speed of sound) for these particles. The hydrodynamic Courant-Friedrichs-Lewi [CFL] timestep condition then limits the hydrodynamic timestep to unfeasibly low values. The cloud opacity and drift velocity in regions which contain very little cloud particles ($n_{\mathrm{d}}(\vec{r}) < 10^{-10}$ cm^{-3}) are assumed to be zero. For regions where $n_{\mathrm{d}}(\vec{r}) > 10^{-10}$ cm^{-3}, a lower bound cloud opacity of $\kappa_{\mathrm{cloud}} = 10^{-7}$ cm^2 g^{-1} across all wavelength bands is implemented to aid numerical stability. This is required since the results of Mie theory in certain seed particle regions can approach floating point limits. This corresponds to a lower bound of $\mathrm{TiO_2}$[s] seed particle opacity ($\kappa_{cloud}(\lambda, a_{seed}) \geq 10^{-7}$ cm^2 g^{-1}) at optical wavelengths.

Furthermore, cells with very small growth/evaporation rates of $|\chi_{\rm net}(\vec{r})| < 10^{-20}$ cm s^{-1} are assumed to remain constant with respect to the dust moments. Only cells which have local conditions that are significant departures from the equilibrium solution ($\chi_{\rm net}(\vec{r}) = 0$) are integrated in time. We found integrating cells with $|\chi_{\rm net}(\vec{r})| < 10^{-20}$ cm s^{-1} was computationally prohibitive and did not produce significantly different results.

The need to only update the r.h.s. of the dust moment equation every 10th hydrodynamic timestep may lead to a fast transport of cloud particles into high temperature regions where they will evaporate. This volatile material would evaporate rapidly at some material dependent "evaporation window" as it passed into these unstable regions. The dust moment and element conservation equations become numerically stiff for such an intense evaporation, hence, the dust moments would approach phase equilibrium (i.e. when evaporation stops) in very small timesteps. Small timesteps for the intense evaporation regions are necessary in order to solve the element conservation equation (Eq. 2.17) to the best possible precision. To overcome this numerical challenge, we introduce a scheme where, should the integration timestep be too low at the beginning of the cloud chemistry integration, a fraction of the volatile materials are instantly evaporated back into the gas phase. This process is repeated until integration of cloud properties can be computed in a reasonable time. Growing or (near-)stable ($|\chi_{\rm s}(\vec{r})| > 10^{-30}$ cm s^{-1}) material are not altered and assumed to remain constant. The return of elements to the gas phase from each evaporation species s due to an instantaneous evaporation event is given by (Woitke, 2006)

$$\varepsilon_i(\vec{r}) = \varepsilon_i^{\rm b}(\vec{r}) + \frac{\nu_s 1.427 \text{amu}}{V_{0,s}} \Delta L_{3,s}(\vec{r}), \tag{4.15}$$

where $\varepsilon_i^{\rm b}(\vec{r})$ is the element abundance before the instant evaporation step, $\nu_{i,s}$ the stoichiometric coefficient of element i in species s and 1.427 amu the conversion factor between gaseous mass density $\rho_{\rm gas}$ and Hydrogen nuclei density $n_{\langle H \rangle}$ and $\Delta L_{3,s}(\vec{r})$ the difference in grain volume of species s before and after instant evaporation.

This scheme has the added benefit of evenly spreading computational load, since each evaporating cell has a more equal work load. Additionally, since the surface chemical growth of the particles occurs in second-minute timescales (Helling et al., 2001, 2004); if too much of a material is instantly evaporated off, the material can quickly grow back to an equilibrium solution before the end of one hydrodynamical time-step.

4.3.2 Initial conditions

For initial conditions, we use a well converged RHD model (total simulated time: ∼420 Earth days) of Dobbs-Dixon & Agol (2013) which included a parameterised cloud opacity (Eq. 4.16). This parameterised opacity is switched off in our simulations. The initial 3D ($T_{\rm gas}$, $p_{\rm gas}$, $\mathbf{v}_{\rm gas}$) structures do not vary significantly from the published results. As in Dobbs-Dixon & Agol (2013) we use a tidally locked HD 189733b set-up with the rotation rate equal to the orbital period (2.22 days). We assume an initial solar abundance of elements throughout the globe given by Asplund et al. (2009).

To set up the 3D RHD simulation, the dust properties are integrated each hydrodynamic timestep for the first 100 iterations and the effects of cloud opacity are neglected until ∼5.5 Earth days into the simulation. During this time, larger sized grains with $\langle a \rangle > 1$ μm will have gravitationally settled from the upper atmosphere to their pressure supported regions (∼1 bar). After these first steps, the opacity of the cloud particles at all positions is accounted for in the radiative transfer scheme.

4.3.3 Convergence tests

We investigate the present state of the model convergence by examining the the horizontal kinetic energy density $E_{\rm kin,h} = \rho_{\rm gas}\, \mathbf{u}_{\rm h}^2\, /\, 2$ [erg cm^{-3}] and root-mean-square (r.m.s.) horizontal + meridional velocity $\mathbf{v}_{\rm rms} = \sqrt{(\mathbf{u}_{\rm h}^2 + \mathbf{u}_{\rm m}^2)/2}$ [m s^{-1}] zonal and meridional averaged at pressure iso-bars. These two quantities show how the global hydrodynamic velocity structure of the atmosphere is changing with atmospheric pressure and with time to check the state of the simulation with respect to a possible statistical steady state. We introduce two properties for the cloud structure, the cloud number density $n_{\rm d}$ [cm^{-3}] (Eq. 2.26) and the equilibrium vertical drift velocity $\mathbf{v}_{\rm dr}$ [m s^{-1}] (Eq. 2.57), which are zonally and meridionally averaged at each iso-bar. Together, these two quantities take into account the time evolution of the global density structure of cloud material as well as the grain size and composition due to their respective dependences.

Overall, the horizontal and meridional mean gas kinetic energy density, r.m.s. velocity and cloud property contours remain reasonably constant throughout our study integration period.

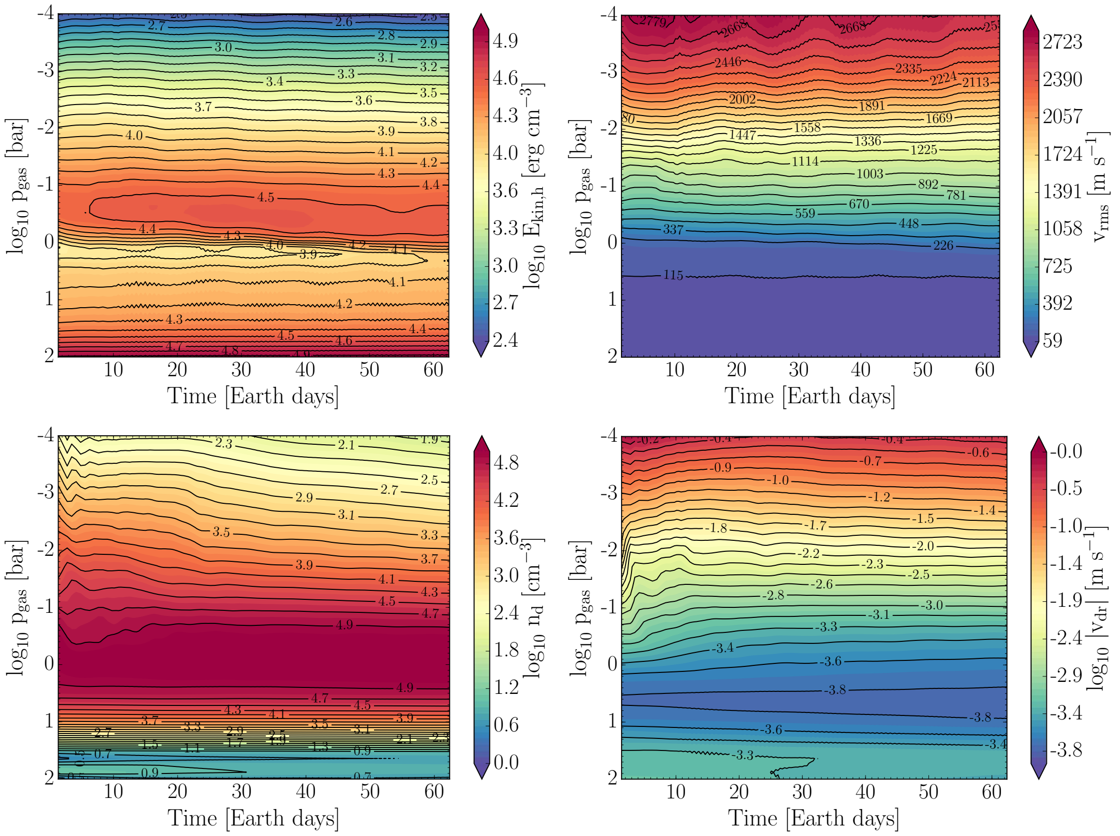

Figure 4.1: Mean global hydrodynamic and cloud properties as function of local gas pressure during ~60 Earth days of simulation. **Top:** Kinetic energy density $\log_{10}$ $E_{\rm h,kin}$ [erg cm^{-3}] (left) and global mean r.m.s. velocity $\mathbf{v}_{\rm rms}$ [m s^{-1}] (right). **Bottom:** Global mean cloud particle number density $\log_{10}$ $n_{\rm d}$ [cm^{-3}] (Eq. 2.26, left) and drift velocity $\log_{10}$ $|\mathbf{v}_{\rm dr}|$ [m s^{-1}] (Eq. 2.57, right). Parallel contour lines indicate that the global properties of the chosen value in the atmosphere, at that pressure iso-bar, are not changing significantly with time. Note: there is no spin-up period since we use of a well converged continuation simulation of Dobbs-Dixon & Agol (2013) as initial conditions.

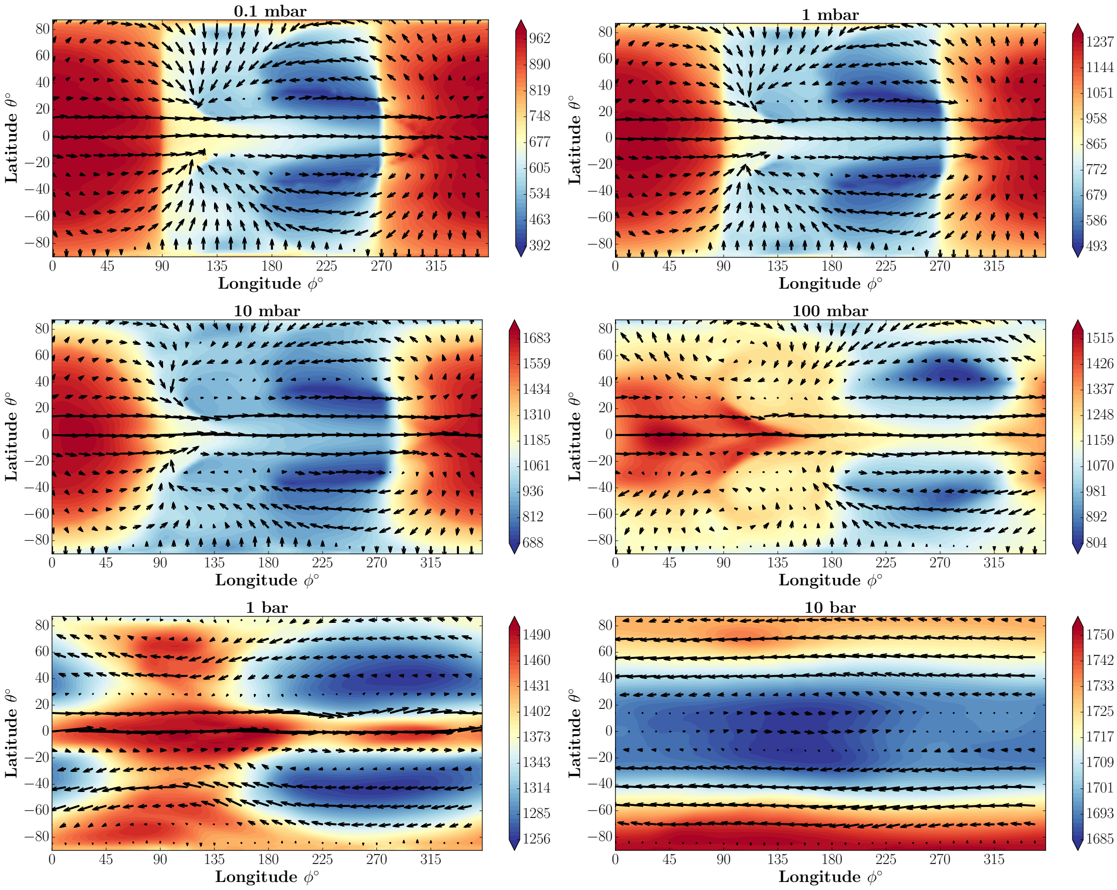

Figure 4.2: Each panel shows T_{gas}[K] (colour bar) and the velocity field (given by the velocity vector $|\mathbf{u}| = \sqrt{\mathbf{u}_h^2 + \mathbf{u}_m^2}$) (arrows) at different atmospheric pressure iso-bars at $p_{gas} = 0.1$, 1, 10, 100 mbar and 1, 10 bar for different ϕ (longitudes) and θ (latitude). Note: the colour bar scale is different for each plot. The sub-stellar point is located at $\phi = 0°$, $\theta = 0°$.

This suggests that the horizontal and meridional gas and cloud structures are not significantly varying in time during the ∼60 Earth days simulated here, and so further changes to the cloud structure are likely to come from the longer timescale vertical motions. An integration time of ∼ 60 days does not capture the longer vertical settling timescales (> 1000 days; Parmentier et al. 2013) of small particles (< 0.1 μm) in the upper atmosphere, nor the larger (∼ 1 μm) particles at the clouds base at ∼ 1 bar.

4.4 3D RHD Simulation of HD 189733b Including Clouds

This section presents our results regarding the combined modelling of cloud formation and radiative hydrodynamics for the giant gas planet HD 189733b. We use snapshot results of our simulation at 65 Earth days to illustrate the global cloud formation structures. We split our results into two broad areas, the gas phase properties such as temperature profiles (Sect. 4.4.1)

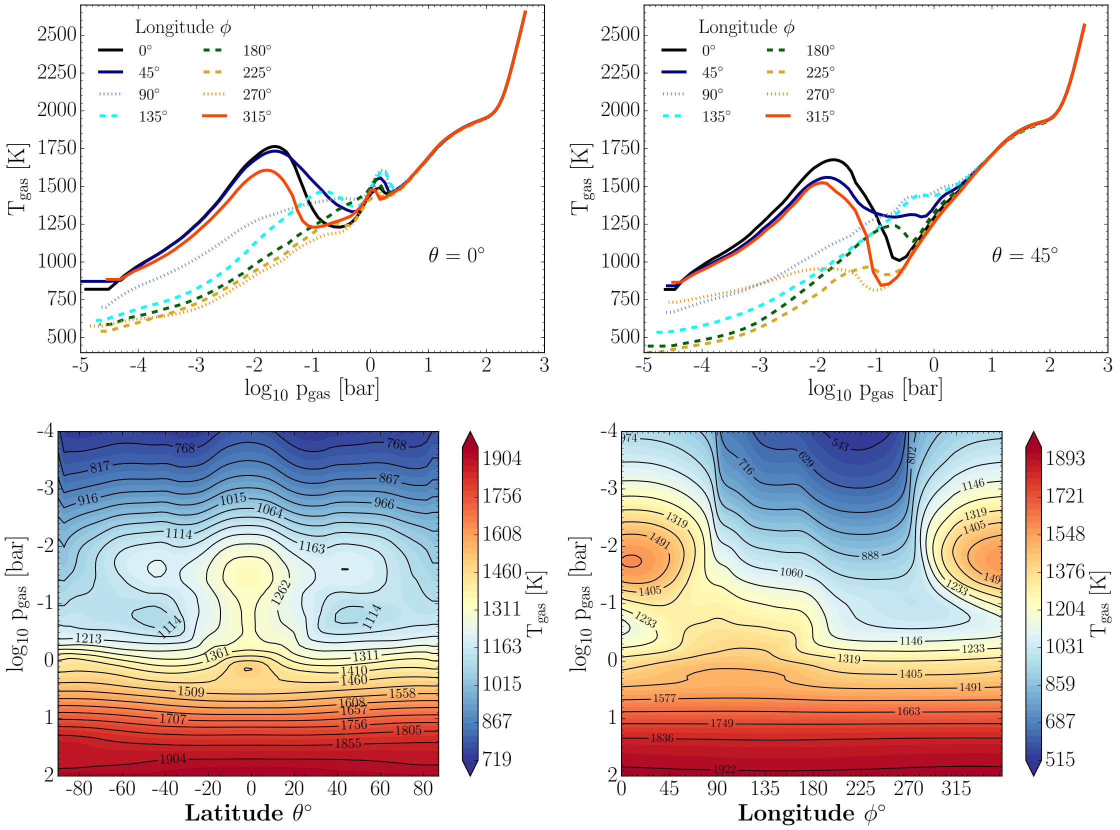

Figure 4.3: Top: 1D (T_{gas}, p_{gas}) trajectories at latitudes $\theta = 0°$ (left) , 45° (right). Dayside profiles (solid) show steep temperature inversions at ∼10 mbar, especially at higher latitudes. Nightside (dashed) and terminator (dotted) profiles have smaller inversions. **Bottom:** Zonal (left) mean T_{gas} [K] as a function of atmospheric pressure and meridional (right) mean T_{gas} [K] as a function of atmospheric pressure. The largest differences in latitudinal temperature contrasts occur from 10mbar to 1bar. The temperature is generally isothermal at atmospheric regions at pressures >5 bar.

and horizontal velocity (Sect. 4.4.2); and the cloud properties such as cloud particle number density structures (Sect. 4.5.1), mean cloud particle grain sizes (Sect. 4.5.2) and material composition (Sect. 4.5.3). Section 4.5.4 presents the depletion/replenishment of gas phase elements due to cloud formation processes and examines the hydrodynamic transport of elements from dayside to nightside. A global summary of the results and cloud formation physics is presented in Sect. 4.5.5. Section 4.6 presents the band by band gas and dust wavelength dependent opacity of the model in order to examine the radiative effects of cloud opacity on the temperature structure of the simulation.

4.4.1 Global temperature profiles

The local thermodynamic quantities like gas temperature and gas pressure, the local element abundances, determine the local cloud formation processes. The resulting cloud particles affect the local temperatures through their opacity, which in turn is coupled to the local pressure and density through the equation of state, Navier-Stokes and energy conservation equations. We therefore study the local gas temperature which will allow us to develop a global picture of the atmospheric temperature of hot Jupiters like HD 189733b under the influence of cloud formation.

A variation between dayside and nightside is present, with largest gradients in temperatures typically occurring near the terminator regions, most apparent at 0.1, 1 and 10 mbar (Fig. 4.2). The larger hydrodynamic velocities (super-sonic jet streams) at equatorial regions advects energy density Eastward, resulting in a longitude offset of the temperature maximum by $\phi \sim$ 20-40° East compared to the sub-stellar point $\phi = 0°$ where the planet receives maximum irradiation from the host star. This is most apparent at 100 mbar and 1 bar in Fig. 4.2. Differences in temperature (>100 K) between equatorial regions and mid-high latitudes are present in upper atmospheric regions. At depths >5 bar the local gas temperature starts to become more uniform in longitude and latitude. Hottest upper atmosphere regions ($T_{\rm gas} > 1500$ K) occur on the dayside at the peak of the temperature inversions ($\sim$ 10mbar). The coolest regions occur at nightside mid-latitudes with temperatures of ~400 K. These low temperature regions correspond to the large scale, nightside vortex regions where global hydrodynamical motions do not efficiently transport dayside hot gas towards.

Figure 4.3 displays the 1D ($T_{\rm gas}$, $p_{\rm gas}$) trajectories and shows that the atmosphere contains steep dayside temperature inversions at ~10 mbar. A second, smaller temperature inversion occurs at higher gas pressures ~1 bar for all longitudes at the equator ($\theta = 0°$; Fig. 4.3, top left). This temperature bump of 100...200K initially develops on the dayside due to a back-warming effect of the larger cloud opacity at ~1 bar (see also Sect. 4.6). Emission of radiation from hot gas at lower pressure is absorbed by the cloud layer at ~1 bar, resulting in localised heating of the gas. The hot gas is then transported to the nightside by the horizontal winds at this pressure (Fig. 4.4), resulting in a bump for all equatorial profiles at ~1 bar.

Figure 4.3 also shows the zonal and meridional mean gas temperature $T_{\rm gas}$ [K] as a function of depth. Zonal mean temperature show how the global temperature structure is changing with latitude and depth. This is useful in order to show global differences between equatorial and mid-high latitude regions for atmospheric properties. Horizontal contours indicate a more uniform variation in temperature in latitude, while vertical contours indicate a greater varia-

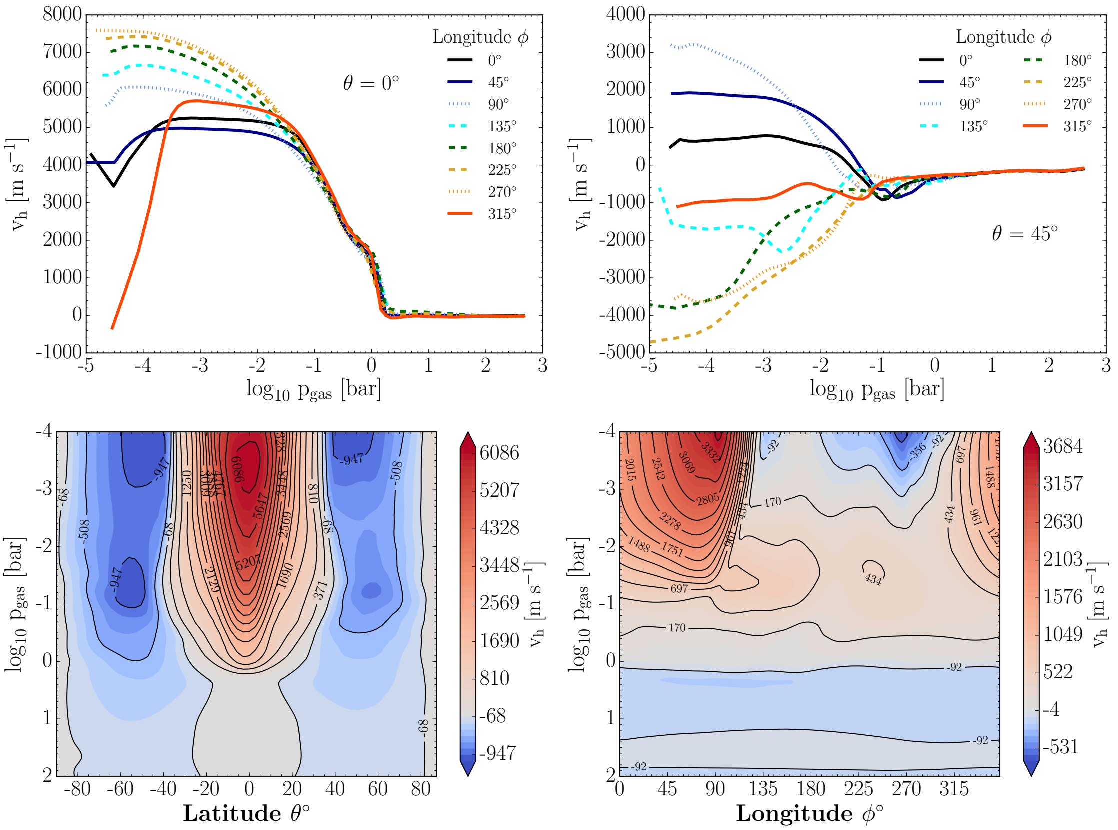

Figure 4.4: Top: 1D zonal/horizontal velocity v_h [m s^{-1}] trajectories at latitudes $\theta = 0°$ (left) , 45° (right). Equatorial regions show positive super-sonic flow confined to $\theta = \pm 30°$ latitudes, with maximum velocities greater than 7000 m s^{-1} at the upper nightside atmosphere. Negative direction velocities occur at higher latitudes ($|\theta| > 40°$). **Bottom:** Zonal (left) and meridional (right) mean horizontal velocity v_h [m s^{-1}] as a function of atmospheric gas pressure. Note: the colour scale bar has been normalised to 0 m s^{-1}. The strongest zonal velocities occur at the equator. Negative flows can be found at latitudes of $\theta \pm 40\ldots80°$.

tion with latitude. Meridional mean temperatures show how the global temperature structure is changing with longitude and depth. This is useful in order to show atmospheric differences between dayside and nightside regions. Horizontal contours indicate a more uniform variation in temperature in longitude, while vertical contours indicate a grater variation with longitude. The highest temperature regions at the upper atmosphere are concentrated at the equator, while a larger (>100 K) difference occurs between equatorial and higher latitude regions. From the meridional mean plot (Fig. 4.3, bottom right), a stream of hotter gas is present past the $\phi = 90°$ terminator at 100 mbar due to hydrodynamic flows advecting energy to the nightside and into deeper regions of higher pressure. The temperature becomes more uniform in longitude and latitude at deeper atmospheric regions >5 bar.

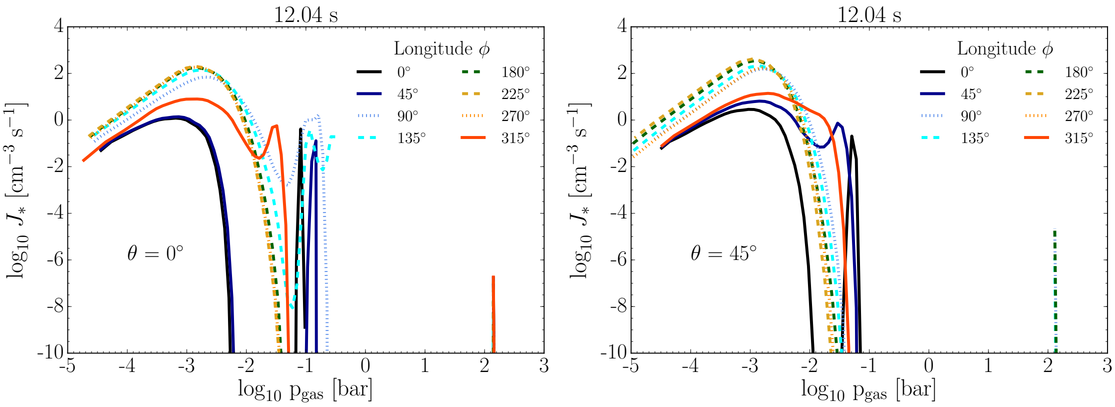

Figure 4.5: Top: 1D nucleation rate $\log_{10} J_*$ [cm^{-3} s^{-1}] trajectories ∼ 12 seconds into the simulation for latitudes $\theta = 0°$ (left) , 45° (right). The initial, most efficient nucleation regions occur at $p_{\rm gas} <$ 100 mbar for all atmospheric profiles. Dayside equatorial profiles at $\phi = 0°$, 45° have no nucleation occurring from ∼ 10-100 mbar, where the gas temperature is too high for the nucleation process. The greatest magnitude of nucleation of seed particles is at nightside, mid-high latitude regions at ∼ 1 mbar.

4.4.2 Atmospheric velocity field

3D RHD simulations provide information about the local and global hydrodynamical behaviour. This section studies the local and global velocity profiles of an atmosphere where cloud formation takes place. 1D profiles of zonal/horizontal velocity at the equator and mid-latitudes are presented in Fig. 4.4. These show that an upper atmosphere super-sonic jet of velocity > 4000 m s^{-1} at equatorial regions. A significant slow down of horizontal velocity at ϕ∼315° longitude occurs West of the sub-stellar ($\phi = 0°$) point. The maximum zonal velocities of > 7000 m s^{-1} occur on the nightside near the night-day $\phi = 315°$ terminator. At mid-latitudes ($\theta \sim 45°$), nightside ($\phi = 135 \ldots 270°$) regions contain super-sonic counter rotating flows with a velocity of < -2000 m s^{-1}. Figure 4.4 also shows the zonal mean gas velocity v_h [m s^{-1}] as at different latitudes and atmospheric pressures. This shows that there is supersonic jet flow at the equator in the West-East direction. Counter rotating flows occur at mid-latitudes with lower horizontal velocities than equatorial regions. Below ∼1 bar, the horizontal motions are slower and longitude, latitude uniform until reaching the inner boundary of our computational domain. The overall structural features remain similar to Dobbs-Dixon & Agol (2013).

4.5 Dynamic mineral clouds in HD 189733b

Giant gas planets like HD 189733b form clouds in their atmospheres from a chemically very rich gas phase. Section 3 has shown that the local thermodynamic conditions suggest that clouds form throughout the whole atmosphere of HD 189733b, although this result was con-

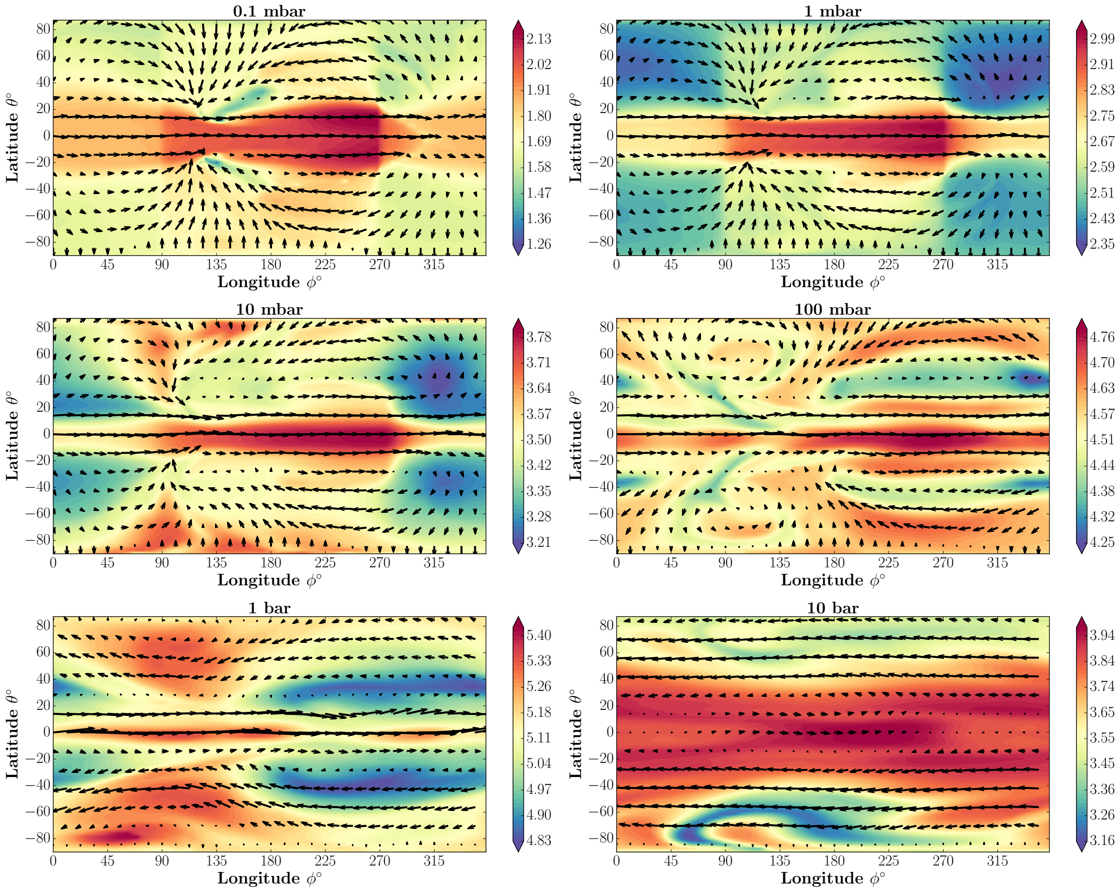

Figure 4.6: Cloud particle number density of grains $\log_{10} \mathrm{n_d}$ $[\mathrm{cm}^{-3}]$ (colour bar) and velocity field ($|\mathbf{u}| = \sqrt{\mathbf{u}_\mathrm{h}^2 + \mathbf{u}_\mathrm{m}^2}$) at 0.1, 1, 10, 100 mbar and 1, 10 bar for different ϕ (longitudes) and θ (latitude). Note: the colour bar scale is different for each plot. The sub-stellar point is located at $\phi = 0°$, $\theta = 0°$. Grains are typically more concentrated at equatorial nightside regions. The number density increases until reaching a maximum near 1 bar, which then gradually falls until the lower computational boundary at ~100 bar. The grains follow the flow patterns in the upper atmosphere, showing a preference to transport cloud particles to nightside equatorial regions. Regions deeper than ~1 bar show a more uniform distribution of cloud particles in latitude and longitude.

ducted in the non-global, 1D mixing approach. A similar conclusion was reach for HD 209458b in a comparison study of both planets (Helling et al., 2016a). While Chapter 3 and Helling et al. (2016a) present their results for stationary cloud structures, we now discuss the formation of clouds in a dynamic, time-dependent atmosphere in combination with the 3D atmospheric temperature and velocity fields. The following section shows how cloud properties like number density of cloud particles (Sect. 4.5.1), cloud particle sizes (Sect. 4.5.2) and the material composition (Sect. 4.5.3) develop in and form a dynamic cloud structure in an atmosphere with hydrodynamic jets and temperature inversions.

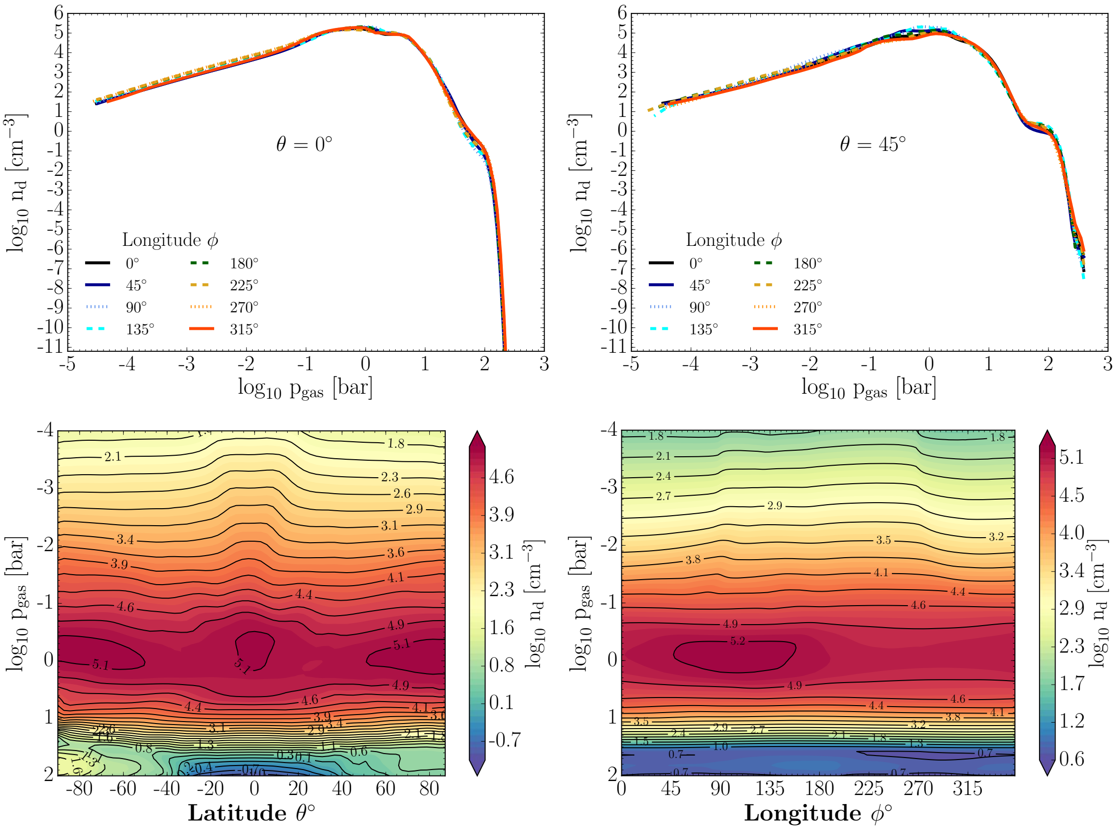

Figure 4.7: Top: 1D cloud particle number density $\log_{10}$ n$_d$ [cm^{-3}] trajectories at latitudes $\theta = 0°$ (left) , 45° (right). The density structure is similar across the longitude and latitude range. Density rises to a maximum of ~10^5 cm^{-3} at ~1 bar which contains the thickest and most opaque cloud regions. **Bottom:** Zonal mean (left) and Meridional mean (right) of the number density of grains $\log_{10}$ n$_d$ [cm^{-3}]. Note: the colour bar scale is different for each plot. The most cloud dense region is from ~100 mbar - 10 bar which is uniform across the globe. The thinest cloud layers are found at the simulation upper (~0.05 mbar) and lower (~500 bar) computational boundaries.

4.5.1 Seed formation and cloud particle density

The resultant number density structure of the cloud particles is a combination of the initial nucleation of seed particles and the hydrodynamic motions that transport cloud particles across the globe. Early in the simulation, nucleation begins the cloud formation process with the most efficient nucleation occurring at the colder nightside mid-latitude regions (Fig. 4.5). Nucleation is a quick processes, and a few minutes/hours into the simulation atomic Ti is already too depleted, limiting the nucleation of further cloud particles. The nucleation source term, $J_*(\vec{r})$, for the dust moment equations presented in Sect. 2.6 becomes negligible across the globe. Further evolution of the number density structure of cloud particles is then determined by the hydrodynamical and particle settling motions, rather than further nucleation. Hotter dayside temperature regions at ~10 mbar do not nucleate cloud particles at any point in time during the presently simulated epoch, but hydrodynamic motions transport cloud particles into these regions. Seed particles remain thermally stable in these regions throughout the whole time-span of the present simulation.

Figure 4.6 shows the number density n_d $[\mathrm{cm}^{-3}]$ of cloud particles after the ~60 Earth simulated days at isobars from 0.1 mbar - 10 bar. The vertical frictional coupling between dust particles and gas is large enough that cloud particles move with the 3D gas flow efficiently. This means, because we assume horizontal coupling, the highest cloud particle number density occurs near and at the equatorial regions for all atmospheric pressures. Drift velocities are small ($\mathbf{v}_\mathrm{dr}$ $\sim 10^{-4} \ldots 0.3$ m s^{-1}) throughout the atmosphere (Fig. 4.1), generally <10 % the local vertical gas velocity. This is a purely hydrodynamical effect and implies that the local grain sizes are not large enough to cause a significant de-coupling in the vertical direction. Cloud particle motion is therefore dominated by the horizontal gas velocity (i.e. $\mathbf{v}_\mathrm{dr} \ll \mathbf{u}_\mathrm{gas,v} < \mathbf{u}_\mathrm{gas,h}$).

The cloud structure predominantly follows the horizontal velocity structures in the atmosphere. For example, cloud particles entering the equatorial jet stream will typically spend a longer time circulating in these regions due to the lower flux of particles out from the central jet, either from meridional motions or vertical settling. Therefore, after a few days of simulation, after seed particle nucleation has become inefficient, equatorial regions are typically denser by ~0.5 magnitudes compared to mid-high latitudes. This is despite the majority of the seed particle nucleation taking place in nightside high-latitude regions, where the flow speed is typically slower, in the first hours of the simulation. There is a build up of material on approach to the $\phi = 270°$ terminator corresponding to regions of highest horizontal velocity ($u_h \sim 7000$ m s^{-1}). This is due to the equatorial jet transporting material quickly around to the nightside and slowing down significantly (Fig. 4.4) when reaching the night-day terminator. This build up of cloud particles means that the overall flux of particles entering the dayside regions is reduced. Additionally, particles entering the equatorial dayside regions are also transported quickly back onto the nightside by the equatorial jet, increasing the flux of particles towards the nightside. This leads to differences in clouds number density, n_d, between the dayside and nightside.

The cloud number density at 0.1, 1 and 10 mbar is also slightly (∼1 %) reduced by downward flows dragging the cloud particles to deeper depths near the day-night $\phi = 90°$ terminator and replenished by similar amounts at the upwelling night-day $\phi = 270°$ terminator. At deeper regions (>100 mbar), due to the lower vertical gas velocities, the effect of vertical velocity on the number density structure is negligible.

At depths greater than 100 mbar there is less difference in number density between nightside-dayside and equatorial-high latitude regions. Figure 4.7 show 1D trajectory plots and the zonal and meridional mean number density as a function of pressure. These clearly show a thicker cloud layer from ∼100 mbar - 10 bar which is relatively uniform throughout the planet which contains micron sized grains (Fig. 4.9). On average, the atmosphere is fairly uniform in number density with 10-20% differences between equatorial and mid-high latitude regions and comparable difference between nightside and dayside regions. This finding has implications for the cloud opacity which will therefore mainly be affected by the size of the cloud particles and their mixed material composition.

The large scale hydrodynamical motions explain the variety of the cloud number density seen on the dayside/nightside and show that cloud particle structures closely follow the horizontal, meridional and vertical gas dynamics at each atmospheric layer. Efficient nucleation of seed particles occurs at mid-high latitudes on the nightside early in the simulation. The gas dynamics then transports them, over time, to the equatorial regions where most of the cloud particles can be found by the end of the simulation. This result may change if frictional coupling of the cloud particles with the atmospheric gas is altered by a force that specifically acts on cloud particles and causes them to move with $\mathbf{u}_d \neq \mathbf{u}_{gas}$ in horizontal/meridional directions.

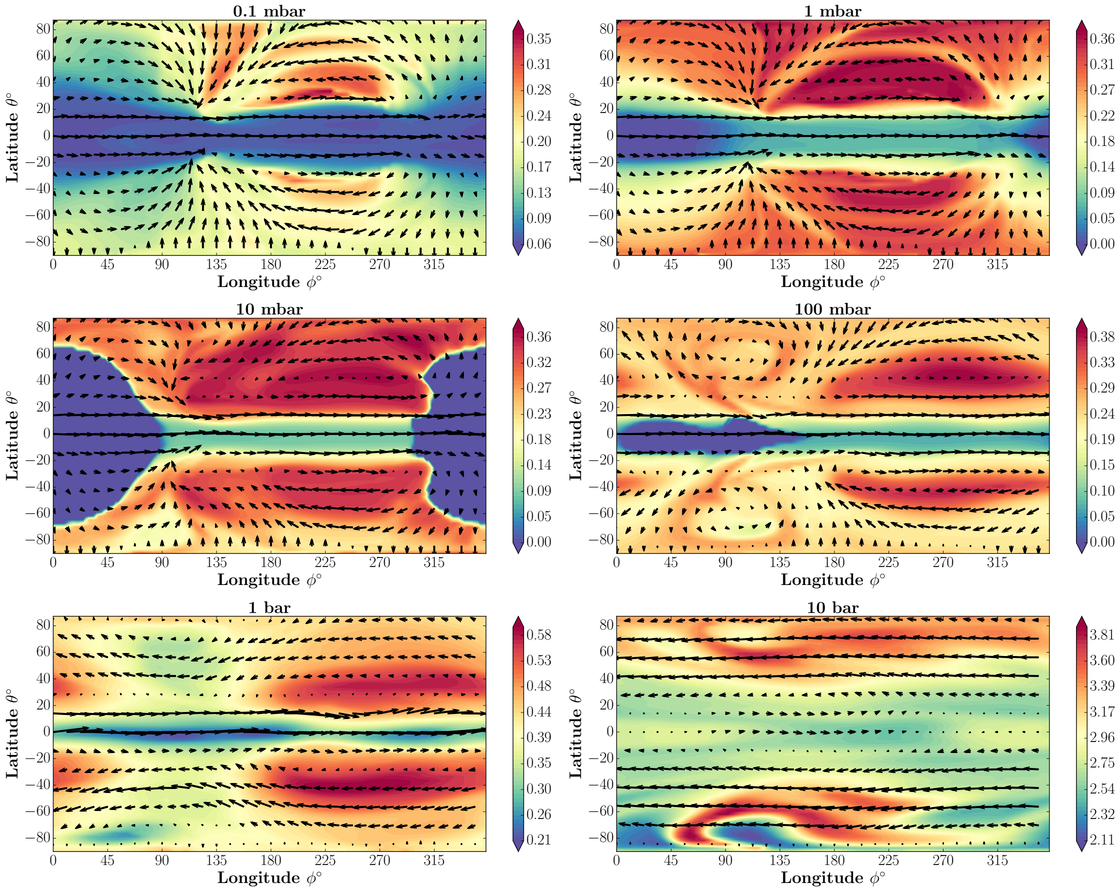

Figure 4.8: Mean grain size ⟨a⟩ [μm] (colour bar) and velocity field ($|\mathbf{u}| = \sqrt{\mathbf{u}_\mathrm{h}^2 + \mathbf{u}_\mathrm{m}^2}$) at 0.1, 1, 10, 100 mbar and 1, 10 bar for different ϕ (longitudes) and θ (latitude). Note: the colour bar scale is different for each plot. The sub-stellar point is located at $\phi = 0°$, $\theta = 0°$. The smallest grains at each layer typically reside at the equatorial regions. The largest grains are typically found on the nightside and at higher latitudes. Deep purple/blue coloured regions at 1, 10 and 100 mbar contain seed particles of sizes ~0.001 μm

4.5.2 Cloud particle sizes

Cloud particle sizes are a direct result of our cloud formation model (Chapter 2). Each growth species local growth/evaporation rate (Eq. 2.16) determines the local grain size, which is a function of the local number of elements and temperature. It also depends on the sinking/settling of cloud particles of different sizes over time as larger grains sink faster to higher pressure regions. Figure 4.8 shows the mean grain size ⟨a⟩ [μm] of cloud particles at pressure isobars from 0.1 mbar - 10 bar. Dayside regions from 0.1 mbar - 1 bar contain smaller grains while the nightside contains larger grains. This is most evident from the 0.1 and 10 mbar plots in Fig. 4.8 where larger grains (>0.1 μm) reside on the nightside while smaller grains (<0.1 μm) are found on the dayside. Asymmetry in grain size between equatorial and

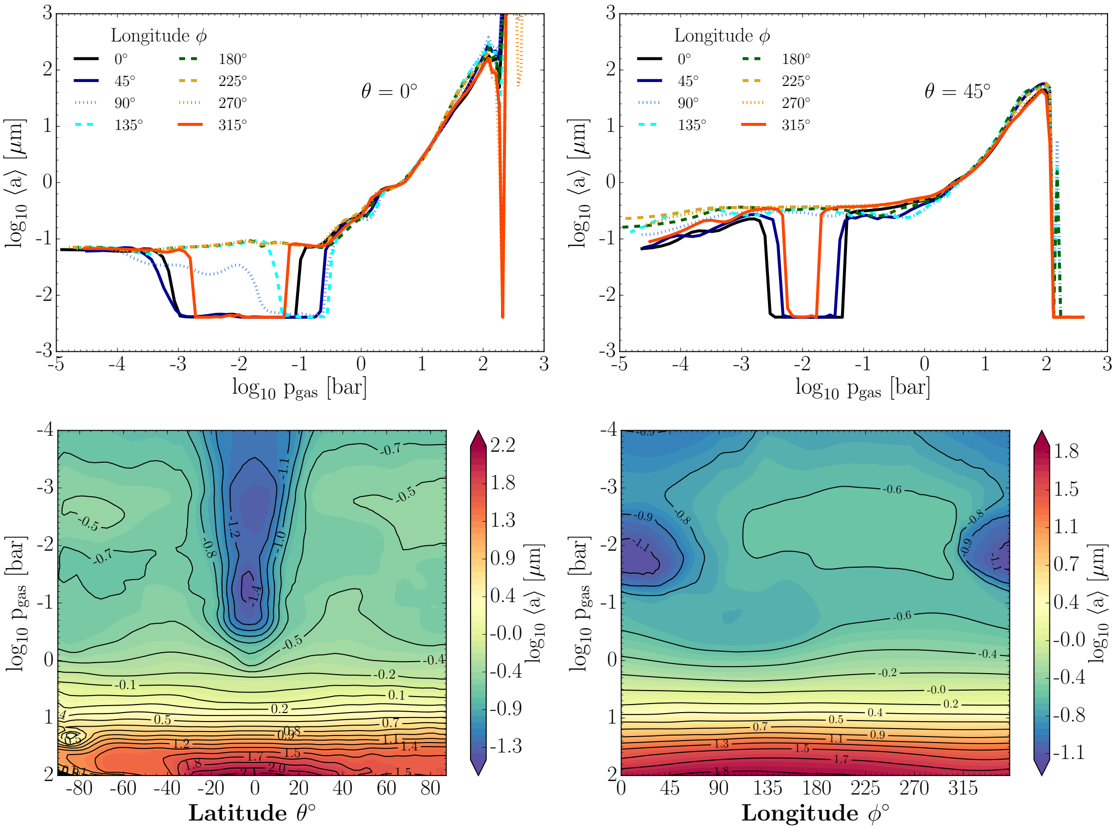

Figure 4.9: Top: 1D mean grain size $\log_{10}\langle a\rangle$ [μm] trajectories at latitudes $\theta = 0°$ (left) , 45° (right). Cloud particles are typically ∼0.1 μm from 0.01-1 mbar. Seed particles are present between 1-100 mbar for many profiles. **Bottom:** Zonal mean (left) and Meridional mean (right) average grain size $\log_{10}$ $\langle a\rangle$ [μm] as a function of pressure. The smallest grains are found on the dayside at pressures 1-100 mbar at the equatorial regions. The grain sizes are typically sub-micron above ∼5 bar and micron sizes below this pressure level.

mid-high latitudes is also seen, with equatorial regions containing the smallest grains at any given atmospheric pressure and larger grains supported at higher latitudes. At $\sim$10 mbar seed particles ($\sim$0.001 μm) reside on the dayside, corresponding to the highest upper atmosphere temperature regions where all other growth species are evaporated. At depths $\sim$ 1 bar particles grow to 1 μm sizes or larger. At such high densities, the frictional coupling to the gas phase is almost complete, resulting in very small drift velocities ($v_{\rm dr} < 0.001$ m s^{-1}).

In Fig. 4.9 the 1D trajectories at equatorial and mid-latitudes show a varied depth dependent grain size. Nightside and mid-latitude terminator regions typically contain grain sizes of $\sim$0.1 μm or less down to 1 bar where they grow to micron sizes and above. Dayside and the $\phi = 90°$, 135° equatorial profiles show the presence of seed particles from $\sim$0.1-100 mbar. Figure 4.9 shows the zonal and meridional averaged mean particle size (note: log scale) as a function of pressure. The atmosphere typically contains sub-micron particles down to a pressure level of $\sim$5 bar. The equatorial dayside regions contain the smallest particulates from 0.1-100 mbar. The nightside mean particle size is also $\sim$0.5-1 magnitudes larger than the dayside grains but remain sub-micron at these pressure levels. The largest particles ($\sim$0.1-1 mm) reside at the most dense parts of the atmosphere at gas pressures $>$ 10 bar. Gradients (up to 1 order of magnitude) in cloud particle size occur near the $\phi = 90°$ terminator, while grain sizes at the $\phi = 270°$ terminator remain relatively homogenous with longitude. This suggests that transit spectroscopy (Pont et al., 2013) would sample a variety of cloud particle sizes. The lower temperature regions at the center of vortex regions on the upper atmosphere nightside contain the largest cloud particles at each pressure level, suggesting that these vortex regions can efficiency trap and grow larger particles.

In summary, our model produces a variety of cloud particle sizes dependent on the local thermo-chemical conditions of the atmosphere. A large portion of the hot equatorial dayside contains seed particles of nm size in contrast to the cooler, nightside and mid-latitude regions where grain sizes can be $>$ 0.1 μm. We, however, note that the present results are limited to the growth of TiO_2[s], SiO[s], SiO_2[s], $MgSiO_3$[s], Mg_2SiO_4[s] materials, which suggests that the present grain sizes to be a lower limit.

4.5.3 Cloud material composition

Cloud particles form that are made of a mix of materials that are locally thermally stable. The composition of these material mixes changes depending on the local thermo-chemical con-

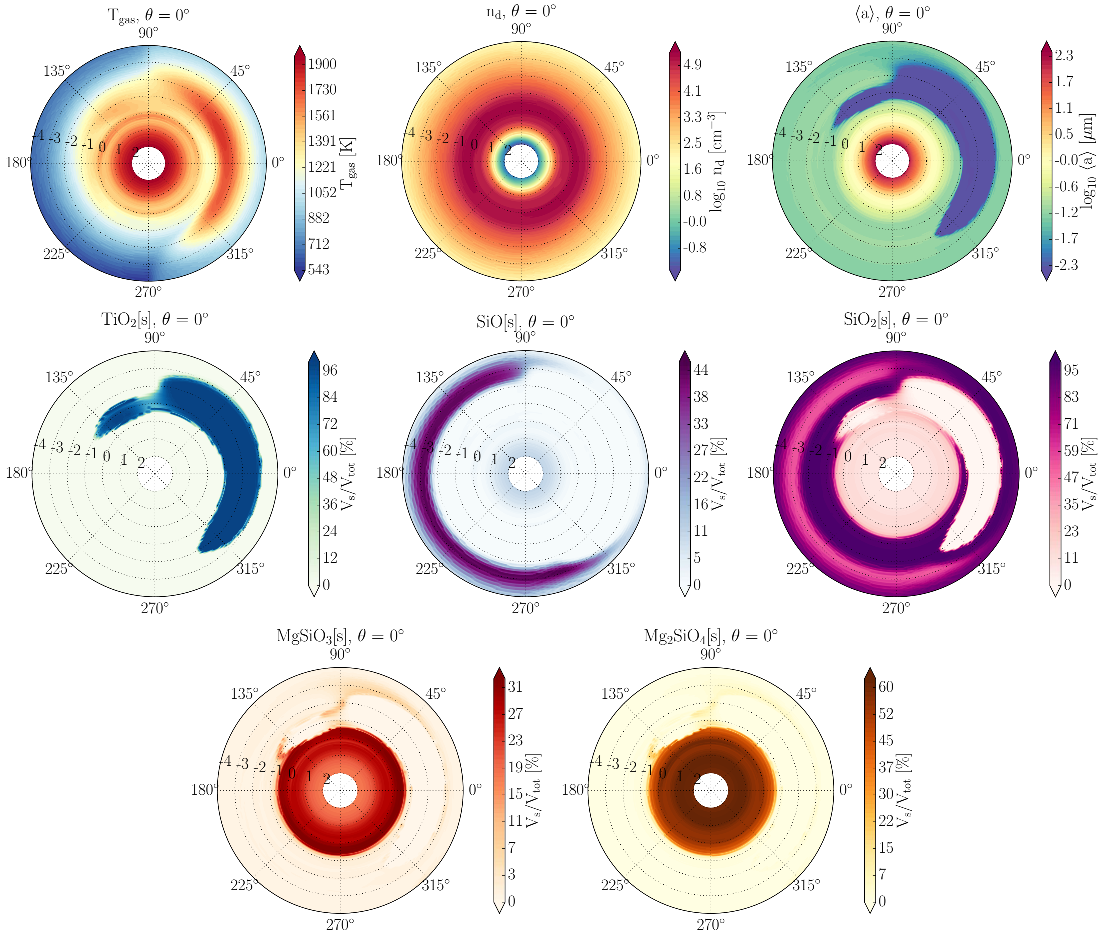

Figure 4.10: Meridional polar slices of atmospheric cloud properties at the equator ($\theta = 0°$). **Top:** Local gas temperature (T_{gas} [K]), cloud particle number density ($\log_{10} n_d$ [cm^{-3}]) and mean cloud particle grain size ($\log_{10} \langle a \rangle$ [μm]). **Middle:** Volume fraction (V_s/V_{tot} [%]) of the cloud particle composition containing TiO_2[s], SiO[s] and SiO_2[s]. **Bottom:** Volume fraction (V_s/V_{tot} [%]) of the cloud particle composition containing $MgSiO_3$[s] and Mg_2SiO_4[s]. Outer circular values denote longitude at intervals of $\phi = 45°$ from the sub-stellar point ($\phi = 0°$). Radial values indicate $\log_{10} p_{gas}$ isobars from 0.1 mbar - 100 bar. The globe is irradiated from the direction of the colour bars. Note: the size of the annulus is not scaled to planetary radius.

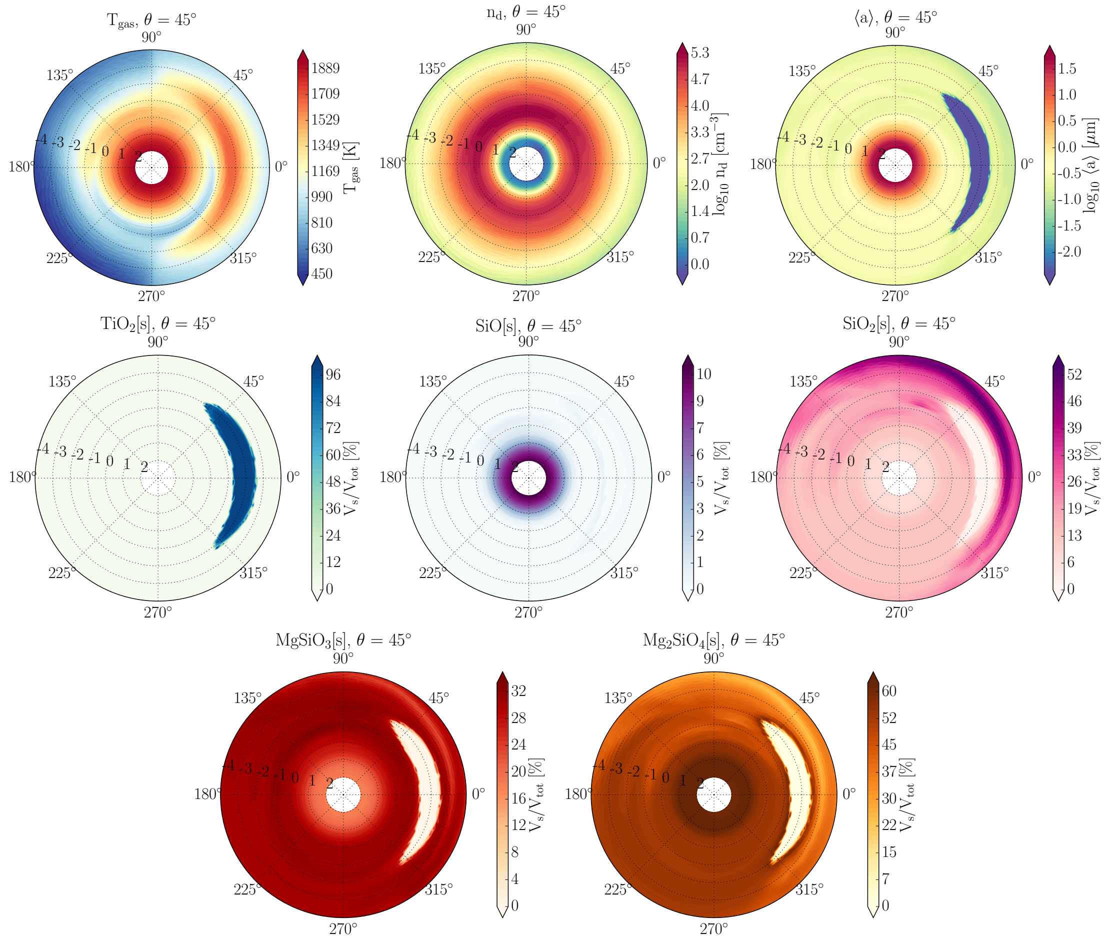

Figure 4.11: Meridional polar slices of atmospheric cloud properties at the equator ($\theta = 45°$). **Top:** Local gas temperature (T_{gas} [K]), cloud particle number density ($\log_{10}$ n_d [cm^{-3}]) and mean cloud particle grain size ($\log_{10}$ $\langle a \rangle$ [μm]). **Middle:** Volume fraction (V_s/V_{tot} [%]) of the cloud particle composition containing TiO_2[s], SiO[s] and SiO_2[s]. **Bottom:** Volume fraction (V_s/V_{tot} [%]) of the cloud particle composition containing $MgSiO_3$[s] and Mg_2SiO_4[s]. Outer circular values denote longitude at intervals of $\phi = 45°$ from the sub-stellar point ($\phi = 0°$). Radial values indicate $\log_{10}$ p_{gas} isobars from 0.1 mbar - 100 bar. The globe is irradiated from the direction of the colour bars. Note: the size of the annulus is not scaled to planetary radius.

ditions that a cloud particle may encounter when being advected due to the presence of a velocity field. Depending on the local temperature and element abundance properties, different solid growth species may dominate the bulk composition compared to others. The local composition of our mixed material cloud particles is therefore dependent on the local growth and evaporation rates as well as the transport of cloud particles and gas phase elements. Figure 4.10 and Fig. 4.11 show meridional slices of temperature, cloud particle number density, mean grain size and composition at latitudes $\theta = 0°$, $45°$ respectively. These show a complicated, non-uniform composition structure depending on what material is thermo-chemically favourable at each local atmospheric regions. These plots visualise the interplay between the gas temperature, number density, grain size and composition of the cloud particles.

TiO_2[s] is a high-temperature condensate which forms stable clusters that become subsequently more stable with size through homogenous nucleation. TiO_2[s] is therefore an efficient seed formation species and will also contribute to the material richness of the grain mantle by surface growth processes. TiO_2[s] rich grains ($V_s/V_{tot} \gtrsim 80\%$) are generally found between pressures of 1-100 mbar on the dayside of planet, corresponding to the hottest regions of the upper atmosphere. These regions primarily consist of near seed particle size ($\sim$0.001 μm) cloud particles due to the more volatile materials evaporating off the grain surface. These seed particles also appear on the nightside of the planet from $\phi = 90°$ to $\phi = 135°$ at $\sim$100 mbar due to the equatorial jet efficiently circulating hot gas to the nightside and to greater depths. At mid-latitudes, pure TiO_2[s] grains are only found in regions with the highest local gas temperatures at $\sim$10 mbar, also seed particle sized. These seed particles are thermo-chemically stable. Elsewhere in the atmosphere, TiO_2[s] constitutes less than 5% of the grain volume. Other materials grow more efficiently due to the greater element abundance of their constituent elements. Deep atmospheric regions near the lower computational boundary ($\sim$500 bar) contain pure TiO_2[s] seed particles where other material is thermally unstable.

SiO[s] is typically $< 5\%$ of the volume fraction in most of the atmosphere. However, it is found in significant volume fractions of $> 33\%$ at the equatorial regions from $\phi = 90°$ to $\phi = \sim 315°$ at gas pressures of $p_{gas} \sim 0.1$-10 mbar. This corresponds to regions of lower gas temperature and density where Mg/Si-growth is unfavourable. SiO[s] can also be found at the hotter and denser inner atmosphere from 10-100 bar where SiO[s] contributes 10 % to the total volume of the cloud particles.

SiO_2[s] dominates ($V_s/V_{tot} \gtrsim 33\%$) the dayside equatorial upper atmospheric regions from 0.1-1 mbar. It is especially dominant at the upper hotter regions from 0.1-1 mbar where Mg/Si-materials are thermodynamically unfavourable with near 100% composition in some regions. Grain sizes at these regions are $\sim 0.1\ \mu$m. At mid-latitudes, SiO_2[s] contributes with >10 % to the total cloud particle volume at all longitudes and pressure levels, with large volume fractions >50 % at dayside pressures of 0.1-1 mbar.

$MgSiO_3$[s] is perhaps the most interesting species included our models since its optical properties have been used to fit transit spectra, Rayleigh slope observations. We find that it comprises a large amount ($V_s/V_{tot} > 20\%$) of the grain composition at mid-high latitudes and at all depths, excluding seed particle regions. However, at equatorial regions it can only be found at the deeper, denser parts of the atmosphere from 100 mbar. At equatorial longitudes from $\phi = 45°$-$90°$ at ~1 mbar it can be found to be 10-20 % of grain volume.

Mg_2SiO_4[s] is found to be the most abundant Mg/Si material. Mg_2SiO_4[s] and $MgSiO_3$[s] can be found in the same regions in the atmosphere, and follow similar trends for their thermal stability. However, Mg_2SiO_4[s] contributes a larger volume fraction when both materials are thermally stable due to its larger monomer volume. It is the most dominant material at pressures greater than ~500 mbar with grain volumes over 50%.

Overall, a complicated longitude, latitude and depth dependence of the cloud composition across the globe with the gas temperature playing a key role. The thermal instability of the silicate materials at the dayside upper atmosphere regions leads to large volumes of the dayside containing thermally stable, nm-sized TiO_2[s] seed particles. An equatorial belt of SiO_2[s] and SiO[s] forms due to the different thermo-chemical conditions between mid-latitudes and equatorial regions. Silicate materials such as SiO_2[s], $MgSiO_3$[s] and Mg_2SiO_4[s] are abundant at terminator regions ($\phi \sim 90°, 270°$) probed by transit spectroscopy.

4.5.4 Non-uniform element abundances

To complete our understanding of why certain mineral materials are thermally unstable at certain atmospheric regions, we look at the elemental abundances of elements involved in the cloud formation. The local element abundances determine the gas phase chemical composition which are used to determine the composition of the cloud particles. Several materials can be thermally stable at a particular T_{gas}-p_{gas}, meaning each of the condensing materials ($S > 1$)

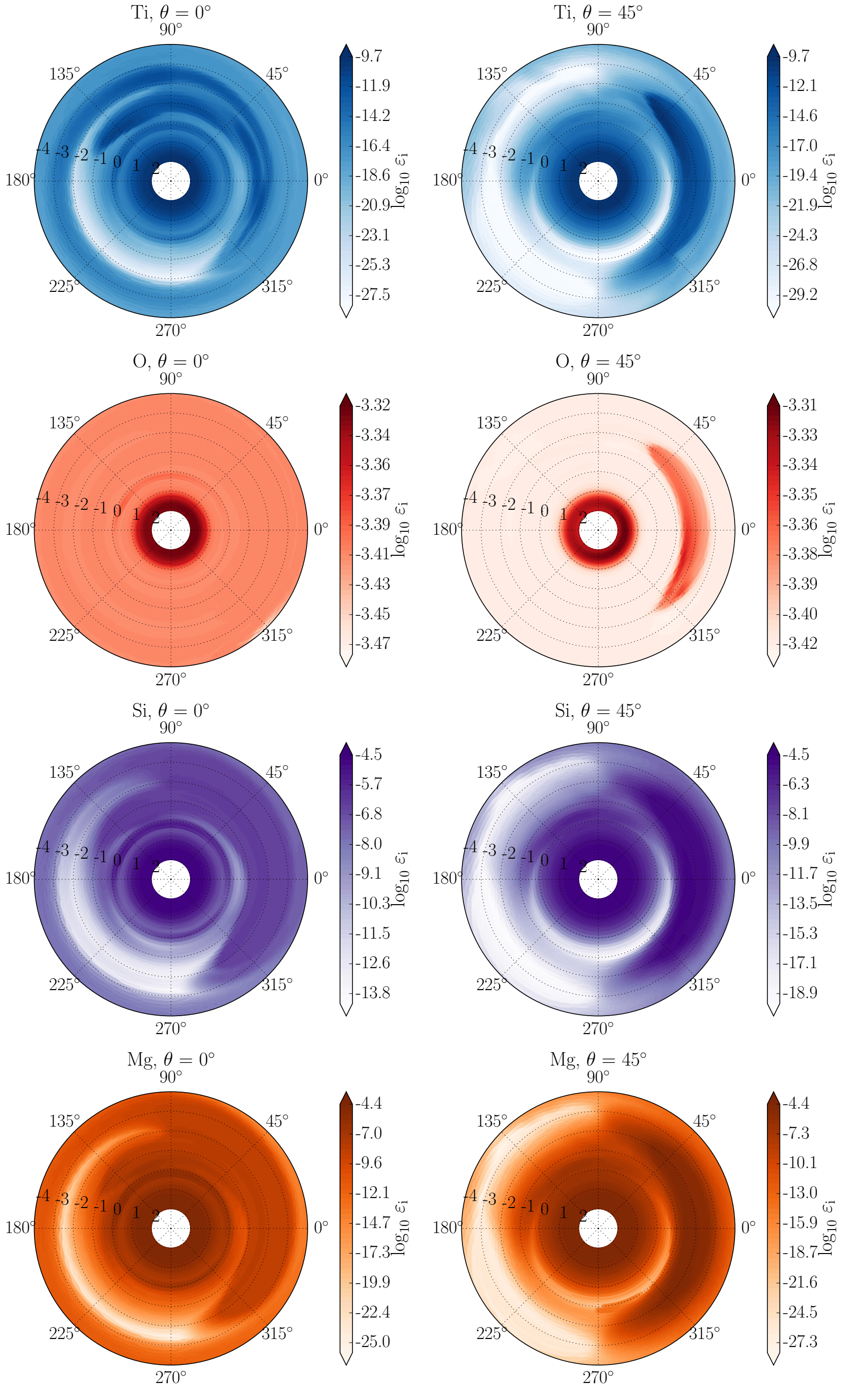

Figure 4.12: Meridional polar slices of gas phase element abundance $\log_{10}\varepsilon_i = n_i/n_{\langle H\rangle}$ (ratio i to Hydrogen abundance) of **Top:** Ti (blue), **Second row:** O (red), **Third row:** Si (purple) and **Fourth row:** Mg (orange/brown) at $\theta = 0°$ (left) and $\theta = 45°$ (right), respectively. For reference, solar metallicity $\log_{10}\varepsilon_i^0$ of the elements from Asplund et al. (2009) are, Ti: -7.05, O: -3.31, Si: -4.49, Mg: -4.40. Lighter coloured regions indicate a depletion of elements due to the cloud formation processes. Darker coloured regions indicate a local element abundance closer to the initial solar values. Outer circular values denote longitude at intervals of $\phi = 45°$ from the sub-stellar point ($\phi = 0°$). Radial values indicate $\log_{10}$ $\mathrm{p_{gas}}$ isobars from 0.1 mbar - 100 bar. The globe is irradiated from the direction of the colour bars. Note: the size of the annulus is not scaled to planetary radius.

must be considered when calculating the element depletion (Appendix B, Helling & Woitke, 2006). If one solid material has reached an equilibrium state ($S = 1$), this does not imply that all the constituent elements of the material have been condensed. If the initial abundance of elements in the gas phase is low for a particular element (e.g. Ti), then any changes in the elemental abundance due to the cloud formation processes will be greater compared to more abundant elements. Elements are depleted from the gas phase where cloud particle formation has occurred and are replenished where the material that the cloud particles are composed of has evaporated from the grain bulk. The 'evaporation window' of a material marks the atmospheric longitude (ϕ) location where a particular cloud particle material becomes thermally unstable. As cloud particles are transported towards this longitude by circulating gas, the elements from the unstable material replenishes the gas phase. More volatile materials evaporate further away from the sub-stellar point ($\phi = 0°$), while more thermally stable material evaporates closer to the sub-stellar point. Figure 4.12 shows meridional slices of the gaseous elemental abundance of Ti, O, Si and Mg at $\theta = 0°, 45°$. This shows where elements have been depleted in the atmosphere by the formation of cloud particles or replenished by the evaporation of thermally unstable materials.

Ti is typically depleted by 2-20 orders of magnitude depending on the location in the atmosphere. The highest abundance of gas phase Ti elements occurs at the dayside at $\sim$ 10mbar where Ti is replenished by the evaporation of $TiO_2[s]$ in these regions. Seed particles are not evaporated, however, indicating that the $TiO_2[s]$ seed particles remain thermally stable in these regions. The gas temperature is also too high to nucleate seed particles at these regions. The atmosphere never returns to solar metallicity values due to the thermal stability of the $TiO_2[s]$ seed particles throughout the 3D radial extent of the simulation boundaries. The evaporation window for $TiO_2[s]$ occurs at approximately $\phi = 315°$ longitude at 10 mbar. At $\theta = 0°$ the equatorial jet carries uncondensed gas towards the nightside where the local temperatures are low enough to allow an efficient surface growth of $TiO_2[s]$. The result is a decreasing Ti-element abundance by > 10 magnitudes on the nightside. The growth efficiency of $TiO_2[s]$ is less compared to other materials because less Ti is available to condense into $TiO_2[s]$ (compare Helling & Woitke 2006).

O, the most abundant element considered here, is depleted by a maximum of 30% throughout the atmosphere. Replenishment of oxygen at $\theta = 45°$, 10 mbar occurs due to the evaporation of O bearing silicate materials.

Si is the least depleted element on the nightside in comparison to Ti and Mg. Upper cooler atmospheric regions where SiO[s] is present tend to be less depleted. The depletion of Si at the equator, $\theta = 0°$, is from SiO_2[s] growth. The evaporation window for Si/O material is $\phi \approx 300°$ longitude at 10 mbar. Equatorial jets resupply the nightside with Si elements from evaporating dayside silicate materials.

Mg is typically more depleted on nightside regions indicating the efficient formation of Mg/Si-material. Gas containing Mg is transported to the nightside by the equatorial jet, where the lower temperatures allow the Mg/Si-material to be thermally stable. Severe depletion occurs at $\sim$1-10 mbar where Mg/Si-material surface growth occurs. The evaporation window for Mg/Si-material is $\phi \approx 280°$ longitude at 10 mbar.

Due to the global dynamics of the upper atmosphere, any replenished elements from evaporating material at mid-latitudes gets funnelled towards the equator. This hydrodynamic preference is how the mid-latitude, nightside regions contain some of the most element depleted areas of the globe with $>$10 orders of magnitude depletion. Si/O materials are also dominant at the equator due to these hydrodynamic motions, compared to Mg/Si despite both elements have similar initial solar abundances. At mid-latitude regions the efficient growth of Mg_2SiO_4[s] removes 1 Mg atom more from the gas phase compared to Si atoms for each Mg_2SiO_4[s] monomer condensed onto the cloud particle. The meridional motions then funnel gas from these mid-latitudes regions towards the equatorial jet, leading to a greater gaseous abundance of Si at the equator compared to Mg. This is seen in the different ranges of colour bar for Si and Mg in Fig. 4.12 where Si is typically more abundant by 5-10 magnitudes. The supersaturation ratio (Eq. 2.1) for SiO[s] and SiO_2[s] materials are therefore larger than Mg_2SiO_4[s] and $MgSiO_3$[s], since there are less gas phase Mg atoms to condense when grains are transported to the equator. Mg_2SiO_4[s] and $MgSiO_3$[s] constitute less of the the grain volume as the supersaturation of SiO[s] and SiO_2[s] increases in these regions while Mg_2SiO_4[s] and $MgSiO_3$[s] decreases. That is, Mg/Si material can become thermo-chemically unstable at equatorial regions while Si/O material remains stable. SiO[s] and SiO_2[s] are more efficient growth materials than Mg_2SiO_4[s] and $MgSiO_3$[s] at the equatorial thermo-chemical conditions and become the most dominant material compositions at the equator. Over time, this leads to an upper atmosphere equatorial band of SiO[s] and SiO_2[s]. A longitude, latitude and height inhomogeneous element abundance structure develops as the evaporation and growth windows are different for each species as they travel around the atmosphere.

In summary, the atmosphere is depleted of elements due to the cloud formation processes. Local regions of cloud material evaporation on the dayside replenish the gas phase of elements. Replenishment of the nightside of elements is governed through the equatorial jet, which transports un-condensed material from the dayside to the nightside. The gas phase elements are then depleted by growth of material at the cooler regions. A consequence of the dayside thermal instability and hydrodynamic transport of material is that the $\phi = 90^\circ$ terminator region is replenished in metallic elements while the $\phi = 270^\circ$ terminator is severely depleted. The atmosphere never returns to solar element abundances for those elements involved in cloud formation.

4.5.5 Summary of dynamic cloud formation results

The previous sections presented each of our cloud formation results individually. In this section, we examine the physics of our results as a whole and explain the cloud formation process on a global scale.

The nucleation of seed particles early in the simulation begins the cloud formation process. After a few minutes/hours of simulation, the rate of seed particle formation becomes negligible throughout the entire atmosphere due to the depletion of Ti elements from the gas phase. Meanwhile, cloud particles that grow $\gtrsim 1\,\mu$m begin to settle rapidly from the upper atmosphere to deeper layers (~ 1 bar), to their pressure supported levels. Settling of cloud particles results in a globally uniform cloud layer of maximum number density at ~ 1 bar. These settling grains deplete elements from the upper atmosphere. This leaves sub-micron cloud particles in the upper atmosphere from $\mathrm{p_{gas}} < 1$ bar. Cloud particles are transported by meridional gas motions towards the equatorial jet where the largest number density $\mathrm{n_d}$ of cloud particles can be found. Cloud particles then follow a circulation cycle as they are transported across the globe, dependent on the local temperature and element abundance conditions. This large scale cloud formation circulation cycle can be summarised as follows:

- As cloud particles are transported towards the night-day terminator ($\phi = 270^\circ$), the increase in gas temperature leads material to become thermally unstable. The most volatile material evaporates first, while the more stable material evaporates closer to the sub-stellar point ($\phi = 0^\circ$). $\mathrm{TiO_2}$ seed particles ($\sim 0.001\,\mu$m) remain thermally stable. The local gas phase is replenished in elements from the evaporating material.

- The equatorial jet transports the element replenished gas phase and the thermally stable seed particles (~ 0.001 μm) past the sub-stellar point ($\phi = 0°$) and to the $\phi = 90°$ day-night terminator. This replenishes the nightside regions near the day-night terminator of uncondensed elements.

- From longitudes $\phi =$ 90-180°; due to the colder nightside temperatures and the replenishment of gas phase elements and transport of seed particles from the equatorial jet, silicate material is thermally stable and condenses onto the seed particles. This depletes the gas phase of elements on the nightside. Due to this cloud formation, particles are $\sim$ 0.01-0.1 μm in these regions.

- Cloud particles remain thermally stable as they are transported through longitudes $\phi =$ 180-270°. The gas phase is severely depleted of elements but the cooler temperatures keep the cloud material thermally stable. The cloud particles are then transported to the night-day terminator ($\phi = 270°$) and the cloud formation cycle repeats.

A characteristic of this element cycle is that the amount of metallic elements returned to the gas phase by dayside grain evaporation is not enough to grow the grains to large sizes (> 1 μm) when they are thermally stable on the nightside. Over time, an upper atmosphere equatorial band of SiO_2[s] and SiO[s] rich grains develops due to greater number of uncondensed Si atoms available at the equator, while Mg atoms condense at higher latitudes.

4.6 Cloud/gas opacity and radiative effects of clouds

From Sect. 4.4.1 the temperature structure of the planet is affected by the presence of cloud particles. The cloud particles add an inhomogeneous opacity distribution to the atmosphere, altering the local radiation fields. A specific feature due to the presence of cloud particles is the equatorial regions temperature bump at $\sim$1 bar of $>$100 K. Figure 4.13 shows the cloud, gas and total opacity at the wavelength midpoints of the wavelength opacity bands in Showman et al. (2009), applied in this paper, at the sub-stellar point and $\phi = 0°$, $\theta = 45°$. Figure 4.13 also shows the parameterised cloud opacity used in Dobbs-Dixon & Agol (2013) (black dashed line),

$$\kappa_{\rm cloud}(\lambda) = \kappa_{\rm grey} + \kappa_{\rm RS}\left(\frac{\lambda}{0.9\mu m}\right)^{-4}, \tag{4.16}$$

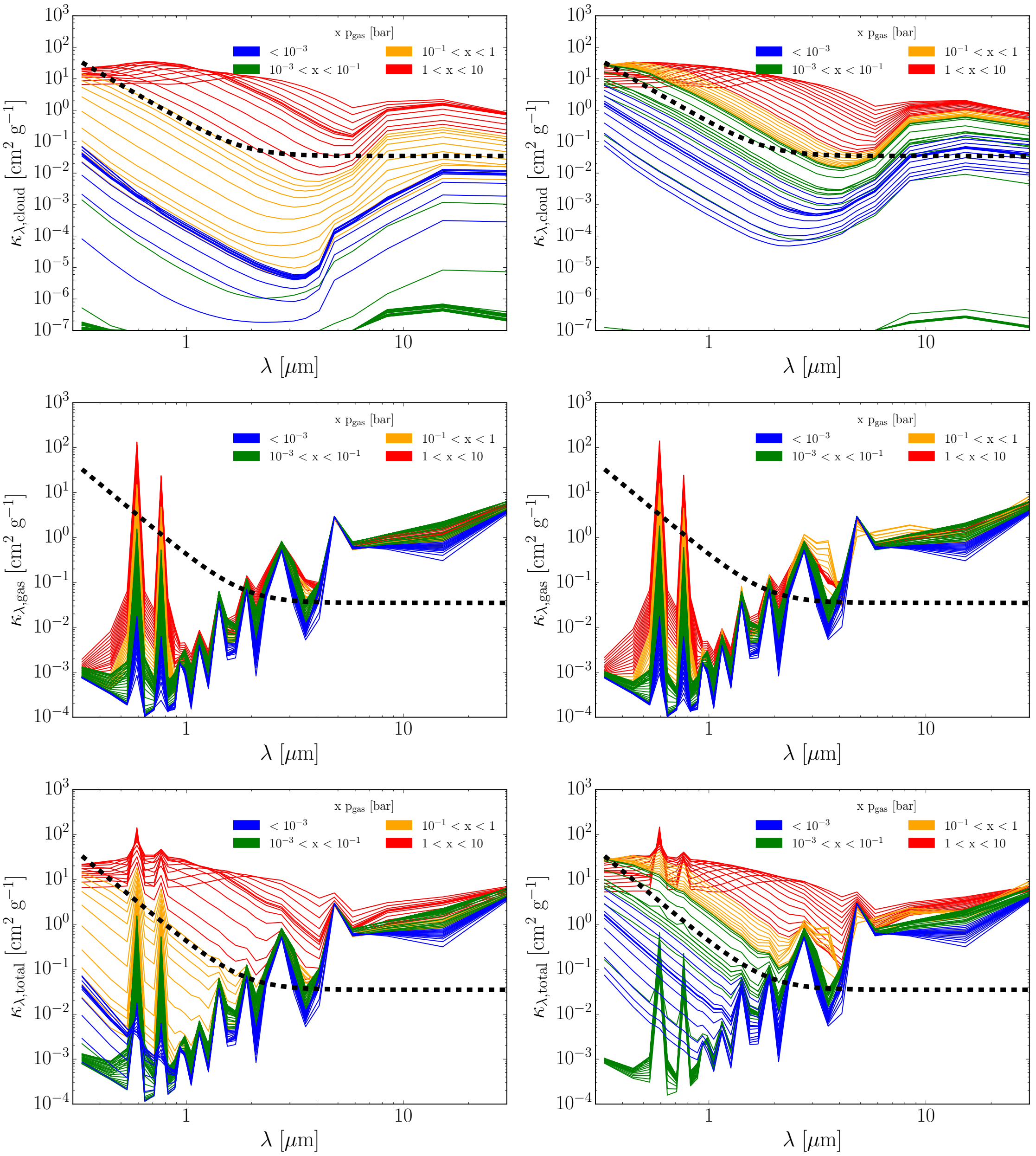

Figure 4.13: Cloud (top), gas (middle) and total (bottom) opacities at the sub-stellar point (left) and $\phi = 0°$, $\theta = 45°$ (right) at the centre of each of the wavelength bands used in the RHD radiative transfer scheme. The thick dashed line shows the parameterised cloud opacity used in Dobbs-Dixon & Agol (2013), Eq. (4.16). The addition of the the size and composition dependent cloud opacity results in a more inhomogeneous opacity structure.

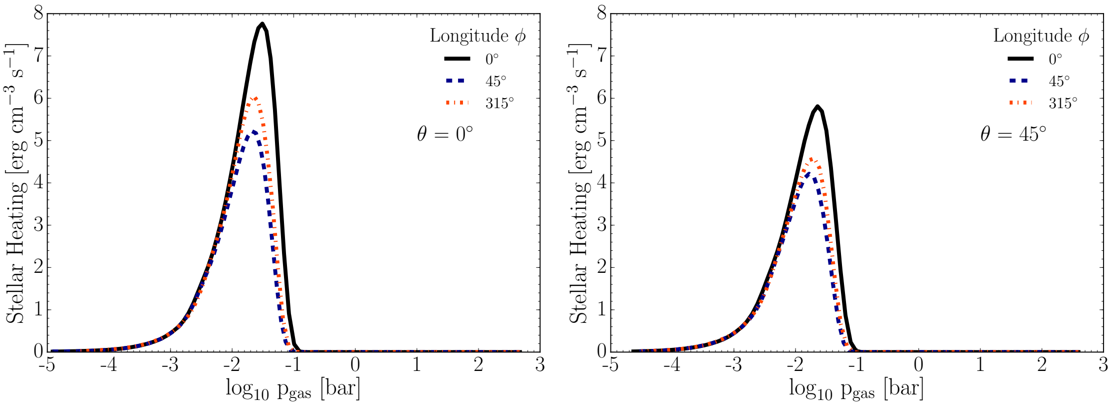

Figure 4.14: Stellar heating rate $S_\star$ [erg cm^{-3} s^{-1}] (Eq. 4.4) at the equator and $\theta = 45°$ latitude, $\phi = 0°, 45°, 315°$ longitude as a function of pressure. The heating rate steadily rises up to a maximum at ∼10 mbar corresponding to the highest temperature regions at the upper atmosphere. The heating rate drops off rapidly at 100 mbar.

where $\kappa_{\rm grey} = 0.035$ cm^2 g^{-1} and $\kappa_{\rm RS} = 0.6$ cm^2 g^{-1}. The size and composition dependent cloud opacity that results from the present simulations is typically lower than the Dobbs-Dixon & Agol (2013) opacity in the upper dayside atmosphere ($p_{\rm gas} < 1$ bar) but larger and greyer, i.e. less strongly wavelength dependent, at all wavelengths from $p_{\rm gas} > 1$.

Fig. 4.14 shows the stellar heating rate $S_\star$ (Eq. 4.4) at the sub-stellar point, $\theta = 45°$ at $\phi = 45°, 315°$ longitudes. The peak of energy deposition by stellar photons occurs at ∼10 mbar, where the highest dayside temperatures occur. The stellar energy deposition drops off rapidly at 100 mbar where some of the coolest dayside temperatures can be found. Compared to a self-consistent gas phase opacity simulation (Fig. 1, Tsai et al., 2014), the peak of stellar energy deposition is at the same pressure level ∼10 mbar. However, the peak of the heating at the sub-stellar point for the gas phase opacity simulation is ∼ 3 erg cm^{-3} s^{-1} less and there is a more gradual drop off in heating to ∼ 1 bar. The Tsai et al. (2014) simulation was found to be too cold when compared to the observations (Dobbs-Dixon & Agol, 2013). Our microphysical cloud structure maintains similar stellar heating regions seen in Dobbs-Dixon & Agol (2013), which suggests that a cloud opacity (parameterised or microphysical) pushes the stellar energy deposition further upward on the dayside atmosphere. The upper atmosphere gas temperature is typically cooler on the dayside and nightside with the microphysical cloud model compared to the parameterised cloud in Dobbs-Dixon & Agol (2013). This indicates that the lower cloud opacity in the microphysical model allows the gas to cool more efficiently in these regions than in the Dobbs-Dixon & Agol (2013) simulation.

Amundsen et al. (2014) suggest that the Planck averaged gas opacities used in the current study can lead to greater uncertainties in the stellar heating rate compared to other methods. The addition of cloud opacity may reduce this error by muting or washing out the rich molecular lines when the cloud opacity approaches the gas opacity, which can be seen in Fig. 4.13. However, in regions of low cloud opacity (e.g. seed particle regions) the results of Amundsen et al. (2014) suggest that the maximum of the stellar heating rate may occur in deeper atmospheric layers. We hypothesise that this would lead to a smaller or larger vertical extension of the seed particle region on the dayside, depending if this change decreased or increased the temperature at the seed particle region boundaries. Energy deposited at greater depth would be advected more efficiently in the vertical and horizontal directions, which may impact the overall trends of the cloud particles.

Since the stellar energy deposition is negligible at $p_{gas} > 100$ mbar, the $T_{gas} > 100$ K temperature bump seen at the equator (Fig. 4.3) cannot be due to stellar heating. A backwarming effect due to the presence of the opaque cloud base at ~ 1 bar occurs. This backwarming was not seen in Dobbs-Dixon & Agol (2013), suggesting that the increased cloud opacity in these regions (Fig. 4.13) is responsible for this feature. The gas irradiated by the host star at $\sim$10 mbar radiates with a Planck function B(λ, T) peak at $\lambda \sim$ 1-2 μm. This emitted radiation is then absorbed deeper in the atmosphere where the cloud opacity at $\sim$1 bar is largest at these infrared wavelengths, heating the local gas phase. The backwarming effect is not seen at mid-latitudes due to the larger grain sizes of the cloud at $p_{gas} < 1$ bar, producing larger infrared opacity (by up to 3 magnitudes) compared to the equator. The remitted infrared at mid-latitude regions is then absorbed closer to the temperature peak at 10 mbar, which results in a slightly flatter temperature inversion. Therefore, the 100-200 K temperature bump is not seen for mid-high latitude regions. Similar backwarming effects due to cloud particle and/or gaseous opacity have been investigated in previous studies (e.g. Helling et al., 2000; Tsuji, 2002; Burrows et al., 2006; Witte et al., 2009; Heng et al., 2012; Heng & Demory, 2013).

4.6.1 Comparison to 1D results

In this section we compare our 3D coupled model to our previous 1D post-processing, non-global approach in Chapter 3. In the current study we have investigated 5 cloud species (TiO_2[s], SiO[s], SiO_2[s], $MgSiO_3$[s], $MgSiO_4$[s]), neglecting 7 materials (Fe[s], FeO[s], FeS[s], Fe_2O_3[s], $CaTiO_3$[s], MgO[s], Al_2O_3[s]) which were included in previous modelling efforts

(Helling & Woitke, 2006; Helling et al., 2008b; Lee et al., 2015a; Helling et al., 2016a). Chapter 3 showed that some of the neglected species can have significant volume fractions in certain parts of the atmosphere. Al_2O_3[s] and $CaTiO_3$[s] were found to be thermally stable at regions of the hot dayside, this is likely to be the same in the 3D RHD case. This suggests that the grain sizes could be underestimated for these regions in the RHD model. However, Al_2O_3[s] and $CaTiO_3$[s] are typically not efficient growth species and are unlikely to grow the grain to significantly larger (> 0.01 μm) sizes. The addition of Fe[s] will affect the thermal stability of the cloud particles, grain sizes and drift velocity and therefore the local degree of element depletion, especially in the deeper regions where other species are less thermally stable compared to Fe[s]. A richer chemical composition can be expected when additional high-temperature condensates are included.

Chapter 3 generally reproduces the regions of efficient nucleation, growth and evaporation compared to the 3D RHD model, indicating that the chemical processes are accurately captured by the 1D models. The influence of dynamics on the specific cloud properties is large however, which leads to differences in predicted grain sizes between the two approaches. The time dependent settling of ~ 1 μm grains to their pressure supported regions near 1 bar results in a higher cloud opacity deeper in the atmosphere for the RHD model compared to the 1D models.

In more general terms, our 1D cloud simulations, DRIFT, are a valuable analysis tool because they are fast at providing a stationary solution to cloud properties with a substantial degree of chemical details. The 3D RHD simulations with our cloud formation module, are time-consuming but allows us to resolve the time and spacial evolution of a cloud-forming hot Jupiter atmosphere. At present, the time evolution of the current study has focused on the first 60 Earth days and the spacial resolution is limited to that of the RHD/GCM cells. Long-term studies which address the limitations of the current implementation are under development.

4.6.2 Limitations of the Current Model

We neglect possible condensation of more volatile material such as ZnS[s], KCl[s] and Na_2S[s]. These materials have been used for modelling cooler objects such as GJ 1214b (Charnay et al., 2015b) and T Brown Dwarfs (Morley et al., 2012), where the more stable species considered in this study are found deeper (below $\tau \sim 1$) in the atmosphere. However, if the atmosphere can efficiently mix solid/gas material upwards, we can expect the more stable condensates to also

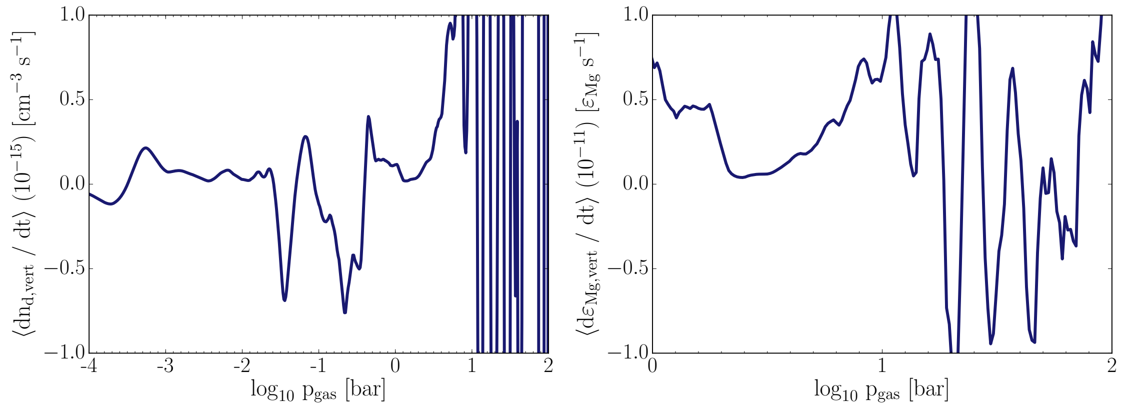

Figure 4.15: Snapshot horizontally and meridionally averaged iso-bars of the time dependent changes in n_d (left) and ε_{Mg} (right) due to the vertical advection. ε_{Mg} is given in the range 1 - 100 bar to avoid the skewing of the global averages by dayside particle evaporation in the upper atmosphere. Settling of grains by the drift velocity is taken into account for the n_d plot.

be present at high altitudes for these cooler objects. Sing et al. (2015) suggest that Na_2S[s] and KCl[s] condensation could be responsible for the sub-solar Na to K ratio observed on hot Jupiter WASP-31b (T_{eq} = 1575 K). SiO[s], the most volatile species in the current set-up, is only abundant at specific regions on the nightside which are thermo-chemically stable for it. The atmosphere is generally highly depleted (> 10 orders of magnitude less than solar) of the Ti, Si, Mg elements which take part in the cloud formation, however, longitude, latitude and depth differences in atomic abundance are present. From our model, the dayside-nightside terminator region is replenished of elements by the equatorial jet after material has evaporated at the hottest dayside regions. We suggest from the presented results, that Na_2S[s] and/or KCl[s] condensation could occur on the nightside and deplete Na/K on the nightside-dayside terminator boundary for both HD 189733b and WASP-31b. Even if Na_2S[s] and/or KCl[s] are a minor component of the total dust volume, the condensation of the materials can cause a large decrease in elemental abundance, as discussed in Helling et al. (2016a). The grains would evaporate their Na/K content once they travel to the dayside which would replenish the Na/K atomic abundance for the dayside-nightside terminator. Additionally, the different thermo-chemical kinetics of Na_2S[s] and KCl[s] could lead to latitudinal variance, similar to our equatorial band of Si/O and mid-latitude Mg/Si material dominated regions.

As noted in Mayne et al. (2014), for most GCM/RHD modelling of hot Jupiters, the deep atmosphere ($p \gtrsim 1$ bar) takes longer to reach a steady state due to the slow (t > 1200 days) momentum exchange between the lower and upper layers. There is evidence from Fig. 4.1 that the velocity structure is still evolving slowly at these deep regions from the effect of the cloud opacity. Due to the added cost of the microphysical cloud model, the effect of the upper and lower atmospheric cloud opacity on the dynamics of deeper regions may take many more months or years of simulation, beyond the scope of this early investigation.

The mixing of replenished gas material upward from the deeper depths ($\sim$ 100 bar) where cloud particles evaporate their volatile contents is also expected to occur on the momentum exchange timescales suggested by Mayne et al. (2014); as it is this timescale where the information of the gaseous elemental content is exchanged between the deep and upper atmosphere. The replenishment rate over 1 scale height can be approximated by the mixing timescale $\tau_{\rm mix}$ at these depths. In Chapter 3 we estimated that the mixing timescale would be on the order of $\tau_{\rm mix} \sim 10^8$ s at $\sim$ 100 bar. The replenishment rate for Mg abundances at these depths can be estimated from $\varepsilon^0_{\rm Mg}$ by $\tau_{\rm mix}$, $\varepsilon^0_{\rm Mg}$ / $\tau_{\rm mix} \approx 4 \cdot 10^{-13}$ $\varepsilon_{\rm Mg}$ s^{-1}; $\varepsilon^0_{\rm Mg} = 10^{-4.4}$ and $\tau_{\rm mix} = 10^8$ s. This value would be many times smaller as the mixing material travels several atmospheric scale heights before reaching the upper atmosphere. Agúndez et al. (2014) suggest that the mixing timescale may be on the order $\tau_{\rm mix} \sim 10^9$ s at these depths for HD 189733b, calculated from the GCM mixing tracing method of Parmentier et al. (2013). To illustrate this point, Fig. 4.15 shows snapshots of the horizontal and meridional mean dn$_{\rm d}$ / dt and d$\varepsilon_{\rm Mg}$ / dt due to vertical advection at gas pressure iso-bars. The small magnitudes of these changes compared to the absolute values suggest that vertical advection may not significantly alter upper atmosphere cloud particle results during the epoch of the simulation discussed here. Longer integration times (>1000 days) will be required to better understand the effect of deeper mixing of gas phase elements and the settling of smaller particles. However, the results of Parmentier et al. (2013) suggest, for HD 209458b, that sub-micron sized cloud particles may remain present in the upper atmospheric (> 1 bar) layers over longer timescales. Overall, this is in contrast to more convective atmospheres, e.g. Brown Dwarfs, where $\tau_{\rm mix}$ is estimated to be $\sim$ 300 s at $\sim$ 10 bar (Woitke & Helling, 2004), which increases the resupply rate of elements to the upper atmosphere.

4.7 Summary and conclusions

We have developed a 3D kinetic cloud formation module for exoplanet RHD/GCM simulations. Through our coupled RHD and cloud model we have shown that HD 189733b has extremely favourable thermodynamic and hydrodynamic conditions for efficient cloud formation and growth. We lend weight to previous interpretations of observations of a thick mineral cloud component containing sub-micron sized particles in the upper atmosphere. The interplay between the hydrodynamical motions and the cloud formation produces an inhomogeneous opacity structure which has effects on the global atmospheric conditions. A summary of key results include:

- Grain sizes are sub-micron at atmospheric pressures and terminator regions probed by transmission spectroscopy.
- Silicate materials are thermally stable in regions probed by transmission spectroscopy.
- Grain sizes, number density and opacity of cloud particles are non uniform across the globe with significant differences in longitude, latitude and depth.
- Due to the global elemental depletion from cloud formation, the equatorial regions are dominated by $SiO[s]$ and $SiO_2[s]$ while mid-upper latitudes mostly contain $MgSiO_3[s]$ and $Mg_2SiO_4[s]$.
- Hydrodynamic motions primarily govern the global distribution of cloud particles, transporting cloud particles towards nightside equatorial regions.
- The existence of the clouds as well as the particle sizes and material mixes are the result of the kinetic cloud formation processes.
- The atmosphere is severely depleted ($\geq$10 orders of magnitude) of elements Ti, Si, Mg used in the cloud formation theory while O is only depleted by $\sim$30 %.
- Mid-high latitude nightside regions are not efficiently replenished in elements and contain the most reduced gas phase elemental abundances.
- Thermally unstable materials on the dayside replenish elements to the gas phase; these uncondensed elements are then transported to the nightside via the equatorial jet.
- Maximum thermal stability of the cloud particles are found at the coolest parts of the nightside inside the large scale vortex regions.

We improve on previous 1D approaches by developing an atmospheric RHD model consistently coupled to cloud formation model of with self consistent opacity feedback, element mixing and cloud particle transport and settling. We emphasise that we do not rely on any mixing parameterisation of gaseous /solid material (e.g. by use of K_{zz}), assumptions about the grain sizes or particle size distributions. Through this early study, we have demonstrated that our kinetic cloud formation model is well suited to be applied to 3D hydrodynamic studies of exoplanet atmospheres. However, long-term studies are required to address the limitations of the current implementation of the cloud module. Potential future applications of our model are 3D Brown Dwarf atmosphere simulations such as those in Showman & Kaspi (2013); Zhang & Showman (2014). The model can be extended for warm-Neptune studies with the addition of more volatile cloud species such as ZnS[s], KCl[s] and Na_2S[s] to the chemical scheme.

5

Monte Carlo Radiative-Transfer for Exoplanet Atmospheres

5.1 Introduction

Radiative transfer theory and modelling is a cornerstone of any astronomical discipline [1], since the astrophysical evidence on the properties of an object of is the detection and subsequent interpretation of photons emanating from that object. The field of exoplanet science is no different, with radiative-transfer modelling required for large scale atmospheric simulations, post-processing of results and simulating synthetic observational data.

For RHD/GCM modelling and post-processing of results, the majority of studies use various configurations of the 'two stream approximation' (e.g. Toon et al., 1989; Marley & McKay, 1999; Fortney et al., 2006). The RHD model outlined in Chapter 4 also applies a two stream scheme to calculate stellar heating rates and atmospheric radiative transfer.

---

[1] bar the recent detection of gravitational waves

For post-processing simulated data, the most sophisticated two stream models use ingoing and outgoing streams at numerous trajectories in the planetary in the atmosphere which include a prescription of the scattering of light by cloud particles (e.g. Cahoy et al., 2010; Webber et al., 2015). Using 1D atmospheric model data, the results of the two stream model are then integrated across the 3D sphere using Gaussian quadrature to calculate the total flux escaping in a particular direction. These two stream approaches are inherently one dimensional in their approach, requiring careful placement of streams inside the computational zone. In many schemes, streams are calculated in vertical columns, with streams not able to interact in the horizontal directions. Hence, many models do not consider the transfer of energy between atmospheric columns, or assume horizontal energy transport to be negligible or second order. Much of the small scale inhomogeneity of the atmosphere can be lost from the use of 1D input data and 1D radiative transfer streams.

Another method of modelling radiative transfer in 3D media is Monte Carlo radiative transfer [MCRT], which is a microphysical, stochastic approach to solving radiative transport problems. The method simulates the random walk of a luminosity packet (henceforth ‘L-packet’ or ‘packet’) through a medium and describes the interactions (scattering, absorption) of the packet with the surrounding medium by probabilistic sampling. This is different from numerically solving the radiative transfer equation via the two-stream approximation or ray-tracing method (e.g. Rijkhorst et al., 2006; Dobbs-Dixon & Agol, 2013). Since MCRT tracks the random walk of a packet and its interactions, radiative transfer through complicated 3D geometries, inhomogeneous opacities, and highly multiple scattering regions can be modelled. The true 3D, and sub-grid nature of MCRT means that the small scale inhomogeneity of the atmosphere can be captured.

Monte Carlo radiative-transfer has a long history in the modelling of astrophysical objects. MCRT methods have been extensively used to investigate radiative transfer in dusty media, for example, protoplanetary disks (e.g. Whitney et al., 2003; Harries et al., 2004; Pinte et al., 2006; Min et al., 2009), the ISM (e.g. Robitaille, 2011), AGB star winds (e.g. Woitke & Niccolini, 2005) and dusty galactic scale problems (e.g. Wood & Loeb, 2000). MCRT has also been applied to the study and retrieval of Earth based cloud properties (e.g. Mayer, 2009; Stap et al., 2016).

The heavily irradiated, inhomogeneous opacity, and thermal structures of cloud forming hot Jupiter atmospheres is an ideal application for a MCRT approach. Modelling the effects of cloud particles on observable properties of exoplanets using MCRT techniques began with Seager et al. (2000), which mainly focused on producing phase and polarised light curves from a model atmosphere. Hood et al. (2008) applied a parameterised cloud model to a 3D idealised atmosphere of HD 209458b and modelled scattered light curves and geometric albedos of varying cloud heights and scattering properties. de Kok & Stam (2012) used a 3D Monte Carlo scattering code to investigate the influence of forward scattering particles on transit spectroscopy. Garcia Munoz & Isaak (2015) used a Pre-conditioned Backward Monte Carlo method to constrain the cloud particle scattering properties of Kepler-7b. Recently, Monte Carlo transport methods have also been used to model the path and decay of cosmic rays through a Jupiter-like atmosphere (Helling et al., 2016b), important to the ion chemistry in exoplanet atmospheres (Rimmer & Helling, 2016).

Whitney (2011) and Steinacker et al. (2013) provide a review of MCRT theory and modelling for astrophysical based applications. Mayer (2009) reviews the method for Earth based applications, with particular emphasis on remote sensing of water vapour clouds.

5.2 Monte Carlo Radiative-Transfer Theory

In MCRT, each initialised packet carries a luminosity fraction ϵ_0 / Δt [erg s^{-1}], proportional to a source (e.g. parent star or planetary atmosphere) of luminosity L_{source} [erg s^{-1}]. If N L-packets are initialised by the source of luminosity, the luminosity carried per packet is then (e.g. Lucy, 1999)

$$\frac{\epsilon_0}{\Delta t} = \frac{L_{\mathrm{source}}}{N}, \tag{5.1}$$

where Δt [s] is the time over which the MCRT experiment is performed; usually $\Delta t = 1$ s for time independent MCRT such as the current study. By tracking the proportion of the luminosity of each L-packet that escapes during the simulation in a certain direction, the total luminosity escaping towards a particular observation direction can be found by summing up the contribution of each L-packet to the total escaping luminosity. If the total luminosity budget in the simulation is normalised to the source luminosity (i.e. $L_{source} = 1$), the total contribution of all packets is then the fraction (i.e. $f_{tot} \in (0, 1)$) of source luminosity that escaped the simulation boundaries. To retrieve the luminosity that escaped, the source luminosity is calculated and multiplied by the fraction of luminosity that escaped carried by the L-packets.

The beginning of the packet tracking process starts by stochastically assigning initial starting coordinates and direction of a given packet, depending on the location of the luminosity source that is emitting the packet. For example, a stellar L-packet is initialised randomly at the top of the atmosphere on the dayside of the HD 189733b computational grid in our model. The wavelength-dependent luminosity carried by these stellar packets is the total monochromatic luminosity incident on the atmosphere, divided by the number of simulated packets ($\epsilon_{0,\mathrm{inc}}$ / Δt = $\mathrm{L}_{\mathrm{inc},\lambda}$ / $\mathrm{N}_{\mathrm{inc}}$). The L-packets emitted from the atmosphere itself are assigned a random starting position within a computational cell volume, where the luminosity is proportional to the total monochromatic luminosity of the atmosphere ($\epsilon_{0,\mathrm{atm}}$ / Δt = $\mathrm{L}_{\mathrm{atm},\lambda}$ / $\mathrm{N}_{\mathrm{atm}}$). Initialised stellar packets are assumed to travel in a plane-parallel direction towards the planet, while atmospheric, thermally emitted packets are given an isotropic initial direction. The random walk of the L-packet is then determined by stochastically sampling probability distributions that govern the behaviour of the packet (distance travelled, scattering directions etc.).

From the Beer-Lambert law in radiative transfer theory, the probability of a photon packet passing, without interaction, through a medium of total optical depth τ_λ is given by

$$P(\tau_\lambda) = \mathrm{e}^{-\tau_\lambda}, \tag{5.2}$$

where the optical depth τ_λ is defined as

$$\tau_\lambda = \int_0^{l_{\max}} \rho_{\mathrm{gas}}(l)\kappa_{\mathrm{ext,total}}(\lambda, l)\mathrm{d}l, \tag{5.3}$$

where ρ_{gas} [g cm^{-3}] is the local gas density, $\kappa_{\mathrm{ext,total}}$ [cm^2 g^{-1}] the local total extinction opacity, including absorption and scattering, and l [cm] the path length. The probability of a packet interacting with the surrounding medium is then

$$P(\tau_\lambda) = 1 - \mathrm{e}^{-\tau_\lambda}. \tag{5.4}$$

The MCRT method stochastically samples this probability distribution with the use of a (pseudo) random number, P(τ_λ) = $\zeta \in [0,1]$. An optical depth, determined stochastically, encountered by the packet before an interaction is given by

$$\tau_\lambda = -\ln(1-\zeta). \tag{5.5}$$

Using the definition of τ_λ (Eq. 5.3), the distance that the packet travelled through the simulation can then be computed should the density and extinction opacity in the path of the packet be known. After the packet has travelled the distance given by the sampled τ_λ, an interaction with the surrounding medium occurs.

5.2.1 L-packet interactions with dust and gas

Once the coordinates specified by the optical depth sampling and direction of travel have been reached by the packet, a scattering or absorption event is determined stochastically. In cloud forming hot Jupiter atmospheres, the packet interacts with two components: the gas and cloud particles. An interacting packet exhibits different scattering and absorption behaviours depending what component it is interacting with. The local probability of the packet interacting with the gas phase $P_{\rm gas}$ is given by

$$P_{\rm gas} = \frac{\kappa_{\rm ext,gas}}{\kappa_{\rm ext,cloud} + \kappa_{\rm ext,gas}}, \tag{5.6}$$

where $\kappa_{\rm ext,gas}$ [cm^2 g^{-1}] is the total opacity of the gas and $\kappa_{\rm ext,cloud}$ [cm^2 g^{-1}] the total opacity of the cloud component. Should $\zeta_1 < {\rm P}_{\rm gas}$, (where the indexed random number (e.g. ζ_1,ζ_2) denotes a sequence of random, independent, numbers for a particular scheme) the packet is assumed to interact with the gas phase. The type of interaction, scattering or absorption is determined by sampling the single scattering albedo $\omega_{\rm gas}$ of the gas phase, which is the probability of the packet undergoing a scattering interaction. Since we only consider a H_2 scattering gas component n the MCRT scheme (Sect. 3.3), the local single scattering albedo of the gas $\omega_{\rm gas}$ is given by

$$\omega_{\rm gas} = \frac{\kappa_{\rm sca,H_2}}{\kappa_{\rm gas,ext}}, \tag{5.7}$$

where $\kappa_{\rm sca,H_2}$ [cm^2 g^{-1}] is the scattering opacity of H_2 and $\kappa_{\rm gas,ext} = \kappa_{\rm gas,abs} + \kappa_{\rm sca,H_2}$ [cm^2 g^{-1}] the total extinction for the gas component. Should $\zeta_2 < \omega_{\rm gas}$ the packet is Rayleigh scattered by H_2, otherwise it is absorbed by the gas phase.

If the interaction is with the cloud component (i.e. $\zeta_1 > P_{\rm gas}$), the type of interaction is given by sampling the local cloud particle single scattering albedo $\omega_{\rm cloud}$. Should $\zeta_3 < \omega_{\rm cloud}$ the packet is assumed to be scattered by the cloud component towards a new direction, otherwise it is absorbed by the cloud particles.

After each scattering event, the next interaction location is determined by Eq. (5.5) and the sampling process is repeated. It is important to note that packets can undergo multiple scattering interactions before getting absorbed, especially in high ($\omega_{\rm gas/cloud} > 0.9$) single scattering albedo regions.

5.2.2 Scattering of L-packets by dust and gas

During a scattering event, a new direction of travel is given to the packet, which is dependent on the geometric and compositional properties of the interacting material as well as the wavelength of the interacting packet. A key quantity to consider when modelling a scattering event is the size parameter of the scattering particle given by $x = 2\pi a/\lambda$, where a [cm] is the particle size and λ [cm] the wavelength of the L-packet. The scattering behaviour of an interacting packet can be split into two categories:

1. x $\ll$ 1 - Rayleigh scattering,

2. x $\gtrsim$ 1 - Mie scattering.

For Rayleigh scattering, the particle size is orders of magnitude smaller than the wavelength of light interacting with it, resulting in the well-known double lobed scattering phase function where the probability of scattering in the forward and backward directions are equal. In the Mie regime, the particle size and wavelength of light are of similar magnitudes; the light is typically more forward scattering with a small backscattered component at optical wavelengths. For a scattered packet in MCRT, the new travel direction is generated stochastically from the scattering properties of the interacting material. This is determined by sampling the (normalised) scattering phase function $\Phi_{\rm scat}(\theta, \phi)$ of the interacting scattering particle, which is the probability of scattering towards angle (θ, ϕ).

For small cloud particles with small size parameters x $\ll$ 1 and H_2 gas particle scattering, we apply the Rayleigh scattering phase function given by

$$\Phi_{\rm RS}(\theta, \phi) = \frac{3}{16\pi}(1 + \cos^2\theta). \tag{5.8}$$

The θ scattering direction is sampled randomly from this distribution, where a rejection method is applied following the advice in Whitney (2011). The ϕ scattering angle angle is given by

$$\phi = 2\pi\zeta, \tag{5.9}$$

which is a uniform sampling of the ϕ direction across the 2π radian circular circumference. Rayleigh scattering events are wavelength independent and assumed to be elastic.

When a packet scatters off a cloud particle with size parameter $x \gtrsim 1$, the Henyey-Greenstein [HG] scattering phase function (Henyey & Greenstein, 1941) can be applied. The HG phase function is an analytic approximation to the Mie scattering phase function, given by

$$\Phi_{\rm HG}(g_\lambda, \theta, \phi) = \frac{1}{4\pi}\frac{1 - g_\lambda^2}{[1 + g_\lambda^2 - 2g_\lambda\cos\theta]^{3/2}}, \tag{5.10}$$

where g_λ is the wavelength-dependent scattering asymmetry parameter in the range -1 to 1, given by the results of the Mie theory. This is defined as the mean scattering cosine angle from the relation

$$g_\lambda = \langle\cos\theta\rangle = \int_\Omega \Phi_{\rm HG}(g_\lambda, \theta)\cos\theta d\Omega. \tag{5.11}$$

A value of $g < 0$ indicates a preference for packet backscattering, $g = 0$ an equal backward/forward scattering and $g > 0$ forward scattering. The scattering angle $\cos\theta$ is sampled stochastically from this distribution using the following form

$$\cos\theta = \frac{1}{2g_\lambda}\left[1 + g_\lambda^2 - \left(\frac{1 - g_\lambda^2}{1 - g_\lambda + 2g_\lambda\zeta}\right)^2\right]. \tag{5.12}$$

The sampled ϕ direction is given by Eq. (5.9). We assume elastic scattering for Mie scattering events. The HG probability distribution has been shown to be a reasonable approximation to Mie scattering within the optical and near-IR wavelength regime (Draine, 2003). However, a small but not insignificant probability of backscattering is not completely captured by this approximation at optical wavelengths (e.g. Kattawar, 1975; Draine, 2003; Hood et al., 2008; Dyudina et al., 2016). To address this, we apply a Two-term Henyey-Greenstein [TTHG] function (e.g. Pfeiffer & Chapman, 2008; Cahoy et al., 2010; Dyudina et al., 2016) given by

$$\Phi_{\rm TTHG}(g_a, g_b, \theta) = \alpha\Phi_{\rm HG}(g_a, \theta) + \beta\Phi_{\rm HG}(g_b, \theta), \tag{5.13}$$

where α is the mainly forward scattering component with $g_a > 0$, and β a mainly backscattering component with $g_b < 0$. For all parameters, the relation $\alpha + \beta = 1$ has to be satisfied. We apply the parameters in Cahoy et al. (2010) where $g_a = g_\lambda$, g_b = -$g_\lambda/2$ and $\alpha = 1$ - g_b^2, $\beta = g_b^2$. The TTHG form is commonly used in various atmospheric radiative transfer scattering codes (e.g. Marley et al. 1999; Cahoy et al. 2010; Barstow et al. 2014; Garcia Munoz & Isaak 2015; Dyudina et al. 2016) and more qualitatively captures the Mie backscattering lobe at optical wavelengths.

To determine the scattering angle of a TTHG event, the probability of forward scattering is simply given by $\zeta < \alpha$ (Pfeiffer & Chapman, 2008) after which Eq. (5.12) with $g_\lambda = g_a$ can be used, otherwise the scattering is a backscattering event in which $g_\lambda = g_b$ is applied. Although α and β are used to determine a forward or backward scattering event, due to the probabilistic sampling of the HG function scattering angle, sampling the α term does not necessarily always result in a forward scattering event, nor β a backward scattered event.

Since there is a distribution of cloud particle sizes in each cell, the size of an individual cloud particle interacting with the packet must be stochastically determined from the size distribution properties. This is required as the size distribution may contain a combination of cloud particles in the Rayleigh and Mie size parameter regimes, resulting in a mixture of packet scattering behaviour. To capture this scattering behaviour, we perform a stochastic sampling from the cumulative distribution function [CDF] of the size distribution, which is the fractional contribution of each particle size to the total area of the particle ensemble. The area distribution is used, rather than the size distribution, as this better captures the contribution of each cloud particle radius to the scattering cross-sectional opacity of the size distribution (since $\kappa_{\rm sca} \propto f(a)a^2$). The cloud particle mean grain size, $\langle a \rangle$ [cm], and mean grain area, $\langle A \rangle$ [cm^2], of the cloud particles in each RHD cell can be found from the dust moment values, L_j (Woitke & Helling, 2003, 2004), Chapter 3. Assuming an arithmetic log-normal distribution of cloud particle sizes (e.g. Ackerman & Marley 2001), the mean μ and standard deviation σ (more specifically their natural logarithms) of the ensemble of particles in each cell is then calculated (e.g. Stark et al., 2015). The surface area log-normal distribution is given by (e.g. Heintzenberg, 1994)

$$A(a) = \frac{A_0}{a\sigma_A\sqrt{2\pi}} \exp\left[-\frac{(\ln(a) - \mu_A)^2}{2\sigma_A^2}\right] \tag{5.14}$$

which is the log-normal size distribution multiplied by the surface area $4\pi a^2$, with the total area $A_0 = 4\pi n_\mathrm{d} \exp(2\mu + 2\sigma^2)$ (e.g. Zender, 2015), where a [cm] is the sampled grain size, n_d [cm^{-3}] the total cloud particle number density, μ_A the arithmetic mean of the area distribution and σ_A the standard deviation of the area distribution. The relation between the mean and standard deviation of the size distribution (μ, σ) and area distribution (μ_A, σ_A) are given by (e.g. Heintzenberg, 1994)

$$\mu_A = \mu + 2\sigma^2,$$

$$\sigma_A = \sigma. \tag{5.15}$$

The cloud particle area cumulative distribution function of the log-normal size distribution $A_\mathrm{CDF} \in (0,1)$ is then constructed in each cell from (e.g. Zender, 2015)

$$A_\mathrm{CDF}(a) = \frac{1}{2} + \frac{1}{2}\,\mathrm{erf}\left[\frac{\ln(a) - \mu_A}{\sqrt{2}\sigma_A}\right], \tag{5.16}$$

where erf is the error function. We construct A_CDF for 100 log-spaced cloud particle size a bins between a minimum seed particle size $a_\mathrm{seed} \sim 0.001$ μm and a maximum of $a_\mathrm{max} = 10 \cdot a_\mathrm{eff}$ μm, where a_eff is the effective cloud particle radius (Eq. 2.30). During the simulation, by sampling a random number $\zeta \in (0,1)$, the particle size from the distribution interacting with the packet can therefore be stochastically determined by sampling A_CDF (i.e. $\zeta \rightarrow a$).

We assume two scattering regime limits in our model for a certain cloud particle size parameter ($x = 2\pi a/\lambda$). For $x < 0.1$ we assume a Rayleigh scattering event, while if $x \geq 0.1$ we assume a TTHG scattering event. We assume TTHG scattering events to occur at the properties of the effective mean radius values (e.g. $g_\lambda(a_\mathrm{eff})$). The effect of this scheme is that if the mean and variance skew the area distribution towards larger cloud particle sizes, then the fractional contribution of particle areas, where $x \geq 0.1$ increases, and so the probability of a TTHG event is increased. However, if the distribution is skewed towards smaller cloud particle sizes then a greater fraction of cloud particle area satisfies $x < 0.1$, increasing the likelihood of a Rayleigh event.

5.2.3 MCRT variance reduction techniques

In a basic MCRT scheme, to produce observable quantities for a particular observation direction, the MCRT code would track how many packets of a particular luminosity entered the simulation and how many escaped. The ratio of these values would then give the fraction

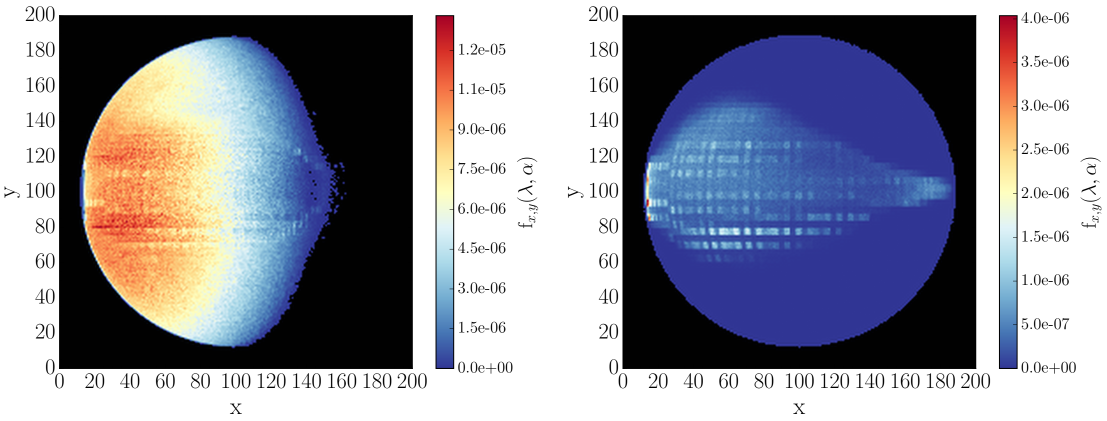

Figure 5.1: Incident scattered (left) and atmospheric emitted (right) light image array of the L-packet luminosity fractions $f_{x,y}(\lambda, \alpha) \in (0,1)$ escaping from the HD 189733b simulation. These images are produced by the next event estimator method at 1.0 μm for a viewing angle/phase of $\alpha = 60°$ (eastern dayside). The sharp transition from blue to black at pixel numbers x = 120—150 is the eastern terminator in the scattered light image, including a 'twilight' effect where packets scatter past the terminator line. The effect of the grid structure on the images is more apparent in the emitted light, since packets are initialised from within the cell volumes.

of luminosity escaping the simulation domain towards a particular direction. However, the probability of an individual packet escaping by chance towards a particular direction can be incredibly small, depending on the geometric properties of the simulation, and can produce noisy results if not enough Monte Carlo packets are simulated (e.g. see Dupree & Fraley, 2002). Therefore, variance reduction techniques were developed for MCRT, which allows for a much improved signal to noise and greater computational efficiency than the basic scheme. We employ three techniques in this study as follows: next event estimation, survival biasing, and composite emission biasing. The variance and convergence properties our model output is presented in Sect. 5.4.5.

Next event estimation

Next event estimation (e.g. Yusef-Zadeh et al., 1984; Wood & Reynolds, 1999) is a variance reduction method that uses a ray-tracing technique in conjunction with the Monte Carlo scheme. At every scattering or emission event, a fraction of the packet's luminosity, $W_{\rm po}\epsilon_0$, (Eq. 5.1) is peeled off towards an observation direction using a ray-tracing method. The fraction of luminosity is given by the normalised phase function of the type of interaction, weighted by the probability of the packet escaping the simulation towards this observation direction. The peeled off luminosity is wavelength dependent and the luminosity carried by the packet is not altered in the peeling off scheme. The peeled off luminosity is then stored in a 2D pixel image array at this observation direction, which can be used to derive observational quantities.

Multiple pixel images can be constructed for many viewing angles and wavelengths, which allows a single photon packet interaction to contribute to multiple output images at different planetary phases. Since every packet now contributes to the output images, this improves the signal to noise of the output as images can be produced without relying on packets emerging by chance from the simulation boundaries towards the observer. Figure 5.1 illustrates the resultant next event estimator scattered stellar (left) and atmospheric emitted (right) luminosity fractions at 1.0 μm for a viewing angle of $\phi = 60°$, $\theta = 0°$.

For atmospheric emission, assumed to be isotropic, the fraction of the packet luminosity peeled off towards observation direction α is given by

$$W_{\mathrm{po}}(\alpha) = \frac{1}{4\pi} \mathrm{e}^{-\tau_2}, \tag{5.17}$$

where $1/4\pi$ is the normalisation factor for isotropic emission into 4π steradians and $\tau_2(\lambda)$ (where indexed τ terms (e.g. τ_1,τ_2 etc.) indicate optical depths calculated using the ray-tracing method to the simulation boundaries, and non-indexed τ denotes the stochastically sampled optical depth for photon packets) the optical depth through the computational zone at wavelength λ, towards the observational direction.

For non-isotropic scattering events such as Rayleigh or Henyey-Greenstein scattering, the fraction of peeled off luminosity is related to the probability of the packet scattering towards the observational direction. For Rayleigh scattering, the weight of peeled off luminosity is given by

$$W_{\mathrm{po}}(\alpha) = \Phi_{\mathrm{RS}}(\alpha) \mathrm{e}^{-\tau_2}, \tag{5.18}$$

and for Two-term Henyey-Greenstein,

$$W_{\mathrm{po}}(\alpha) = \Phi_{\mathrm{TTHG}}(g_a, g_b, \alpha) \mathrm{e}^{-\tau_2}. \tag{5.19}$$

Phase curve information can be calculated by adding the contribution of each event to an image in the desired observation direction (e.g.. 360° in longitude). Each weight is added into a square image pixel array of (x, y) = (201, 201) pixels and then normalised by the number of initialised packets after the simulation is complete. The luminosity scattered/emitted in the observational direction can then be found by multiplying the fraction of escaping luminosity by the total luminosity of the emitting source.

Survival biasing

For diffuse emission from within the simulation boundaries, the packet is forced to scatter at each interaction and not terminated upon absorption (see Sect. 3.3). In order to conserve energy, the weight of the luminosity carried by the packet is reduced at each interaction by the single scattering albedo

$$W_{\rm new} = \omega W, \tag{5.20}$$

where, in an interaction with the gas phase, $\omega = \omega_{\rm gas}$ and with the cloud particles $\omega = \omega_{\rm cloud}$. The fraction of luminosity lost by the photon packet due to absorption is then taken into account in the peeled off images as the packet interacts with the surrounding medium. So that a packet does not scatter indefinitely with ever decreasing weight, a Russian Roulette scheme (e.g. Dupree & Fraley, 2002) is applied to stochastically terminate packets below a predefined weight cut-off. The packet is then given a 1 in 10 chance of surviving, with the new weight of the surviving packets $\mathrm{W}_{\rm new} = 10 \cdot \mathrm{W}$. In our model, packets with weight $\mathrm{W} < 10^{-3}$ are entered into the Russian Roulette scheme.

Composite emission biasing

For hot Jupiter atmospheres, the total dayside emission luminosity can be orders of magnitude greater than the emission from the nightside of the planet. In non-biased MCRT, the number of packets $N_{i,\lambda}$ emitted from cell i is given by the fraction of the luminosity of the cell to the total luminosity of the atmospheric cells at this wavelength (e.g. Pinte et al., 2006),

$$N_{i,\lambda} = \frac{L_{i,\lambda}}{\sum_i L_{i,\lambda}} N_{\rm atm}, \tag{5.21}$$

where $L_{i,\lambda}$ is the luminosity of the cell, $\sum_i L_{i,\lambda}$ the total luminosity of the considered cells, and $N_{\rm atm}$ the total number of atmospheric L-packets emitted at wavelength λ. Low luminosity regions (e.g.. the nightside), where $L_{i,\lambda} \ll \sum_i L_{i,\lambda}$ can therefore be under sampled in the emission scheme, which increases the variance of results derived from these regions.

To address this, we implement the multiple component, emission composite biasing method from Baes et al. (2016), where a linear combination of the unbiased emission (Eq. 5.21) probability distribution function and a uniform (in cell number) distribution function is applied.

This results in the number of emitted packets per cell given by

$$N_{i,\lambda} = N_{\text{atm}} \left[(1-\eta) \frac{L_{i,\lambda}}{\sum_i L_{i,\lambda}} + \frac{\eta}{\sum_i i_\lambda} \right], \tag{5.22}$$

where $\eta \in (0,1)$, is a parameter governing the linear combination and $\sum_i i_\lambda$ the total number emitting cells at wavelength λ. To conserve the total luminosity, each emitted packet is given a cell dependent starting weight of

$$W_{\text{em}} = \frac{1}{(1-\eta) + \eta \langle L_{i,\lambda} \rangle / L_{i,\lambda}}, \tag{5.23}$$

where

$$\langle L_{i,\lambda} \rangle = \frac{\sum_i L_{i,\lambda}}{\sum_i i_\lambda}, \tag{5.24}$$

is the average cell luminosity at wavelength λ. We apply a fixed $\eta = 0.5$ throughout our simulations. Baes et al. (2016) provide an in depth description of this composite emission biasing method.

Forced First Scattering

L-packets emitted or incident in optically thin regions ($\tau < 1$) of the atmosphere can escape the simulation boundaries without contributing (apart from their initial emission event) their luminosity fractions to the next event estimator images. To address this, the forced first scattering method can be employed for MCRT simulations (e.g. Cashwell & Everett, 1959; Mattila, 1970; Wood & Reynolds, 1999), where the packet is forced to scatter at least once before continuing its random walk. After an isotropic emission direction is given, the optical depth τ_1 towards the edge of the simulation is calculated. The packet is then randomly scattered at a corresponding distance less than τ_1 given by

$$\tau_\lambda = -\ln\left[1 - \zeta(1 - \mathrm{e}^{-\tau_1})\right] \tag{5.25}$$

Packets initially emitted in the direction towards the centre of the planet are exempt from the scheme, as they are likely to interact with the atmosphere before exiting or terminating. The weight for the packets after a forced first scattering event is

$$W_{\text{fs}} = \omega(1 - \mathrm{e}^{-\tau_1}) \tag{5.26}$$

where ω is the gas or cloud particle single scattering albedo at the scattering coordinates. The reduced weight packet luminosity fraction at the first scattering location is then peeled off using the next event estimator scheme and a new travel direction sampled.

5.2.4 Noise Error in MCRT

Because of the stochastic nature of MCRT, it exhibits Poisson sampling statistics, where the noise error σ is given by

$$\sigma = \frac{1}{\sqrt{N_{\rm im}}}, \tag{5.27}$$

where $N_{\rm im}(\lambda, \alpha)$ is the number of photon packets contributing to the output image, dependent on the wavelength and viewing angle.

For weighted MCRT, the use biasing techniques, the above relation is not strictly true for integrated quantities derived from the MCRT method which are not 'fair detectors' of photon packets. However, for imaging post-processing the $1 / \sqrt{N}$ relation is a suitable guide for estimating the noise errors.

5.3 Relation to Observable Quantities

Since MCRT works in units of fractions of luminosity, to produce synthetic observable quantities the definition of the quantity of interest must be expressed in terms of luminosity, or rather fractions of escaping luminosity. In the following sections we detail how simulating each quantity is approached and how the code units outputted by the MCRT scheme relate to observational quantities.

5.3.1 Scattered light phase curves and albedo spectra

To produce scattered light phase curves, we track the random walks of stellar L-packets incident on the HD 189733b simulated atmosphere. The stellar illumination is assumed to be plane parallel from the direction of the host star, with the initial latitude and longitude (ϕ, θ) top of atmosphere positions determined stochastically from a rejection method, carried out across the circular annulus of the dayside face of the planet. In this mode, should the packet be absorbed by the gas or cloud particles, it is terminated and no longer contributes to the simulation. The survival biasing variance reduction technique is not required in this mode since the majority of incident stellar packets are scattered or absorbed in the atmosphere. Therefore, the fractional

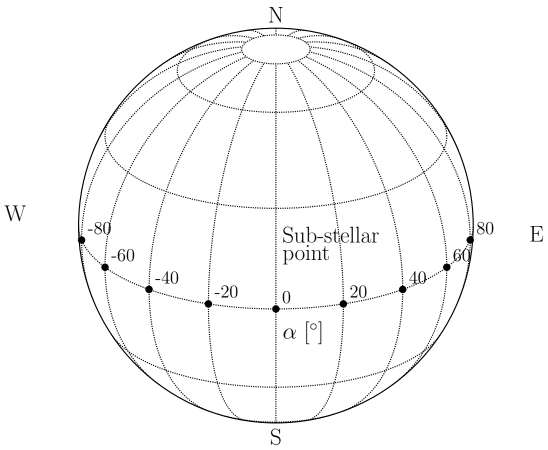

Figure 5.2: Diagram visualising the definition of equatorial viewing angle α [°] used in this study. Viewing angles east of the sub-stellar point are positively defined, while regions west of the sub-stellar point are negatively defined.

weight of the packet luminosity remains unchanged in this mode (W = 1). We chose a viewing angle of $\theta = 0°$ latitude (equator) while altering the longitude viewing angle α to capture planetary phase information. We define $\alpha = 0°$ as the viewing angle at the sub-stellar point (i.e. full phase) with $+°$ α eastward and $-°$ α westward from the sub-stellar point. Figure 5.2 shows a schematic visualisation of this α definition. As a consequence, we ignore possible viewing effects of non-negligible transit impact parameters, similar to other post-processing RHD/GCM methods (e.g. Fortney et al., 2006; Showman et al., 2009; Amundsen et al., 2016).

The total fraction of luminosity, carried by the photon packets, escaping towards viewing angle α at wavelength λ is given by summing the image pixel array produced by the peeling off method (Sect. 5.2.3, Fig. 5.1)

$$f_{\rm total}(\lambda, \alpha) = \sum_{x,y} f_{x,y}(\lambda, \alpha), \tag{5.28}$$

where $f_{\rm total}$ is the total fraction of luminosity escaping towards viewing angle α at wavelength λ and $f_{x,y}$ is the fraction of luminosity contained in a (x,y) pixel image array. The monochromatic phase dependent albedo $\mathrm{A}_\lambda(\alpha)$ is defined as

$$A_\lambda(\alpha) = \frac{f_{total}(\lambda, \alpha) L_{inc}(\lambda)}{L_{inc}(\lambda)} = f_{total}(\lambda, \alpha), \tag{5.29}$$

where L_{inc} [erg s^{-1}] is the incident luminosity onto the dayside face of the exoplanet atmosphere from the host star. The monochromatic apparent geometric albedo $\mathrm{A}_{g,\lambda}$ is defined as the fraction of scattered light at zero phase angle ($\alpha = 0°$) to an equivalent spherical Lambertain surface (e.g. Seager, 2010; Madhusudhan & Burrows, 2012). In the MCRT scheme $A_{g,\lambda}$ is derived from the luminosity fractions by the equation

$$A_{g,\lambda} = \frac{f_{total}(\lambda, \alpha = 0^o) L_{inc}(\lambda)}{f_{Lambert} L_{inc}(\lambda)} = \frac{f_{total}(\lambda, \alpha = 0^o)}{2/3}, \tag{5.30}$$

where $f_{Lambert} = 2/3$ is the scattering fraction of the theoretical Lambertian planet at zero phase.

The wavelength-dependent classical phase function (e.g. Seager, 2010; Madhusudhan & Burrows, 2012) can be constructed from the scattering fractions

$$\Phi_\lambda(\alpha) = \frac{f_{\rm total}(\lambda, \alpha)}{f_{\rm total}(\lambda, \alpha = 0^o)}, \tag{5.31}$$

which is the ratio of reflected luminosity at viewing angle α compared to the fraction reflected at $\alpha = 0°$. The monochromatic planetary luminosity due to reflected starlight $L_{\rm p,scat,\lambda}$ [erg s^{-1} cm^{-1}] as a function of viewing angle is given by

$$L_{\rm p,scat,\lambda}(\alpha) = f_{\rm total}(\lambda, \alpha) L_{\star,\lambda} \left(\frac{R_p^2}{4a^2} \right), \tag{5.32}$$

where R_p is the radius of the planet and a the semi-major axis. The monochromatic luminosity of the star is given by

$$L_{\star,\lambda} = 4\pi^2 R_\star^2 B_\lambda(T_{\star,\rm eff}, \lambda), \tag{5.33}$$

where $R_\star$ is the radius of the star and B_λ the Planck function, which is dependent on the stellar effective temperature $T_{\star,\rm eff}$. To ensure good signal to noise, we emit the same number of packets ($N_{\rm inc} = 10^7$) for each (pseudo) monochromatic wavelength.

5.3.2 Emitted light phase curves and spectra

We follow a similar scheme to the protoplanetary disk and ISM MCRT based studies of Pinte et al. (2006) and Robitaille (2011) where the monochromatic luminosity $L_{i,\lambda}$ [erg s^{-1} cm^{-1}] of computational cell i is

$$L_{i,\lambda} = 4\pi \rho_{i,gas} V_i (\kappa_{i,\lambda,abs,cloud} + \kappa_{i,\lambda,abs,gas}) B_\lambda(T_i), \tag{5.34}$$

where V_i is the volume of the cell, $\rho_{i,gas}$ the gas density, $\kappa_{i,\lambda,abs,cloud}$ the cloud absorption opacity, $\kappa_{i,\lambda,abs,gas}$ the gas absorption opacity, and $B_{i,\lambda}$ the Planck function, which is dependent on the cell temperature T_i.

In this scheme the packets are not terminated upon absorption but are forced to scatter with reduction in their weight at each event. Survival biasing and Russian Roulette techniques are therefore applied (Sect. 5.2.3). Composite emission biasing is also applied to decrease the noise error of results derived from nightside regions (Sect. 5.2.3). We employ a wavelength-dependent *dark zone* (Pinte et al., 2006) of longitude- and latitude-dependent, radially integrated optical depth $\tau_{r,\lambda}(\theta,\phi) = 30$ (Eq. 5.3). No packets are emitted from these regions and packets are terminated if they cross into regions deeper in the atmosphere than the cell radial index given by this condition. This prevents tracking packets through low luminosity weight regions which contribute negligibly to the photospheric emission. The contribution of cells below this depth to the total cell emission luminosity is also ignored (i.e. $L_{i,\lambda} = 0$). The emitted monochromatic luminosity $\mathrm{L}_{\mathrm{p,em},\lambda}$ [erg s^{-1} cm^{-1}] from the planet at viewing angle α is then given by

$$L_{\mathrm{p,em},\lambda}(\alpha) = f_{\mathrm{total}}(\lambda,\alpha)\sum_i L_{i,\lambda}. \tag{5.35}$$

As in the scattered light case, we assume the same number of packets ($\mathrm{N}_{\mathrm{atm}} = 10^8$) for each (pseudo) monochromatic wavelength.

5.3.3 Transit Spectroscopy

The calculation of a model transit spectrum using MCRT is different to albedo calculations, since in transit spectroscopy, we are interested in the total amount of luminosity *absorbed* at a particular impact parameter b from the planetary annulus.

The radius ratio of the planet to host star is proportional to the difference in flux in and out of transit from a photometric light curve. However, planets with an atmosphere will have a wavelength dependent annulus radius, which adds an additional component to the 'solid' annulus (usually taken to be a solid surface, or in the case of hot Jupiter exoplanets a deep atmospheric layer (~10-100 bar) subtended by the planet. This additional 'radius' from the opacity of the atmosphere can be thought of as the impact parameter b where the chord transmitted through the atmosphere is approximately where $\tau = 1$. In practice, for post-processing

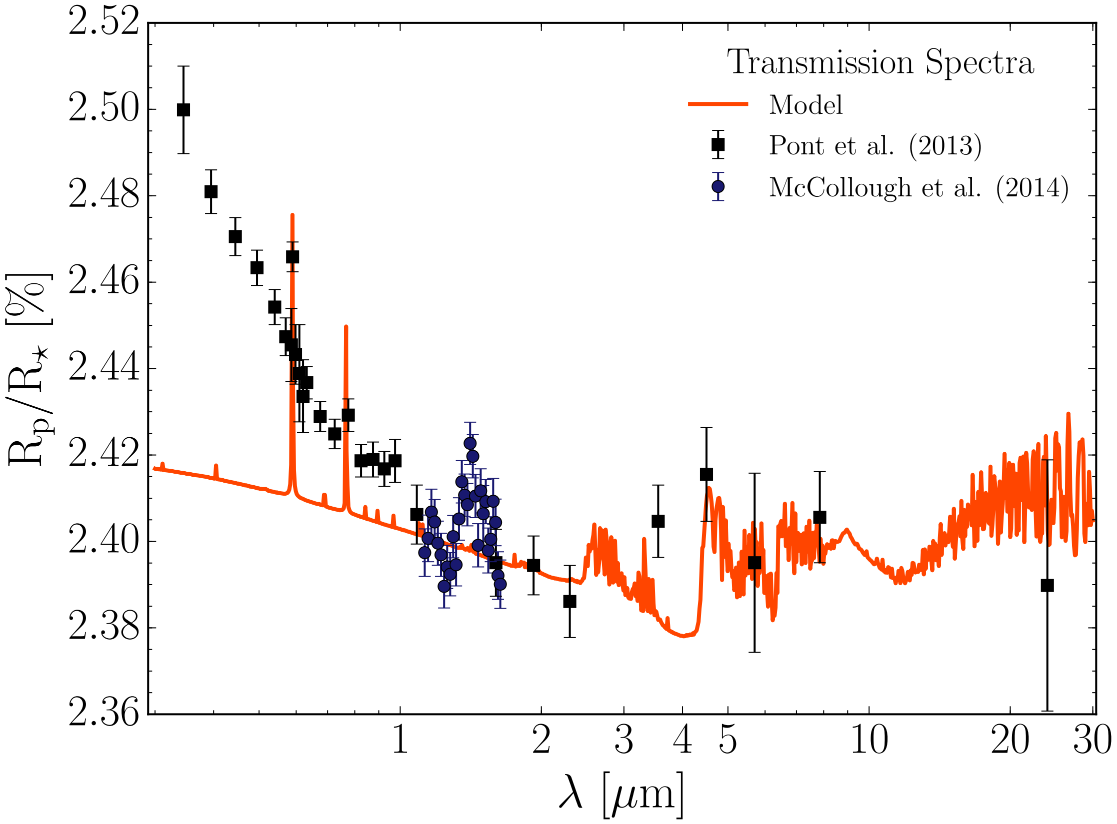

Figure 5.3: Transmission spectra post-processing of the HD 189733b simulation using the MCRT method. The model output is compared to the data from Pont et al. (2013) (HST STIS, Spitzer) and McCullough et al. (2014) (HST WFC3).

atmospheric models, an average or effective radius is calculated by integrating the transmission as function of impact parameter.

This is calculated from (e.g. Dobbs-Dixon & Agol, 2013)

$$\frac{\Delta F}{F\star} = \frac{1}{\pi R_\star^2}\left[R_p^2 + \int_0^\infty (1 - \mathrm{e}^{-\tau_\lambda(\mathrm{b})})\mathrm{bdbd}\alpha\right], \tag{5.36}$$

where R_p is the solid radius of the exoplanet, $\tau(b)$ the optical depth at impact parameter b and α the observed polar angle during transit. For a simulation grid structure, such as in most GCM models, this expression becomes (e.g. Robinson, 2017)

$$\frac{\Delta F}{F\star} = \frac{1}{R_\star^2}\left[R_p^2 + 2\sum_{i=1}^{N_b}(1 - \mathrm{e}^{-\tau_{\mathrm{i},\lambda}})\mathrm{b_i}\Delta\mathrm{b_i}\right], \tag{5.37}$$

where N_b is the number of radial cells and i the i^{th} radial cell and Δb_i the thickness of the radial cell i. The MCRT model then must track the wavelength dependent τ_λ emergent at each impact parameter along the circular annulus of the simulated atmosphere. Fortunately, in practice this is simple in the current MCRT set up, thanks to the variance reduction methods described in the section above, which we detail below.

Stellar packets are spawned randomly on the dayside of the planet in the transit annulus (rather than across the whole planetary disk) and the impact parameter index calculated, via a ray tracing routine the τ_λ can then be calculated at that impact parameter. This gives an initial optical depth through the transit chord at an initial impact parameter, which is added to the total τ_λ counter. So far, the technique is similar to absorption only ray tracing methods of calculating transit spectra (e.g. Fortney et al., 2010; Dobbs-Dixon & Agol, 2013). To accommodate multiple scattering, packets are then free to propagate though the atmosphere, interacting (scattering, absorption) with the surrounding medium as in the usual MCRT scheme. The next event estimator, forced first scattering and survival biasing methods are applied to increase the efficiency. The next event estimator is used to track the optical depth contribution of each photon packet at each scattering event to the transit chord at a specific impact parameter. The weighted optical depth and impact parameter are tracked and added to the individual packets contribution to the transmission through each impact parameter.

The average optical depth contribution from the ensemble of packets at each impact parameter is then

$$\bar{\tau}_i = \frac{\sum \tau_i}{N_{ph}}, \tag{5.38}$$

which then can be used in Eq. 5.37 to calculate the effective radius. Figure 5.3 shows the transit spectra of our HD 189733b simulation from the MCRT code, compared to available observational data from Pont et al. (2013) and McCullough et al. (2014). It is clear that although the model is a consistent fit with the infra-red data, the optical slope produced by the model contains a large discrepancy. This may be due to the effect of unresolved starspots on HD 189733A, which is known to be an active star. The effect of star spots on transmission spectrum is to increase the optical slope (McCullough et al., 2014), mimicking the effects a Rayleigh scattering cloud coverage.

5.4 Post-Processing of HD 189733b RHD data

In this section, we present the scattered and emitted light results of our MCRT post-processing method. We chose 36 different viewing angles to capture orbital phase information of the scattered and emitted light, which gives a phase resolution of $\Delta\alpha = 10^{\circ}$. Sections 5.4.1 and 5.4.2 present our incident scattered light apparent geometric albedo A_g, and albedo spectra/phase curves, respectively. Section 5.4.3 presents our atmospheric emitted luminosity spectra and phase curves. In Sect. 5.4.4 we combine our scattered and emitted light results and compare these combined results with current observations; we also predict Kepler, TESS and CHEOPS photometric observations for HD 189733b. Finally, in Sect. 5.4.5 we discuss the variance and convergence properties of our MCRT model results.

5.4.1 Geometric albedo

Figure 5.4 shows the resultant geometric albedo of our post-processed cloud forming HD 189733b 3D RHD model, which we compare to the HST STIS observations of Evans et al. (2013). Our results in the B band are consistent with the individual STIS data points, but underestimate the convolved B Band geometric albedo. Our results are also consistent with the Wiktorowicz et al. (2015) ground based B+V band polarimetry measurement of an upper limit of $A_{g,\lambda} < 0.4$. Our V Band result compares poorer to the observations, however it is clear that Na absorption is responsible for the downward trend near 0.6 μm. This is perhaps

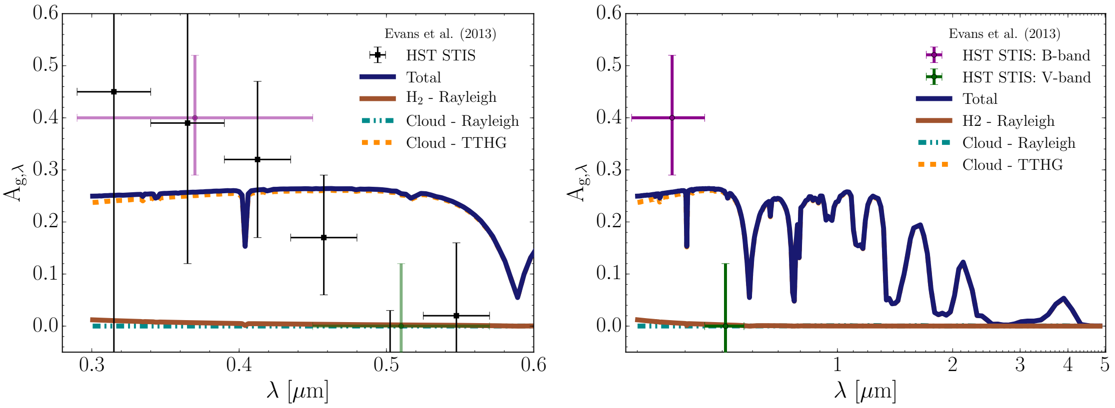

Figure 5.4: Scattered light apparent geometric albedo $A_{g,\lambda}$ (Eq. 5.30) of our HD 189733b simulation output compared to Evans et al. (2013)'s individual HST STIS measurements. The total contribution is indicated by the solid blue line; TTHG cloud particle scattering by the dashed orange line; Rayleigh cloud particle scattering by the teal dash-dotted line; H_2 Rayleigh scattering by the brown solid line. Left: (0.29-0.6 μm) The Rayleigh & TTHG model is generally consistent with the B Band HST STIS measurements, but does not predict the low albedo of the V band. Right: (0.29-5 μm) Extended spectra from 0.3-5 μm, showing the convolved B Band and V band measurements from Evans et al. (2013). $A_{g,\lambda}$ becomes negligible beyond 5 μm.

because of the presence of an unknown absorbing material in the V band (Evans et al., 2013; Barstow et al., 2014).

Figure 5.4 also shows the individual contributions from H_2 Rayleigh scattering, cloud particle Rayleigh scattering, and cloud particle TTHG scattering to the total fractions. The TTHG scattering contributes the greatest fraction to the total geometric albedo across all wavelengths. A small H_2 Rayleigh scattering component is also present at shorter optical wavelengths.

5.4.2 Scattered light phase curves

During a single orbit of HD 189733b around its parent star, different atmospheric regions come in and out of view of the detector, dependent on the planetary phase being observed. If eastward and westward hemispheres of the dayside atmospheric properties are different, an asymmetric signal as a function of phase (α) is expected to be observed. In order to extract this phase behaviour from our 3D RHD results, we produce observables at various viewing angles (longitude from the sub-stellar point) α during the Monte Carlo simulation.

Figure 5.5 shows the albedo $A_{\lambda}(\alpha)$ spectra (Eq. 5.29) as a function of phase. Slight differences in the fraction of scattered light between the regions east and west of the sub-stellar point are present, due to the differences in the east-west 3D cloud properties in our HD 189733b RHD model. The greatest difference in A_{λ} (Δ A_{λ} = 0.005) in the B and V bands between the east and west hemispheres occur between viewing angles of $\sim 80°$ and $100°$. This corresponds to the east and west day-night terminator regions, respectively, which have the largest differences in cloud properties. For example, the eastern terminator generally has mean particles sizes $\langle a \rangle \sim 0.01$ μm, composed of a mix of Si-O materials and TiO_2. While the western terminator $\langle a \rangle \sim 0.1$ μm with larger volume fractions of $MgSiO_3$[s] and Mg_2SiO_4[s] (Chapter 4). Wavelengths > 5 μm show little or no scattering behaviour, as the single scattering albedo for both gas and cloud components become negligible.

Figure 5.6 (left) presents the albedo $A_\lambda(\alpha)$ (Eq. 5.29) phase curves at 25 different wavelengths in the range considered in the MCRT post-processing. Optical and some near-IR wavelengths show scattering fractions $A_\lambda(\alpha) > 0.1$ across $-90° \ldots 90°$ viewing angles. This suggests that a significant percentage of the planet's optical scattered luminosity remains observable, while a majority of the dayside hemisphere remains in view. Scattered light fractions drop below 10% for $\lambda > 3$ μm.

Figure 5.6 (right) shows the classical scattered light phase function $\Phi_\lambda(\alpha)$ (Eq. 5.31). This adds emphasis to any asymmetric scattering behaviour as a function of phase. Optical and near-IR wavelengths 0.3-1μm show very symmetric scattering phase curves around the sub-stellar point, while longer 1-5μm can show asymmetry in their scattering properties. Longer IR wavelengths can also show westward offsets of 10-20°, depending on wavelength. This is due to larger cloud particles residing on the western hemisphere of the dayside (Paper I), increasing the opacity and scattering probability of IR packets travelling in these regions.

We compare our classical phase function to the Lambertian phase function (Fig. 5.6, dashed black line), which is the phase function of a theoretical, perfectly isotropic scattering sphere (e.g. Seager, 2010; Madhusudhan & Burrows, 2012). This is useful for interpreting the type of scattering behaviour at east and west dayside hemispheres (Madhusudhan & Burrows, 2012). The eastern hemisphere shows a classical phase function behaviour typical of Rayleigh-like scattering across all wavelengths, suggesting that the majority of optical and near-IR packets undergo a single scattering event in these regions. This region contains the smallest cloud particle sizes in the RHD simulation and lowest cloud opacity, increasing the likelihood of the packet escaping the boundaries without further interaction. The western hemisphere shows a mix of isotropic and Rayleigh-like scattering classical phase function behaviour for optical, near-IR and IR wavelengths. This suggests that packets experience multiple scattering events, which results in packets escaping in an isotropic manner. These regions contain some of the

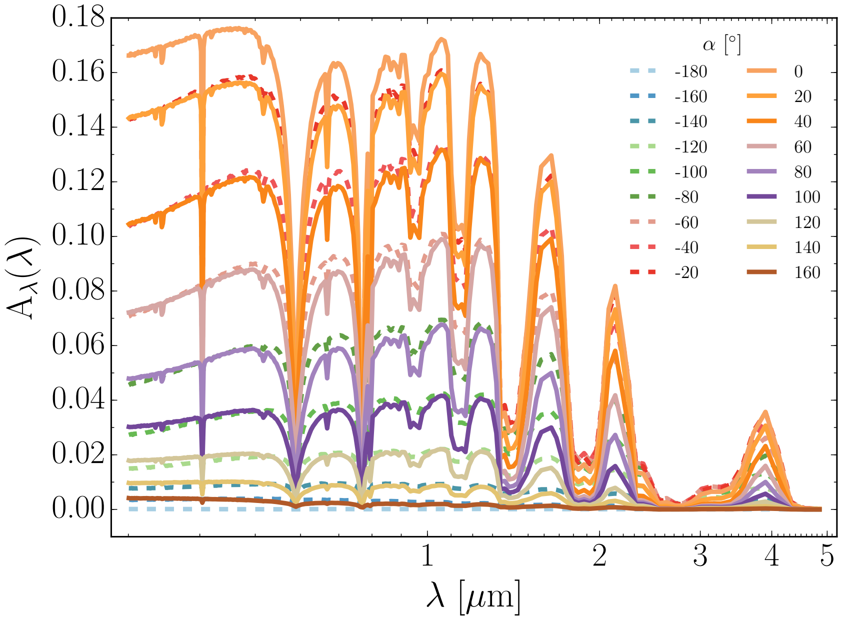

Figure 5.5: Scattered light albedo spectra $A_\lambda(\alpha)$ (Eq. 5.29) as a function of wavelength at several viewing angles α, where $\alpha = 0°$ defines the sub-stellar point. Differences in the 3D cloud structure on the east and west hemispheres from the sub-stellar points produce small variations in A_λ across the 360° phase space at optical wavelengths. Na and K absorption are responsible for the drops in A_λ in the optical, while H_2O features are the main absorber at near-IR to IR wavelengths.

larger cloud particles on the dayside and an increased cloud scattering probability.

Figure 5.6 (right) also shows IR (3-5 μm) classical phase function asymmetry that arises from the differences in the opacity structure between the two day-night terminator regions. The westward limb ($\alpha = -90°$) contains larger cloud particle sizes, opacity, and scattering probability in the IR compared to the eastern limb ($\alpha = 90°$). The behaviour of the IR wavelength classical phase functions suggests that packets do not interact with the eastern terminator cloud structures and pass through without interaction, are absorbed, or interact with cloud particles on the nightside hemisphere since there is a return to the Lambertian function at nightside viewing angles. For the westward limb, the IR cloud opacity is higher, packets travel shallower into the atmosphere before interacting and are more likely to be scattered. These differences in cloud structures between the terminator regions result in a skewing of the IR classical phase function. The western side of the planet is therefore typically brighter in the IR by 10-20% in scattered light than the eastern side at comparable phases.

5.4.3 Emitted light spectra and phase curves

At secondary transit, observations are also sensitive to the thermal emission from the planetary atmosphere itself. Because the star-planet contrast is larger at IR wavelengths than in the

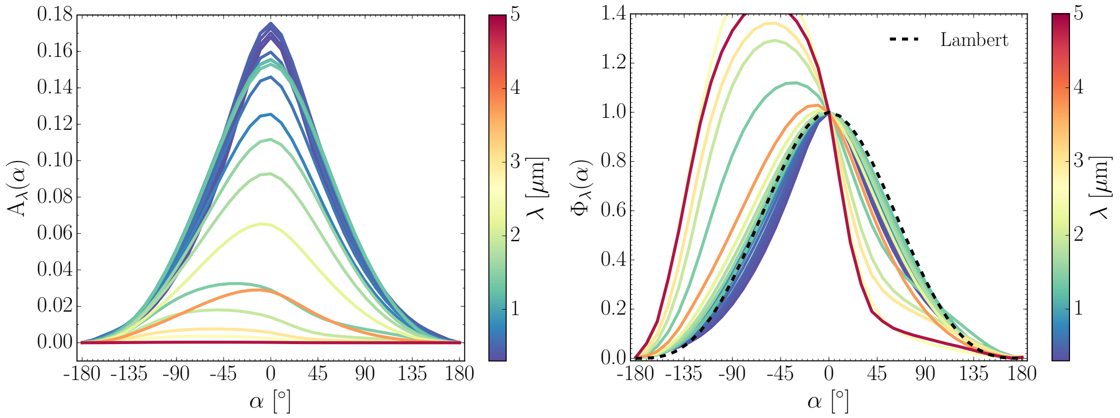

Figure 5.6: Left: Scattered light phase curves of the albedo spectra $A_\lambda(\alpha)$ (Eq. 5.29) of our HD 189733b simulation between 0.3 μm (colour bar: dark purple) to 5.0 μm (colour bar: dark red). Optical and near-IR wavelength packets are more strongly scattered than longer IR wavelengths. Right: Classical phase function (Eq. 5.31), which emphasises the phase curve shapes. Optical wavelengths are more symmetric about the sub-stellar point, IR wavelengths show more variation with phase. A Lambertian phase function (black, dashed line) is over-plotted for reference, which is useful for characterising scattering behaviour (see text).

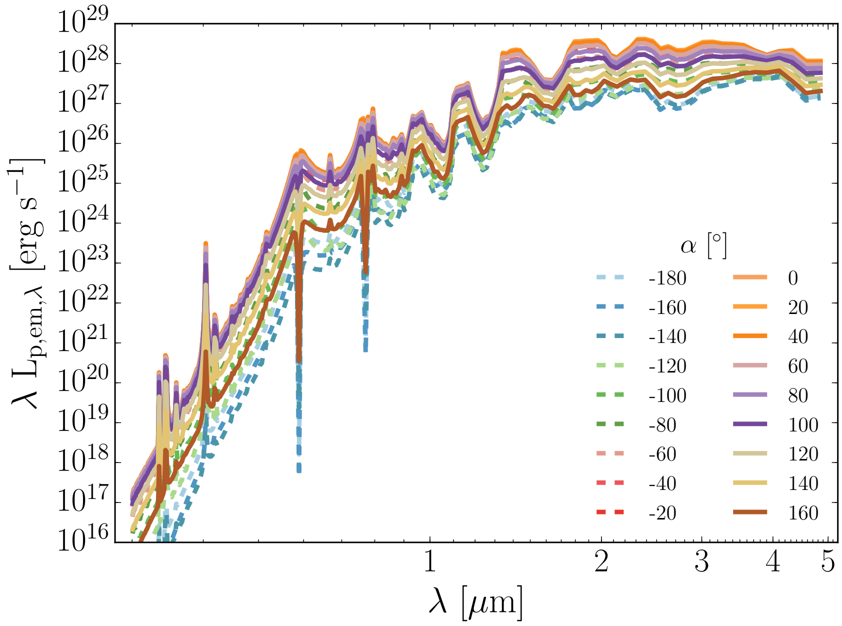

Figure 5.7: Emitted light spectral energy distribution $\lambda\ L_{\rm p,em,\lambda}$ (Eq. 5.35) of our HD 189733b simulation as a function of wavelength at several viewing angles α ($\alpha = 0°$ is the sub-stellar point). Spectral features remain qualitatively similar at different viewing angles with a $\sim$ 1 order of magnitude difference between the sub-stellar point ($\alpha = 0°$) and anti-stellar point ($\alpha = -180°$). The peak wavelength is found to be at $\sim$ 2 μm.

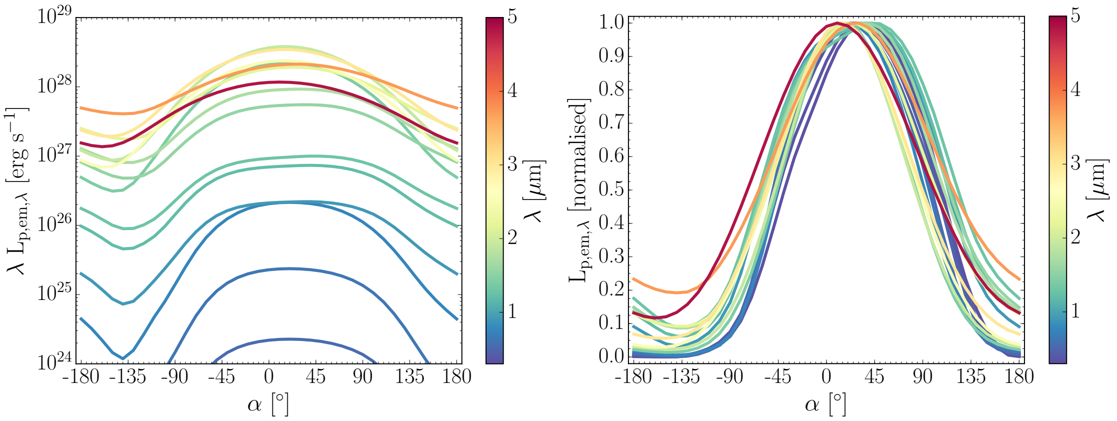

Figure 5.8: Left: Emitted light spectral energy distribution λ L$_{\rm p,em,\lambda}$ (Eq. 5.35) of our HD 189733b simulation phase curves between 0.3 μm (colour bar: dark purple) to 5.0 μm (colour bar: dark red). Infrared wavelengths from 3-5 μm dominate the emission luminosity at all phases. Right: Normalised (to maximum λ L$_{p,em,\lambda}$) spectral energy distribution phase curves to emphasise the phase curve shapes. All wavelengths show a $\alpha \geq 10°$ eastward offset from the sub-stellar point.

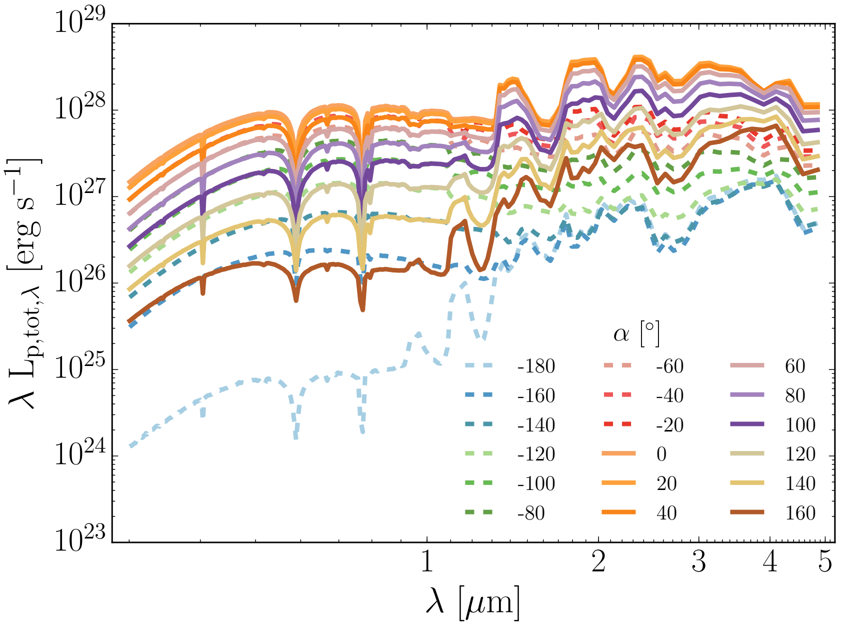

Figure 5.9: Combined scattered and emitted light spectral energy distribution λ L$_{\rm p,tot,\lambda}$ (Eq. 5.39) of our HD 189733b simulation as a function of wavelength at several viewing angles α ($\alpha = 0°$ is the sub-stellar point). The optical wavelength scattered light luminosity drops off as the nightside of the planet is viewed. The emission features between the dayside and nightside are $\sim$ 1 order of magnitude different dependent on wavelength.

optical, the planet's atmospheric emission features are easier to detect.

Figure 5.7 shows the spectral energy distribution (SED) λ $L_{p,em\lambda}$ [erg s^{-1}] (Eq. 5.35) as a function of wavelength for the atmospheric emitted light. We find that the SED follows similar trends across all viewing angles with $\sim$ 1−2 magnitude differences between dayside and nightside emission luminosities. The peak of emission occurs at ~ 2 μm, where our model HD 189733b is brightest in emitted light. The least emission luminosity in the IR occurs at a viewing angle of $\alpha = -140°$, corresponding to the coldest regions of the nightside.

Figure 5.8 (left) presents the planetary atmosphere SED λ $L_{p,em,\lambda}$ (Eq. 5.35) as a function of viewing angle α. We find that emission is dominated by the longer IR wavelengths 2-5μm for all phases. Emission at optical wavelengths is confined to the hottest dayside regions of the planet, however, this emission is $>$ 4 magnitudes in luminosity smaller than IR wavelengths. A dip in luminosity is seen at $\sim -135°$ for all wavelengths, corresponding to the coldest nightside regions of the RHD simulation. Figure 5.8 (right) shows the normalised emitted light phase curves, which emphasises the shape of the phase curve. Most wavelengths show eastern offsets from the sub-stellar point in peak emission at 10-25° with some IR wavelengths showing offsets $\sim$ 45° from the sub-stellar point.

We find that the effects of atmospheric scattering by emitted packets on the phase curves to be negligible. This is because of the low gas phase single scattering albedos ($\omega_{\rm gas} < 10^{-3}$) at IR wavelengths, which lowers the weights of the packets to negligible proportions after one or two scattering interactions. The majority of packets are then likely to be terminated by the Russian Roulette scheme, and those that survive will contain low luminosity weights in future interactions.

5.4.4 Total luminosities and observational predictions

The observed luminosity from an exoplanet atmosphere is a combination of the reflected starlight and the emission from the planet itself. The component that dominates the observation will be wavelength- and phase-dependent owing to the 3D inhomogeneous scattering opacities (from cloud particles) and temperature profiles (from atmospheric circulation) of the planet. Such inhomogeneity is present in the results of the HD 189733b RHD cloud forming simulation. In this section, we combine our scattering and thermal emission results above to produce observable quantities in the TESS (Ricker et al., 2014) and CHEOPS (Broeg et al.,

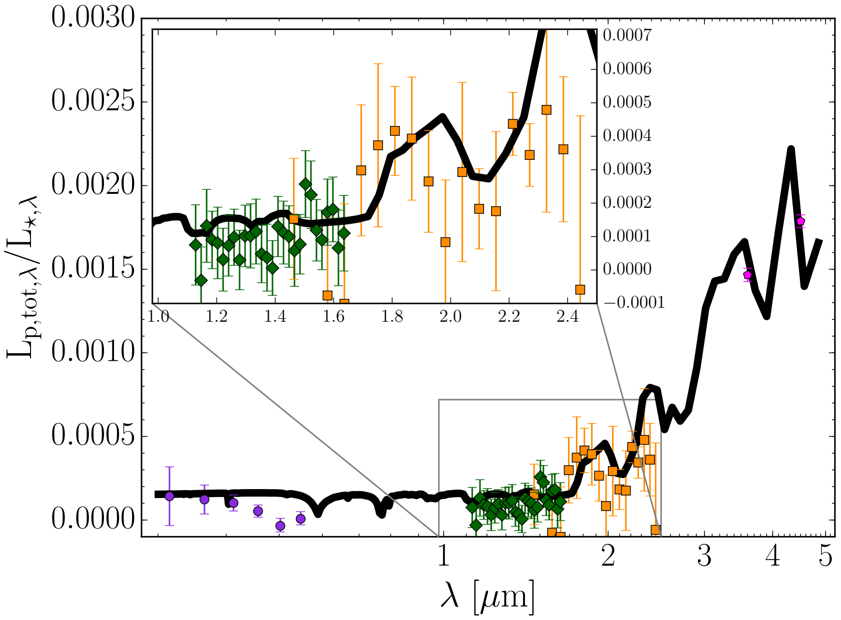

Figure 5.10: Combined scattered and emitted light flux ratio $L_{p,tot,\lambda}/L_{\star,\lambda}$ of our HD 189733b simulation as a function of wavelength at secondary eclipse ($\alpha = 0°$). We compare our HD 189733b simulation results to available observational data from HST STIS (purple dots, 0.29-0.57 μm) (Evans et al., 2013), HST WFC3 (green diamonds, 1.13-1.64 μm) (Crouzet et al., 2014), HST NICMOS (orange squares, 1.46-2.44 μm) (Swain et al., 2009; Barstow et al., 2014), and Spitzer IRAC (magenta pentagons, 3.6 μm, 4.5 μm) (Knutson et al., 2012).

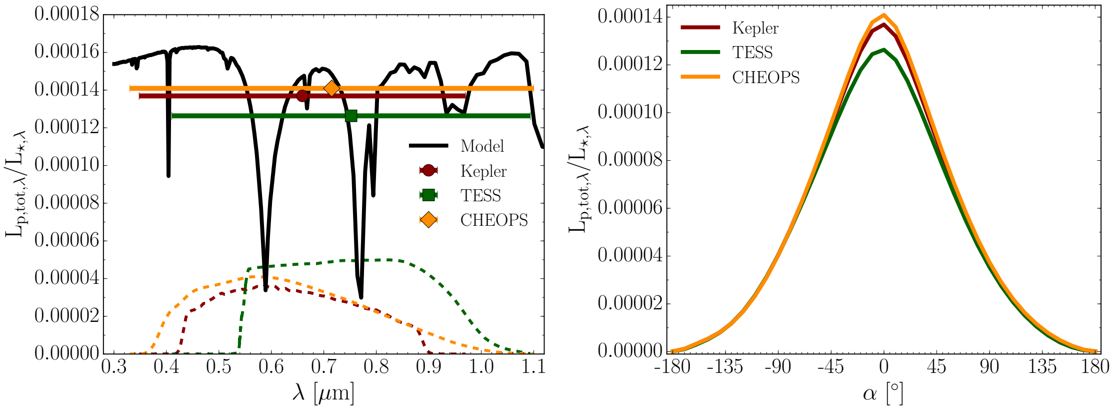

Figure 5.11: Combined scattered and emitted light flux ratio $L_{p,tot,\lambda}/L_{\star,\lambda}$ HD 189733b predictions for the Kepler, TESS, and CHEOPS instruments. Left: Predicted dayside flux ratio for Kepler (red dot), TESS (green square) and CHEOPS (orange diamond) photometric bandpasses. The solid black line is the model output. Dashed lines indicate the spectral response function of the instrument. Right: Predicted Kepler (red), TESS (green) and CHEOPS (orange) flux ratio phase curves. All three instruments show no/little offset from the sub-stellar point, we predict a westward maximum flux offset of only -5° — 0° from the sub-stellar point.

2013) bandpasses for our HD 189733b model. We also compare to readily available observational data from current/past missions. We also produce Kepler band predictions, despite K2 not scheduled to observe HD 189733b, to allow a comparison to other studies focused on modelling Kepler objects (e.g. Parmentier et al., 2016).

The total monochromatic luminosity from the planet is the sum of the reflected light and emitted light

$$L_{\rm p,tot,\lambda} = L_{\rm p,scat,\lambda} + L_{\rm p,em,\lambda}. \tag{5.39}$$

The apparent geometric albedo (which includes scattered and emitted light) is then

$$A_{g,\lambda} = \frac{L_{\rm p,tot,\lambda}\,(\alpha = 0^{\circ})\,3}{L_{\rm inc,\lambda}2}, \tag{5.40}$$

in which the numerator and denominator are integrated across the Kepler, TESS, and CHEOPS bandpasses. For our comparisons to observational data and observational predictions, instead of assuming the host star radiates as a black body in previous sections, the stellar monochromatic luminosity of HD 189733 ($L_{\star,\lambda}$) is taken from the Kurucz [2] stellar atmosphere model for HD 189733.

Figure 5.9 shows the spectral luminosity of the planet as a function of phase including both the scattering and emitted components. On the dayside of the planet, the luminosity from scattered light is at a similar magnitude to the IR emission. For nightside profiles, the scattered light fraction drops off and the emitted luminosity dominates.

Figure 5.10 presents the flux ratio $L_{\rm p,tot,\lambda}/L_{\star,\lambda}$ of our combined scattered and emitted light, compared to the HST secondary eclipse data from Swain et al. (2009); Evans et al. (2013); Crouzet et al. (2014); Barstow et al. (2014) and Spitzer data from Knutson et al. (2012). Similar to Sect. 5.4.1, our simulation is consistent with the B Band HST STIS data from Evans et al. (2013) but overestimates the planet-star flux ratio for the V Band. The results are consistent with the HST WFC3 (Crouzet et al., 2014) and NICMOS (Swain et al., 2009; Barstow et al., 2014) spectral trends, with offsets in the amplitude of these features. Several retrieval models on this and similar observational data (e.g. Madhusudhan & Seager, 2009; Lee et al., 2012; Line et al., 2012, 2014) suggest a possible sub-solar H_2O abundance on the dayside of HD 189733b, which would lower the amplitude of the H_2O features in our results. Our results are

---

[2] http://kurucz.harvard.edu/stars/hd189733/

Table 5.1: Summary of observational predictions. A_g is the predicted geometric albedo across the bandpass. The offset is defined as degrees from the sub-stellar point.

Telescope	λ [μm]	A_g	Offset [°]
Kepler	0.35-0.97	0.2221	-5—0
TESS	0.41-1.10	0.2050	-5—0
CHEOPS	0.33-1.10	0.2286	-5—0

also consistent with the 3.6 μm and 4.5 μm Spitzer IRAC photometry observations of Knutson et al. (2012). Overall, our current model reproduces the secondary transit optical to near-IR observational trends well.

Figure 5.11 (left) shows the dayside flux ratio predictions for Kepler, TESS, and CHEOPS bandpasses. We predict a $\sim$ 10 % difference in peak flux ratio between the CHEOPS and TESS bandpasses. This is directly due to the sensitivity of the CHEOPS bandpass to the optical scattering component of our RHD modelled cloud particles, while the TESS bandpass is unaffected by this component and more sensitive to the near-IR thermal emission of the HD 189733b model.

Figure 5.11 (right) presents the flux ratio phase curves for the Kepler, TESS, and CHEOPS bandpasses. Our modelling results show that we expect HD 189733b to have a zero or small westward offset of no less than -5° from the sub-stellar point for the Kepler, TESS, and CHEOPS bands. This suggests that the cloud particle differences (size, composition, etc.) at the east and western hemispheres in our RHD simulation are not radically different enough to produce the larger ($< -10°$) westward offsets seen for some Kepler planets. The TESS and CHEOPS photometry become comparable at greater longitudes as the cloud particle scattering component becomes less dominant compared to the thermal emission (Fig. 5.9).

If the extra absorption component from the Evans et al. (2013) HST STIS measurements at $\sim$ 0.4-0.5 μm is taken into account, owing to the bandpass efficiencies, the Kepler and CHEOPS contrast ratios and geometric albedos of HD 189733b are likely to be lower than those presented here. However, the TESS photometric band would be relatively unaffected owing to the low sensitivity in this wavelength regime, unless the influence of this absorber extends into the near-IR. Table 5.1 summarises our Kepler, TESS, and CHEOPS predictions, including estimates of the geometric albedo A_g (Eq. 5.40) in each respective band.

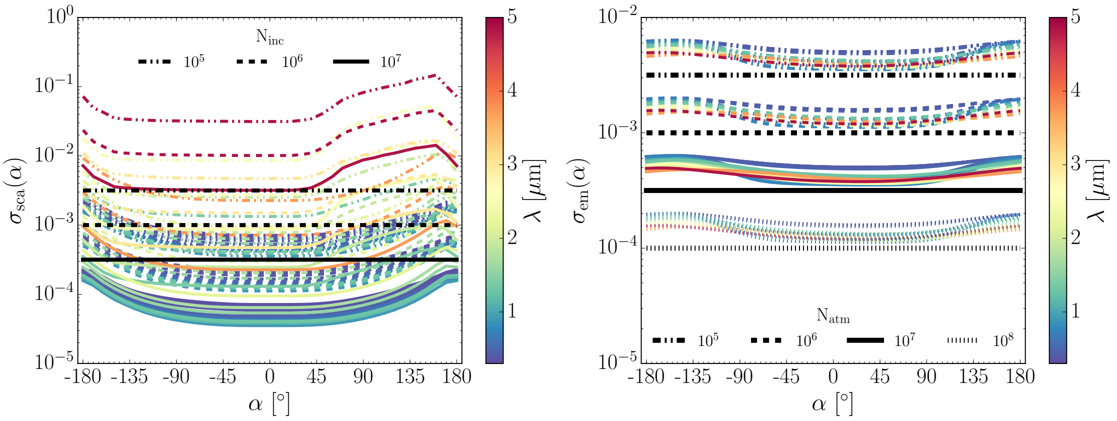

Figure 5.12: Scattered light (Top) and emitted light (Bottom), noise error σ (Eq. 5.27) with viewing angle α and wavelength (colour bar). The nominal noise error values for $N_{inc/atm} = 10^5$ (dash-dot line), 10^6 (dashed line), 10^7 (solid line) and 10^8 (dotted line) are the horizontal black lines. Most scattered and emitted light images are near or below the nominal values, suggesting that each packet contributes once or more to multiple images.

5.4.5 Variance and convergence

To test the convergence of the results, the same experiments are performed with a varying number of initialised photon packets. We repeat the above simulations with $N_{\text{inc/atm}} = 10^5$, 10^6 and 10^7 to test the decrease of σ with initialised packet numbers.

Figure 5.12 shows the noise error of each scattered and emitted light image for our three $N_{\text{inc/atm}}$ simulations with viewing angle α and wavelength. We also show the nominal value (black horizontal line) from the total initialised photons (N_{inc}, N_{atm}). In incident scattered light, all but the longest IR wavelengths show noise errors below the nominal values, indicating that most incident stellar packets contribute to one or more image results. In thermal emitted light, the noise error values are within 2-3 times the nominal value, suggesting that most thermally emitted photons also contribute to many image outputs. The error only increases by a factor of 2 or 3 for images including a nightside component, which suggests that composite emission biasing was successful in more evenly spreading the noise error between high and low luminosity regions. Our presented results of the previous sections using $N_{\text{inc}} = 10^7$, $N_{\text{atm}} = 10^8$, have a typical model noise error of < 0.1 %.

6

Future Prospects for Cloud Formation Modelling

6.1 Introduction

In this chapter, we follow up on each of the previous chapters and look ahead to future prospects for modelling hot Jupiter exoplanet atmospheres using these techniques. We present additional theory building on the topics of the previous chapters.

6.2 1D modelling

The use of 1D modelling for investigation of exoplanet clouds will continue for the foreseeable future as the workhorses in exoplanet atmospheric modelling. The increased chemical detail of 1D modelling compared to 3D simulations is a valuable tool to analyse what material species are important to focus on in the 3D models, where computational efficiency in addition to reasonable accuracy is required. 1D cloud modelling for radiative-convective [RC] modelling of exoplanet atmospheres is still an important and a staple of the modern modelling approach to exoplanet atmospheres. A similar consistent coupling to exoplanet based RC modelling to the DRIFT-PHOENIX sub-stellar models (Witte et al., 2009) would be a fruitful endeavour and help physical understanding of the observations. Coupling a cloud formation model to chemical kinetics and radiative-convective modelling studies such as those in Drummond et al. (2016) is a rich avenue to be explored for the future of 1D cloud formation modelling.

6.3 3D RHD/GCM cloud formation modelling

A key goal for cloud formation modelling in 3D RHD/GCM models will be a push to lower atmospheric temperatures than hot Jupiters. Mbarek & Kempton (2016) published equilibrium calculations of cloud condensates for cooler atmospheres ($T_{eq} < 1000$ K). Cr, Cr_2O_3 and Cr_7C_3 are expected to condense at around 1300 K. Sulfide species such as Na_2S, ZnS, MnS are proposed to condense for $T_{eq} < 1000$ K (Morley et al., 2013). At lower temperatures ($\sim$ 700 K) Chloride materials such as KCl and NaCl are expected to start to condense out. Carbon graphite is also expected to condense at these lower temperatures, should atomic C be abundant.

One question that arises for these lower temperature atmospheres is what material or materials seed particles may be made out of. Two promising candidates are KCl and NaCl. Cl is reasonably abundant at solar metallicities and its main chemical pathways only involve K and Na materials. This suggests that KCl and NaCl condensation will have little competition from other species and can proceed efficiently. Although Sulphate materials will dominate most of the cloud composition at these temperatures (Morley et al., 2013), nucleation of KCl and NaCl could be an efficient way of forming first surfaces in these atmospheres. Another homogenous nucleation candidate is Cr. This material fulfils a similar role to TiO_2 for our high temperature models, a lower abundance but refractory material that can nucleate. Only a thorough investigation into the nucleation properties of these materials will be able to inform modellers of a reasonable choice of seed species. Basic science investigations on these materials such as those carried out by Jeong et al. (2000), Helling & Fomins (2013) and Lee et al. (2015b) on seed particles will need to be repeated for lower temperature materials.

A true holistic cloud formation model for RHD/GCMs should have a hierarchy of cloud formation models suitable for the atmospheric conditions being modelled. Considering a multiplicity of seed particle species along with a larger array of high and low temperature condensates. This is particularly true of hot Jupiters in the range of $T_{eq} = 1000$—1500 K, where atmospheric temperatures range from $\sim$ 2000 K on the dayside to $\sim$ 500 K on the nightside and higher latitudes. From this alone, we should expect a diversity of cloud materials dependent on longitude, latitude and hight in the atmosphere. Table 6.1 presents a list of surface chemical reactions for lower temperature condensates, including ices important for the atmospheres of cold gas and ice giants. Adding and testing the results of these reactions to the kinetic scheme will be an important part of future development of the cloud formation model.

6.4 Monte Carlo radiative-transfer modelling

Monte Carlo radiative-transfer is a highly flexible method and thrives in 3D, inhomogeneous environments such as exoplanet atmospheres. Although at present not a mainstream radiative-transfer method for exoplanets, interest is growing. Due to the ‘embarrassingly parallel’ nature of MCRT, with advances in computing power MCRT may become a workhorse for scientists looking for an accurate and flexible multiple-scattering method. This may follow a similar path to the protoplanetary disk community where MCRT methods are now an ‘industry staple’ for all aspects of radiative-transfer

Raman scattering

Raman scattering defined as when a photon is red or blue shifted in a gas phase scattering event, usually by H_2 or N_2 molecules. This has been examined using 1D methods in Marley et al. (1999) and Oklopčić et al. (2016) which found that this process creates ‘Raman ghost’ line in albedo spectra. The probability of a MCRT packet undergoing a Raman scattering event is given by the ratio of the Raman cross sectional opacity to the total opacity.

$$P_{\rm Ram} = \frac{\kappa_{\rm Ram}}{\kappa_{\rm gas,tot}}, \tag{6.1}$$

where $\kappa_{\rm Ram}$ is the Raman mass opacity of H_2 or N_2 and $\kappa_{\rm gas,tot}$ the total opacity (including Raman opacity) of the gas phase. After a Raman scattering event has been determined, the new frequency of the photon packet can be sampled from the details of the quantum numbers of the gas species, dependent on the temperature (Oklopčić et al., 2016). This may be an important modelling consideration for studying H_2 and N_2 abundances for cold directly imaged exoplanets, especially super-Earth atmospheres.

Table 6.1: Table of chemical reactions for lower temperature cloud forming species

Solid s	Surface reaction	Key species	Reference
Refractories, sulfides & salts			
$Cr[s]$	$Cr \rightarrow Cr[s]$	Cr	Morley et al. (2012)
chromium	$CrH + OH \rightarrow Cr[s] + H_2O$	CrH	
	$CrO + H_2 \rightarrow Cr[s] + H_2O$	CrO	
	$CrO_2 + 2\ H_2 \rightarrow Cr[s] + 2\ H_2O$	CrO_2	
	$CrO_3 + 3\ H_2 \rightarrow Cr[s] + 3\ H_2O$	CrO_3	
$MnS[s]$	$MnS \rightarrow MnS[s]$	MnS	
alabandite	$Mn + H_2S \rightarrow MnS[s] + H_2$	Mn	Morley et al. (2012)
	$MnO + H_2S \rightarrow MnS[s] + H_2O$	min[MnO, H_2S]	
	$2\ MnH + 2\ H_2S \rightarrow 2\ MnS[s] + 3\ H_2$	min[MnH, H_2S]	
	$MnH + HS \rightarrow MnS[s] + H_2$	min[MnH, HS]	
	$2\ MnH + 2\ CS \rightarrow 2\ MnS[s] + H_2 + 2\ C$	min[MnH, CS]	
$Na_2S[s]$	$2\ Na + H_2S \rightarrow Na_2S[s] + H_2$	½Na	Morley et al. (2012)
sodium sulfide	$2\ Na + S \rightarrow Na_2S[s]$	min[½Na, S]	
	$2\ NaH + H_2S \rightarrow Na_2S[s] + 2\ H_2$	½NaH	
	$2\ NaOH + H_2S \rightarrow Na_2S[s] + 2\ H_2O$	½NaOH	
$ZnS[s]$	$Zn + H_2S \rightarrow ZnS[s] + H_2$	Zn	Morley et al. (2012)
sphalerite	$ZnO + H_2S \rightarrow ZnS[s] + H_2O$	ZnO	
	$ZnH + HS \rightarrow ZnS[s] + H_2$	min[ZnH, HS]	
	$2\ ZnH + 2\ CS \rightarrow 2\ ZnS[s] + H_2 + 2\ C$	min[ZnH, CS]	
$KCl[s]$	$KCl \rightarrow KCl[s]$	KCl	Morley et al. (2012)
sylvite	$K + Cl \rightarrow KCl[s]$	min[K,Cl]	
	$KH + HCl \rightarrow KCl[s] + H_2$	min[KH, HCl]	Helling et al. (2016b)
	$KH + NaCl \rightarrow KCl[s] + NaH$	min[KH, $NaCl$]	
	$KOH + HCl \rightarrow KCl[s] + H_2O$	min[KOH, HCl]	Helling et al. (2016b)
	$KOH + CaCl \rightarrow KCl[s] + CaOH$	min[KOH, $CaCl$]	Helling et al. (2016b)
$NaCl[s]$	$NaCl \rightarrow NaCl[s]$	$NaCl$	
halite	$Na + Cl \rightarrow NaCl[s]$	min[Na, Cl]	
	$NaH + HCl \rightarrow NaCl[s] + H_2$	min[NaH, HCl]	
	$NaH + KCl \rightarrow NaCl[s] + KH$	min[NaH, KCl]	
	$NaOH + HCl \rightarrow NaCl[s] + H_2O$	min[$NaOH$, HCl]	
	$NaOH + CaCl \rightarrow NaCl[s] + CaOH$	min[$NaOH$, $CaCl$]	
$NH_4SH[s]$ ammonium hydrosulfide	$NH_3 + H_2S \rightarrow NH_4SH[s]$	min[NH_3,H_2S]	
Liquids & ices	[s] = solid phase (ice), [l] = liquid phase		
$H_2O[s/l]$	$H_2O \rightarrow H_2O[s/l]$	H_2O	
water ice/liquid	$CO + 3H_2 \rightarrow H_2O[s/l] + CH_4$	CO	
	$CO_2 + H_2 \rightarrow H_2O[s/l] + CO$	CO_2	
$NH_3[s/l]$	$NH_3 \rightarrow NH_3[s/l]$	NH_3	
ammonia ice/liquid	$N_2 + 3H_2 \rightarrow 2NH_3[s/l]$	N_2	
	$HCN + 3H_2 \rightarrow NH_3[s/l] + CH_4$	HCN	
$H_2S[s/l]$ hydrogen sulfide ice/liquid	$H_2S \rightarrow H_2S[s/l]$	H_2S	
$CH_4[s/l]$	$CH_4 \rightarrow CH_4[s/l]$	CH_4	
methane ice/liquid	$C_2H_2 + 3H_2 \rightarrow 2CH_4[s/l]$	C_2H_2	
	$CO + 3H_2 \rightarrow CH_4[s/l] + H_2O$	CO	
	$HCN + 3H_2 \rightarrow CH_4[s/l] + NH_3$	HCN	

Photochemistry & Haze Formation

Another solid material of importance to solar system and exoplanet atmospheres other than clouds is the formation of photochemical haze. These hazes form via a network of chemical reactions brought on by the non-equilibrium effects of high energy UV photons.

The energy absorbed by a particular material A_i [erg s^{-1}] in a computational cell can be estimated by the Monte Carlo method via (Lucy, 1999)

$$A_i = \frac{\epsilon_0}{\Delta t}\frac{1}{V}\sum_l \kappa_{i,\lambda} l, \tag{6.2}$$

where $\epsilon_0 = \mathrm{L_{inc}} \,/\, \mathrm{N_{ph}}$ is the power or luminosity carried by one packet, Δt the time of the simulation, V the volume of the cell, $\kappa_{i,\lambda}$ the opacity of material i and l the path length traveled by a packet in the cell. By tracking the total path length traced out by the packets in a single cell, the absorption rate of a particular species can be estimated. For photochemistry we are interested in the rates of decomposition of gas phase species by energetic photons. An example reaction is the decomposition of CH_4 into CH_3 via

$$CH_4 + h\nu \rightarrow CH_3 + H. \tag{6.3}$$

The task of the MCRT scheme is then to find the number of photon interactions of a certain wavelength with CH_4. Using the definition in Eq. 6.2, the interaction rate of photon packets is

$$I_i = \frac{L_{\rm inc}}{N_{\rm ph} hc}\frac{1}{V}\sum_l \lambda \sigma_i l, \tag{6.4}$$

where this calculation is performed between a maximum and minimum wavelength dependent on the dependence on the decomposition cross section with wavelength. For example, for CH_4 in Eq. 6.3 the decomposition cross section occurs at photon wavelength of 0.0773—0.277μm.

7

Conclusion

In this chapter we summarise and conclude the thesis content and evaluate the general aims of the thesis. In Chapter 2 we reviewed the cloud formation chemistry surface chemistry. Cloud formation in hot Jupiter atmospheres occurs from a sequence of steps:

- The nucleation of seed particles (either homogeneously or heterogeneously).
- Subsequent growth of cloud particles from thermochemically stable materials via surface chemical reactions.
- Advection and settling of cloud particles with atmospheric motions.
- Replenishment of gas phase material from upward mixing or horizontal advection.

In Chapter 3 we used our 1D cloud formation model DRIFT to investigate the cloud formation properties of the hot Jupiter HD 189733b. In a 2-model approach we applied the cloud formation model to RHD output from Dobbs-Dixon & Agol (2013). We found that the atmosphere of HD 189733b is likely host to a thick and varied atmospheric cloud complex, dependent on the longitude, latitude and depth of the planet. The 1D approach captures detailed thermochemical properties of the atmosphere and provides critical insight into how to proceed with the required physics for 3D modelling, where efficiency is as important as accuracy.

In Chapter 4 we time-dependently coupled the 3D cloud formation model to the RHD simulations of Dobbs-Dixon & Agol (2013) self consistently. We found that considering the 3D structure of the atmosphere resulted in a highly inhomogeneous cloud structure. The cloud had a significant feedback effect on the temperature structure of the dayside of the planet, with a greenhouse effect resulting in a temperature inversion deeper in the atmosphere.

In Chapter 5 we post-process the results of Chapter 4 using a Monte Carlo radiative-transfer code. We investigated the observable properties of the simulated exoplanet and compared our simulation results with observational data.

Many improvements to the methodology of the models could be implemented in the future. Additions to the RHD scheme to include the effects of radiation scattering by cloud particles, which could have a large effect in the T-p structures of the models. The added CPU cost of the cloud formation scheme to the RHD scheme is a major barrier to the study of long term (> 1000 days) cloud dynamics. These longer times are required to be performed in order to accuracy gauge the effects of cloud settling, vertical element replenishment and potential long term variability in the atmospheres of hot Jupiters. A critical future improvement will be to find efficiency gains for the cloud formation kinetic network, without compromising accuracy. A similar approach may be taken to gas phase chemical models where a number of "unimportant" reactions are removed from the scheme to improve the efficiency with little effect on accuracy.

The models presented in this thesis are highly flexible and can be extended to investigate atmospheric properties across a wide variety of atmospheric temperatures, pressures and metallicities. An extension of the cloud formation code to lower temperatures in order to model cloud material important for Warm-Neptune/Super-Earth atmospheres will be critical to the theoretical evaluation of observational data in the near future. Monte Carlo radiative transfer shows great promise in accuracy describing the radiation field in 3D, cloudy environments. Expansion of the MCRT code to investigate a number of photochemical physics such as Raman scattering, photochemistry and haze formation and polarisation can be undertaken in the future. Due to its true 3D nature, MCRT is ideal to investigate 3D radiative-transfer problems, especially for inhomogeneous, scattering large and small scale cloud structures in exoplanet atmospheres. MCRT methods are now a staple of the protoplanetary disk community after decades of using ray tracing or steam methods. If the uptake of MCRT is a vigorous in the exoplanet community as it has been in the protoplanetary disk community, then MCRT has a bright future for exoplanet modelling.

With the advent of highly sensitive spectroscopic and photometric missions to study exoplanet atmospheres (JWST, WFIRST, TESS, CHEOPS) and a dearth of directly imaged data arriving in the near future, a holistic framework of modelling the 3D properties of exoplanets must be undertaken in order to provide a physical basis to observational data. In this thesis we have successfully undertaken a first inquiry into a holistic, 3D modelling of cloud particle formation, dynamics and their effects on radiative-transport in exoplanet atmospheres. Further development of the framework presented here will enable the astronomy and planetary science communities to have greater confidence in the interpretation of future and current observational data.

Bibliography

Ackerman, A. S., & Marley, M. S. 2001, ApJ, 556, 872, astro-ph/0103423

Agúndez, M., Parmentier, V., Venot, O., Hersant, F., & Selsis, F. 2014, A&A, 564, A73, 1403.0121

Allard, F., Allard, N. F., Homeier, D., Kielkopf, J., McCaughrean, M. J., & Spiegelman, F. 2007, A&A, 474, L21, 0709.1192

Allard, F., Guillot, T., Ludwig, H.-G., Hauschildt, P. H., Schweitzer, A., Alexander, D. R., & Ferguson, J. W. 2003, in IAU Symposium, Vol. 211, Brown Dwarfs, ed. E. Martín, 325

Allard, F., Hauschildt, P. H., Alexander, D. R., Tamanai, A., & Schweitzer, A. 2001, ApJ, 556, 357, astro-ph/0104256

Amundsen, D. S., Baraffe, I., Tremblin, P., Manners, J., Hayek, W., Mayne, N. J., & Acreman, D. M. 2014, A&A, 564, A59

Amundsen, D. S. et al. 2016, A&A, 595, A36

Anders, E., & Grevesse, N. 1989, Geochimica et Cosmochimica Acta, 53, 197

Angerhausen, D., DeLarme, E., & Morse, J. A. 2015, PASP, 127, 1113, 1404.4348

Anglada-Escudé, G. et al. 2016, Nature, 536, 437, 1609.03449

Asplund, M., Grevesse, N., Sauval, A. J., & Scott, P. 2009, ARA&A, 47, 481, 0909.0948

Auvergne, M. et al. 2009, A&A, 506, 411, 0901.2206

Baes, M., Gordon, K. D., Lunttila, T., Bianchi, S., Camps, P., Juvela, M., & Kuiper, R. 2016, A&A, 590, A55, 1603.07945

Barman, T. S., Hauschildt, P. H., & Allard, F. 2001, ApJ, 556, 885, astro-ph/0104262

Barstow, J. K., Aigrain, S., Irwin, P. G. J., Hackler, T., Fletcher, L. N., Lee, J. M., & Gibson, N. P. 2014, ApJ, 786, 154, 1403.6664

Beatty, T. G., Madhusudhan, N., Tsiaras, A., Zhao, M., Gilliland, R. L., Knutson, H. A., Shporer, A., & Wright, J. T. 2016, ArXiv e-prints, 1612.06409

Beuzit, J.-L. et al. 2008, in Proc. SPIE, Vol. 7014, Ground-based and Airborne Instrumentation for Astronomy II, 701418

Bohren, C. F., & Huffman, D. R. 1983, Absorption and scattering of light by small particles

Borucki, W. J. et al. 2010, Science, 327, 977

Broeg, C. et al. 2013, in European Physical Journal Web of Conferences, Vol. 47, European Physical Journal Web of Conferences, 03005, 1305.2270

Bruggeman, D. A. G. 1935, Annalen der Physik, 416, 636

Burrows, A., Sudarsky, D., & Hubeny, I. 2006, ApJ, 640, 1063, astro-ph/0509066

Cahoy, K. L., Marley, M. S., & Fortney, J. J. 2010, ApJ, 724, 189, 1009.3071

Calatayud, M., Maldonado, L., & Minot, C. 2008, The Journal of Physical Chemistry C, 112, 16087, http://dx.doi.org/10.1021/jp802851q

Cashwell, E. D., & Everett, C. J. 1959, A practical manual on the Monte Carlo method for random walk problems, Internat. Tracts Computat. Sci. Technol. (London: Pergamon)

Charbonneau, D., Brown, T. M., Latham, D. W., & Mayor, M. 2000, ApJL, 529, L45, astro-ph/9911436

Charbonneau, D., Brown, T. M., Noyes, R. W., & Gilliland, R. L. 2002, ApJ, 568, 377, astro-ph/0111544

Charnay, B., Meadows, V., & Leconte, J. 2015a, ApJ, 813, 15, 1509.06814

Charnay, B., Meadows, V., Misra, A., Leconte, J., & Arney, G. 2015b, ApJL, 813, L1, 1510.01706

Cosentino, R. et al. 2012, in Proc. SPIE, Vol. 8446, Ground-based and Airborne Instrumentation for Astronomy IV, 84461V

Crouzet, N., McCullough, P. R., Deming, D., & Madhusudhan, N. 2014, ApJ, 795, 166, 1409.4000

de Kok, R. J., & Stam, D. M. 2012, Icarus, 221, 517, 1208.2795

Dehn, M., Helling, C., Woitke, P., & Hauschildt, P. 2007, in IAU Symposium, Vol. 239, IAU Symposium, ed. F. Kupka, I. Roxburgh, & K. L. Chan, 227–229

Deming, D. et al. 2013, ApJ, 774, 95, 1302.1141

Demory, B.-O. et al. 2013, ApJL, 776, L25, 1309.7894

Dobbs-Dixon, I., & Agol, E. 2013, MNRAS, 435, 3159, 1211.1709

Dobbs-Dixon, I., Agol, E., & Burrows, A. 2012, ApJ, 751, 87, 1110.4377

Dobbs-Dixon, I., Cumming, A., & Lin, D. N. C. 2010, ApJ, 710, 1395, 1001.0982

Dorschner, J., Begemann, B., Henning, T., Jaeger, C., & Mutschke, H. 1995, A&A, 300, 503

Draine, B. T. 2003, ApJ, 598, 1017, astro-ph/0304060

Draine, B. T., & Salpeter, E. E. 1977, Journal of Chemical Physics, 67, 2230

Drummond, B., Tremblin, P., Baraffe, I., Amundsen, D. S., Mayne, N. J., Venot, O., & Goyal, J. 2016, A&A, 594, A69, 1607.04062

Dupree, S. A., & Fraley, S. K. 2002, A Monte Carlo Primer

Dyudina, U., Zhang, X., Li, L., Kopparla, P., Ingersoll, A. P., Dones, L., Verbiscer, A., & Yung, Y. L. 2016, ApJ, 822, 76, 1511.04415

Elsasser, W. 1942, Heat Transfer by Infrared Radiation in the Atmosphere

Esteves, L. J., De Mooij, E. J. W., & Jayawardhana, R. 2015, ApJ, 804, 150, 1407.2245

Evans, T. M. et al. 2013, ApJL, 772, L16, 1307.3239

Fortney, J. J., Cooper, C. S., Showman, A. P., Marley, M. S., & Freedman, R. S. 2006, ApJ, 652, 746, astro-ph/0608235

Fortney, J. J., Shabram, M., Showman, A. P., Lian, Y., Freedman, R. S., Marley, M. S., & Lewis, N. K. 2010, ApJ, 709, 1396, 0912.2350

Gail, H.-P., Keller, R., & Sedlmayr, E. 1984, A&A, 133, 320

Gail, H.-P., & Sedlmayr, E. 1986, A&A, 166, 225

——. 2014, Physics and Chemistry of Circumstellar Dust Shells

Garcia Munoz, A., & Isaak, K. G. 2015, Proceedings of the National Academy of Science, 112, 13461, 1511.01424

Gillon, M. et al. 2017, ArXiv e-prints, 1703.01424

Goumans, T. P. M., & Bromley, S. T. 2012, MNRAS, 420, 3344

Hansen, J. E. 1971, Journal of Atmospheric Sciences, 28, 1400

Hansen, J. E., & Travis, L. D. 1974, Space Science Reviews, 16, 527

Harries, T. J., Monnier, J. D., Symington, N. H., & Kurosawa, R. 2004, MNRAS, 350, 565, astro-ph/0401574

Hartogh, P., Medvedev, A. S., Kuroda, T., Saito, R., Villanueva, G., Feofilov, A. G., Kutepov, A. A., & Berger, U. 2005, Journal of Geophysical Research (Planets), 110, 11008

Heintzenberg, J. 1994, Aerosol Science and Technology, 21, 46, http://dx.doi.org/10.1080/02786829408959695

Helling, C. 2009, in American Institute of Physics Conference Series, Vol. 1094, 15th Cambridge Workshop on Cool Stars, Stellar Systems, and the Sun, ed. E. Stempels, 162–171, 0809.4562

Helling, C., Dehn, M., Woitke, P., & Hauschildt, P. H. 2008a, ApJL, 677, L157

Helling, C., & Fomins, A. 2013, Royal Society of London Philosophical Transactions Series A, 371, 10581

Helling, C., Klein, R., Woitke, P., Nowak, U., & Sedlmayr, E. 2004, A&A, 423, 657, astro-ph/0404272

Helling, C. et al. 2016a, MNRAS, 460, 855, 1603.04022

Helling, C., Oevermann, M., Lüttke, M. J. H., Klein, R., & Sedlmayr, E. 2001, A&A, 376, 194

Helling, C., Rimmer, P. B., Rodriguez-Barrera, I. M., Wood, K., Robertson, G. B., & Stark, C. R. 2016b, Plasma Physics and Controlled Fusion, 58, 074003, 1604.03369

Helling, C., Winters, J. M., & Sedlmayr, E. 2000, A&A, 358, 651

Helling, C., & Woitke, P. 2006, A&A, 455, 325

Helling, C., Woitke, P., & Thi, W.-F. 2008b, A&A, 485, 547, 0803.4315

Heng, K., & Demory, B.-O. 2013, ApJ, 777, 100, 1309.5956

Heng, K., Hayek, W., Pont, F., & Sing, D. K. 2012, MNRAS, 420, 20, 1107.1390

Heng, K., Menou, K., & Phillipps, P. J. 2011, MNRAS, 413, 2380, 1010.1257

Heng, K., & Showman, A. P. 2015, Annual Review of Earth and Planetary Sciences, 43, 509, 1407.4150

Henning, T., Begemann, B., Mutschke, H., & Dorschner, J. 1995, A&AS, 112, 143

Henyey, L. G., & Greenstein, J. L. 1941, ApJ, 93, 70

Hiranaka, K., Cruz, K. L., Douglas, S. T., Marley, M. S., & Baldassare, V. F. 2016, ApJ, 830, 96, 1606.09485

Hood, B., Wood, K., Seager, S., & Collier Cameron, A. 2008, MNRAS, 389, 257, 0807.1561

Jäger, C., Dorschner, J., Mutschke, H., Posch, T., & Henning, T. 2003, A&A, 408, 193

Jeong, K. S., Chang, C., Sedlmayr, E., & Sülzle, D. 2000, Journal of Physics B Atomic Molecular Physics, 33, 3417

Jeong, K. S., Winters, J. M., Le Bertre, T., & Sedlmayr, E. 2003, A&A, 407, 191

Kataria, T., Showman, A. P., Fortney, J. J., Marley, M. S., & Freedman, R. S. 2014, ApJ, 785, 92, 1401.1898

Kataria, T., Sing, D. K., Lewis, N. K., Visscher, C., Showman, A. P., Fortney, J. J., & Marley, M. S. 2016, ApJ, 821, 9, 1602.06733

Kattawar, G. W. 1975, Journal of Quantitative Spectroscopy and Radiative Transfer, 15, 839

Knutson, H. A. et al. 2009, ApJ, 690, 822, 0802.1705

——. 2012, ApJ, 754, 22, 1206.6887

Komacek, T. D., & Showman, A. P. 2016, ApJ, 821, 16, 1601.00069

Korolev, A. V., & Mazin, I. P. 2003, J. Atmos. Sci., 60, 2957?2974

Lecavelier Des Etangs, A., Pont, F., Vidal-Madjar, A., & Sing, D. 2008, A&A, 481, L83, 0802.3228

Lee, G., Helling, C., Dobbs-Dixon, I., & Juncher, D. 2015a, A&A, 580, A12, 1505.06576

Lee, G., Helling, C., Giles, H., & Bromley, S. T. 2015b, A&A, 575, A11, 1410.6610

Lee, J.-M., Fletcher, L. N., & Irwin, P. G. J. 2012, MNRAS, 420, 170, 1110.2934

Lewis, N. K., Showman, A. P., Fortney, J. J., Knutson, H. A., & Marley, M. S. 2014, ApJ, 795, 150, 1409.5108

Lewis, N. K., Showman, A. P., Fortney, J. J., Marley, M. S., Freedman, R. S., & Lodders, K. 2010, ApJ, 720, 344, 1007.2942

Line, M. R., Knutson, H., Wolf, A. S., & Yung, Y. L. 2014, ApJ, 783, 70, 1309.6663

Line, M. R., Zhang, X., Vasisht, G., Natraj, V., Chen, P., & Yung, Y. L. 2012, ApJ, 749, 93, 1111.2612

Looyenga, H. 1965, Physica, 31, 401

Lucy, L. B. 1999, A&A, 344, 282

Ludwig, H.-G., Allard, F., & Hauschildt, P. H. 2002, A&A, 395, 99, astro-ph/0208584

Macintosh, B. et al. 2014, Proceedings of the National Academy of Science, 111, 12661, 1403.7520

Madhusudhan, N., & Burrows, A. 2012, ApJ, 747, 25, 1112.4476

Madhusudhan, N., & Seager, S. 2009, ApJ, 707, 24, 0910.1347

Marley, M. S., Gelino, C., Stephens, D., Lunine, J. I., & Freedman, R. 1999, ApJ, 513, 879, astro-ph/9810073

Marley, M. S., & McKay, C. P. 1999, Icarus, 138, 268

Mattila, K. 1970, A&A, 9, 53

Mayer, B. 2009, in European Physical Journal Web of Conferences, Vol. 1, European Physical Journal Web of Conferences, 75

Mayne, N. J. et al. 2014, A&A, 561, A1

Mayor, M. et al. 2003, The Messenger, 114, 20

Mbarek, R., & Kempton, E. M.-R. 2016, ApJ, 827, 121, 1602.02759

McCullough, P. R., Crouzet, N., Deming, D., & Madhusudhan, N. 2014, ApJ, 791, 55, 1407.2462

Mie, G. 1908, Annalen der Physik, 330, 377

Min, M., Dullemond, C. P., Dominik, C., de Koter, A., & Hovenier, J. W. 2009, A&A, 497, 155, 0902.3092

Morley, C. V., Fortney, J. J., Kempton, E. M.-R., Marley, M. S., Visscher, C., & Zahnle, K. 2013, ApJ, 775, 33, 1305.4124

Morley, C. V., Fortney, J. J., Marley, M. S., Visscher, C., Saumon, D., & Leggett, S. K. 2012, ApJ, 756, 172, 1206.4313

Moses, J. I. et al. 2011, ApJ, 737, 15, 1102.0063

Oklopčić, A., Hirata, C. M., & Heng, K. 2016, ArXiv e-prints, 1605.07185

Oreshenko, M., Heng, K., & Demory, B.-O. 2016, MNRAS, 457, 3420, 1601.03050

Palik, E. D. 1985, Handbook of optical constants of solids

Parmentier, V., Fortney, J. J., Showman, A. P., Morley, C., & Marley, M. S. 2016, ApJ, 828, 22, 1602.03088

Parmentier, V., Showman, A. P., & Lian, Y. 2013, A&A, 558, A91, 1301.4522

Perna, R., Heng, K., & Pont, F. 2012, ApJ, 751, 59, 1201.5391

Pfeiffer, N., & Chapman, G. H. 2008, Optics Express, 16, 13637

Pinte, C., Ménard, F., Duchêne, G., & Bastien, P. 2006, A&A, 459, 797, astro-ph/0606550

Pollacco, D. L. et al. 2006, PASP, 118, 1407, astro-ph/0608454

Pont, F., Sing, D. K., Gibson, N. P., Aigrain, S., Henry, G., & Husnoo, N. 2013, MNRAS, 432, 2917, 1210.4163

Posch, T., Kerschbaum, F., Fabian, D., Mutschke, H., Dorschner, J., Tamanai, A., & Henning, T. 2003, ApJS, 149, 437

Rauscher, E., & Kempton, E. M. R. 2014, ApJ, 790, 79, 1402.4833

Rauscher, E., & Menou, K. 2010, ApJ, 714, 1334, 0907.2692

Ricker, G. R. et al. 2014, in Proc. SPIE, Vol. 9143, Space Telescopes and Instrumentation 2014: Optical, Infrared, and Millimeter Wave, 914320, 1406.0151

Rijkhorst, E.-J., Plewa, T., Dubey, A., & Mellema, G. 2006, A&A, 452, 907, astro-ph/0505213

Rimmer, P. B., & Helling, C. 2016, ApJS, 224, 9, 1510.07052

Robinson, T. D. 2017, ArXiv e-prints, 1701.05564

Robitaille, T. P. 2011, A&A, 536, A79, 1112.1071

Seager, S. 2010, Exoplanet Atmospheres: Physical Processes

Seager, S., & Sasselov, D. D. 2000, ApJ, 537, 916, astro-ph/9912241

Seager, S., Whitney, B. A., & Sasselov, D. D. 2000, ApJ, 540, 504, astro-ph/0004001

Sharp, C. M., & Burrows, A. 2007, ApJS, 168, 140, astro-ph/0607211

Showman, A. P., Fortney, J. J., Lian, Y., Marley, M. S., Freedman, R. S., Knutson, H. A., & Charbonneau, D. 2009, ApJ, 699, 564, 0809.2089

Showman, A. P., & Kaspi, Y. 2013, ApJ, 776, 85, 1210.7573

Showman, A. P., Lewis, N. K., & Fortney, J. J. 2015, ApJ, 801, 95

Showman, A. P., & Polvani, L. M. 2011, ApJ, 738, 71, 1103.3101

Shporer, A., & Hu, R. 2015, AJ, 150, 112, 1504.00498

Sing, D. K. et al. 2011, A&A, 527, A73, 1008.4795

——. 2016, Nature, 529, 59, 1512.04341

——. 2015, MNRAS, 446, 2428, 1410.7611

Snellen, I. A. G., de Kok, R. J., de Mooij, E. J. W., & Albrecht, S. 2010, Nature, 465, 1049, 1006.4364

Stap, F. A., Hasekamp, O. P., Emde, C., & Röckmann, T. 2016, Journal of Quantitative Spectroscopy and Radiative Transfer, 170, 54

Stark, C. R., Helling, C., & Diver, D. A. 2015, A&A, 579, A41, 1505.04592

Steinacker, J., Baes, M., & Gordon, K. D. 2013, ARA&A, 51, 63, 1303.4998

Swain, M. R., Vasisht, G., & Tinetti, G. 2008, Nature, 452, 329

Swain, M. R., Vasisht, G., Tinetti, G., Bouwman, J., Chen, P., Yung, Y., Deming, D., & Deroo, P. 2009, ApJL, 690, L114

Syzgantseva, O. A., Gonzalez-Navarrete, P., Calatayud, M., Bromley, S., & Minot, C. 2011, The Journal of Physical Chemistry C, 115, 15890, http://dx.doi.org/10.1021/jp2050349

Toon, O. B., McKay, C. P., Ackerman, T. P., & Santhanam, K. 1989, Journal of Geophysical Research, 94, 16287

Tsai, S.-M., Dobbs-Dixon, I., & Gu, P.-G. 2014, ApJ, 793, 141, 1405.0003

Tsuji, T. 2002, ApJ, 575, 264, astro-ph/0204401

——. 2005, ApJ, 621, 1033, astro-ph/0411766

Venot, O., Hébrard, E., Agúndez, M., Dobrijevic, M., Selsis, F., Hersant, F., Iro, N., & Bounaceur, R. 2012, A&A, 546, A43, 1208.0560

Webber, M. W., Lewis, N. K., Marley, M., Morley, C., Fortney, J. J., & Cahoy, K. 2015, ApJ, 804, 94

Whitney, B. A. 2011, Bulletin of the Astronomical Society of India, 39, 101, 1104.4990

Whitney, B. A., Wood, K., Bjorkman, J. E., & Wolff, M. J. 2003, ApJ, 591, 1049, astro-ph/0303479

Wiktorowicz, S. J., Nofi, L. A., Jontof-Hutter, D., Kopparla, P., Laughlin, G. P., Hermis, N., Yung, Y. L., & Swain, M. R. 2015, ApJ, 813, 48, 1507.03588

Witte, S., Helling, C., Barman, T., Heidrich, N., & Hauschildt, P. H. 2011, A&A, 529, A44

Witte, S., Helling, C., & Hauschildt, P. H. 2009, A&A, 506, 1367, 0908.3597

Woitke, P. 2006, A&A, 452, 537, astro-ph/0602371

Woitke, P., & Helling, C. 2003, A&A, 399, 297

——. 2004, A&A, 414, 335

Woitke, P., & Niccolini, G. 2005, A&A, 433, 1101, astro-ph/0404560

Wood, K., & Loeb, A. 2000, ApJ, 545, 86, astro-ph/9911316

Wood, K., & Reynolds, R. J. 1999, ApJ, 525, 799, astro-ph/9905289

Yusef-Zadeh, F., Morris, M., & White, R. L. 1984, ApJ, 278, 186

Zeidler, S., Posch, T., & Mutschke, H. 2013, A&A, 553, A81

Zender, C. 2015, http://dust.ess.uci.edu/facts/psd/psd.pdf

Zhang, X., & Showman, A. P. 2014, ApJL, 788, L6, 1403.2143